POLITECNICO
MILANO 1863

SCUOLA DI INGEGNERIA INDUSTRIALE
E DELL'INFORMAZIONE

Resonant inelastic x-ray scattering study of the double-chain superconducting cuprate $YBa_2Cu_4O_8$

Tesi di Laurea Magistrale in
Engineering Physics - Ingegneria Fisica

Author: **Federico Pisani**

Student ID: 944059
Advisor: Prof. Giacomo C. Ghiringhelli
Co-advisors: Dr. Nicholas B. Brookes
Academic Year: 2020-2021

Abstract

Cuprates are a class of high-temperature superconductors characterised by a layered structure of CuO_2 planes. They are unconventional superconductors where the pairing mechanism between charges presents a d-wave symmetry. Periodical modulations of valence charges, typically with unidirectional character, have essentially been observed in all cuprate families. These charge modulations go under the name of charge density waves (CDWs). Many studies also confirm that CDWs and the superconducting phase compete against one another.

We performed resonant inelastic x-ray scattering at the Cu L_3 edge on single crystals of the underdoped cuprate $YBa_2Cu_4O_8$ (Y124). No direct proof of the existence of CDWs in this compound exists. Nevertheless, the evidence of quantum oscillations and the doping level close to the one of cuprates where CDWs was observed are signs that charge order is present in Y124 as well. Indeed, we found a CDW signal in strict analogy to what observed in other cuprate families: the energy dependence of the quasielastic intensities confirms that charge order in Y124 must be connected to a modulation of the charge density associated with valence electrons of planar copper atoms. Moreover, H- and K-scans demonstrates that CDWs develop along both the a- and b- directions, with unidirectional domains similar in shape and size to those observed in YBCO. On the contrary, considering the temperature dependence of the CDW signal, an evident discrepancy between Y124 and its close relative $YBa_2Cu_3O_{6+x}$ (Y123) is present. It is possible to associate the concave-downward trend in Y124 with the behaviour of an order parameter of broken symmetry. The idea is that the clean stoichiometry of Y124, in contrast to the intrinsic stoichiometric defects associated with the oxygen content in Y123, should allow CDWs to develop as a true second order phase transition.

RIXS spectra collected with an energy resolution around 35 meV allowed to study the dispersions of phononic and magnetic excitations in Y124. RIXS is able to probe two vibrational modes in cuprates, the buckling and the breathing modes, which are present in several cuprates with similar characteristics. The study of magnetic excitations, arising from spin-1/2 Cu atoms in the CuO_2 planes, shows that they reach an energy of approx. 300 meV at the Brillouin zone boundaries, that is, a value comparable to other cuprate

systems.

Keywords: high-temperature superconductivity, cuprates, $YBa_2Cu_4O_8$, charge density waves, magnetic excitations, resonant inelastic x-ray scattering

Abstract in lingua italiana

I cuprati sono una classe di superconduttori ad alta temperatura caratterizzati da una struttura a strati di CuO_2. Si tratta di superconduttori non convenzionali che presentano una simmetria di tipo d per il meccanismo di accoppiamento tra le cariche alla base della superconduttività. In diverse famiglie di cuprati sono state scoperte modulazioni periodiche della densità di carica elettrica associata agli elettroni di valenza, tipicamente con carattere unidirezionale. Esse prendono il nome di onde di densità di carica (charge density waves, CDWs). É stato inoltre confermato da molti studi che tali modulazioni di carica sono in diretta competizione con la fase superconduttiva.
Nel presente lavoro di tesi lo studio del cuprato $YBa_2Cu_4O_8$ (Y124) è stato eseguito tramite scattering inelastico risonante di raggi X (resonant inelastic x-ray scattering, RIXS) ad energia coincidente con lo spigolo di assorbimento L_3 del rame. Ad oggi, non esiste alcuna prova diretta dell'esistenza di CDWs in questo materiale. Tuttavia, l'osservazione di oscillazioni in esperimenti volti a mappare la superficie di Fermi e il valore del drogaggio simile a quello di altri cuprati dove le CDWs sono state rilevate rappresentano dei chiari segnali che questa fase ordinata possa esistere anche nel cuprato Y124. In effetti, dalle nostre misure è emerso un segnale relativo alle CDWs con caratteristiche simili a quanto osservato in altre famiglie di cuprati: l'analisi in energia dell'intensità quasi elastica conferma l'esistenza di una modulazione della carica elettrica connessa con gli elettroni di valenza dei piani di CuO_2. Inoltre, i dati raccolti lungo le direzioni H e K dello spazio reciproco dimostrano che le onde di densità di carica si sviluppano sia lungo la direzione a che lungo la direzione b dello spazio reale, con domini unidirezionali del tutto simili in forma e dimensioni a quelli osservati nel YBCO. Al contrario, dall'analisi in temperatura del segnale quasi elastico, sono emerse alcune differenze tra Y124 e il suo "parente" $YBa_2Cu_3O_{6+x}$ (Y123). É stato possibile associare l'andamento dell'intensità derivante dalle CDWs nell'Y124 a quello di un parametro d'ordine che descrive il rompersi di una simmetria. L'idea è che la stechiometria priva di difetti dell'Y124, in contrasto con i difetti intrinseci che si riscontrano nel contenuto di ossigeno nell'Y123, dovrebbe permettere alle CDWs di svilupparsi come una vera e propria transizione di fase del secondo ordine.

Sono stati inoltre raccolti spettri RIXS ad alta risoluzione energetica ($\Delta E \approx 35\,\mathrm{meV}$), i quali hanno permesso di studiare la dispersione delle eccitazioni magnetiche e dei fononi nello spazio reciproco. Dagli spettri è stato possibile estrapolare informazioni riguardo a due modi vibrazionali, il "buckling" e il "breathing", che corrispondono rispettivamente ad una flessione e ad un'estensione dei legami rame ossigeno. Tali vibrazioni del reticolo cristallino sono ritrovabili in altri cuprati con caratteristiche simili. Lo studio delle eccitazioni magnetiche, le quali emergono dagli spin degli atomi di rame nei piani di CuO_2, mostra come esse raggiungono un energia di circa 300 meV ai limiti della zona di Brillouin. Si tratta di un valore comparabile a quelli riscontrati in altri cuprati.

Parole chiave: superconduttività ad alta temperatura, cuprati, $YBa_2Cu_4O_8$, onde di densità di carica, eccitazioni magnetiche, scattering inelastico risonante di raggi X

Contents

Introduction

Cuprate superconductors were discovered in 1986 and from that moment on they have raised more and more interest. One reason is surely linked to the fact superconductivity appears at higher temperature values with respect to standard superconducting materials. This property results to be very appealing from the point of view of potential applications as there is the possibility to employ liquid nitrogen, instead of liquid helium, in the cooling process, thus avoiding the high costs and technical complications involved with the use of the last. At the same time, it was soon clear that cuprates materials show a huge complexity. The pairing mechanism which allows superconductivity to happen in cuprates is still not well-understood and it cannot be ascribed to the phonon-electron coupling as it is in conventional superconductors. Moreover, complexity is evident by looking at their phase diagram: by varying the doping level of the copper oxygen planes, common feature of the crystalline structure of all cuprates, and by changing temperature a rich variety of intertwined and overlapping phases arises. In addition to the superconducting phase, cuprates can be antiferromagnets, behave as Fermi-liquids or find themselves in the so-called pseudograp phase. Some of these phases can exist at the same time or compete against one another. The latter case is for example what happens between the superconducting phase and the phenomenon which goes under the name of charge order or, more specifically, charge density waves (CDWs). Charge order is a modulation of the charge density associated with Fermi electrons which is usually characterised also by a lattice deformation. This kind of phase was essentially observed in all cuprate families even though specific details vary from system to system. For instance, in lanthanum-based cuprates stripe-like CDWs appear with a periodicity which is a multiple of the underlying crystalline lattice periodicity, whereas in the Y123-family ($YBa_2Cu_3O_{6+x}$) incommensurate CDWs were observed. A close relative of Y123 is $YBa_2Cu_4O_8$ (Y124). The similar crystal and electronic structures between Y124 and Y123, the doping level close the the one where the CDWs are strongest, together with evidences of small electron pockets, are signs that the presence of charge order can be inferred in Y124 as well. Nevertheless, at present no direct proof of the existence of charge density waves in Y124 has been reported. Moreover, the experimental study of this cuprate would be valuable because Y124 possesses, differently

from Y123, a clean stoichiometry at all temperatures. Investigating charge order in Y124 and its properties will be the main goal of this thesis. This will be possible thanks to the powerful and highly versatile resonant inelastic x-ray scattering technique which ensures a way to study elementary excitations inside solids. We collected experimental at the ID32 beamline of the European Synchrotron (ESRF) where a pioneering high-resolution RIXS setup has been developed in collaboration with Prof. Giacomo Ghiringhelli and Prof. Lucio Braicovich from Politecnico di Milano.
In Chapter 1 I will give a brief introduction on high temperature superconductivity, but soon the attention will be directed to cuprate materials. After describing their crystalline structure, and their magnetic and electronic properties, the phase diagram of hole-doped cuprates will be extensively described. Due to the goal of the present thesis, a special care will be reserved to the superconducting state and charge order. I will provide a review of the discovery and properties of charge order in several cuprate families. Lastly, I will present previous relevant studies on $YBa_2Cu_4O_8$, the compound investigated in this thesis.
In Chapter 2 I will describe the resonant inelastic x-ray scattering (RIXS) by highlighting its advantages and versatility. I will discuss the RIXS process and the excitations which can be investigated. A brief theoretical treatment of the RIXS cross section will be provided as well. A second part will be devoted to the introduction to synchrotron radiation and to describe the instrumentation of the ID32 beamline at the ESRF, where the experimental data were collected. Lastly, the experimental scheme will be considered.
Chapter 3 will be dedicated to present and comment the experimental results. After an introduction to the samples and how experiments were performed, I will firstly focus on the investigation of charge density waves and their temperature dependence. A Lorentzian lineshape on the top of a linear background will be used to fit the energy integrated data. This way there will be the possibility to properly analyse the temperature dependence. Then, data fits of high-resolution measurements will be considered in order to study the dispersions of phononic and magnetics excitations in reciprocal space. The obtained results may be helpful for future studies and theoretical models on high-temperature superconductors akin quantum materials.
In the Conclusions I will provide some perspectives for future investigations.

1 | High-temperature superconductors and cuprates

In this first Chapter an introduction to high-critical temperature superconductors (HTS) will be given, also considering their historical importance in the field of condensed matter physics. Then, the focus will be put on a particular class of HTS, the cuprates. We will describe their crystal structure together with their magnetic and electronic properties. A final part will be reserved to a in-depth analysis of the double-chain superconducting cuprate $YBa_2Cu_4O_8$, whose experimental investigation by resonant inelastic x-ray scattering (RIXS) is the central focus of this thesis.

1.1. High-temperature superconductivity

Superconductivity is a macroscopic quantum phenomenon. Its peculiar physical properties, among others the infinitely high electrical conductivity, have attracted great interest of physicists and engineers. This phenomenon was discovered by Onnes [1] in 1911. He realised that the electrical resistance of mercury reaches an immeasurably small value when its temperature is brought below 4.2 K. In the subsequent years many other superconductors were found whose critical temperature, T_C, was below 20 K. Therefore, their possible applications would require the use of liquid helium (4.2 K).
Only in 1986 the first sample of high-critical temperature (HTS) superconductor was discovered in $La_{2-x}Ba_xCuO_4$. This kind of superconductivity had been hoped for many years since applications are feasible where SC can be achieved by cooling through liquid nitrogen (77 K). After the discovery of the first HTS, many more materials showing high temperature superconductivity were identified. In Fig. 1.1 an illustration of the most relevant HTS discovered throughout the years is reported, along with their superconducting transition temperatures. The cuprate compound with the highest critical temperature is a mercury-based copper oxide. It exhibits $T_C = 165$ K but only under specific conditions of high pressure. In 2015, studies on sulfur hydride H_2S, led by researchers of the Max-Planck-Institute for chemistry in Mainz (Germany), show that this system transforms

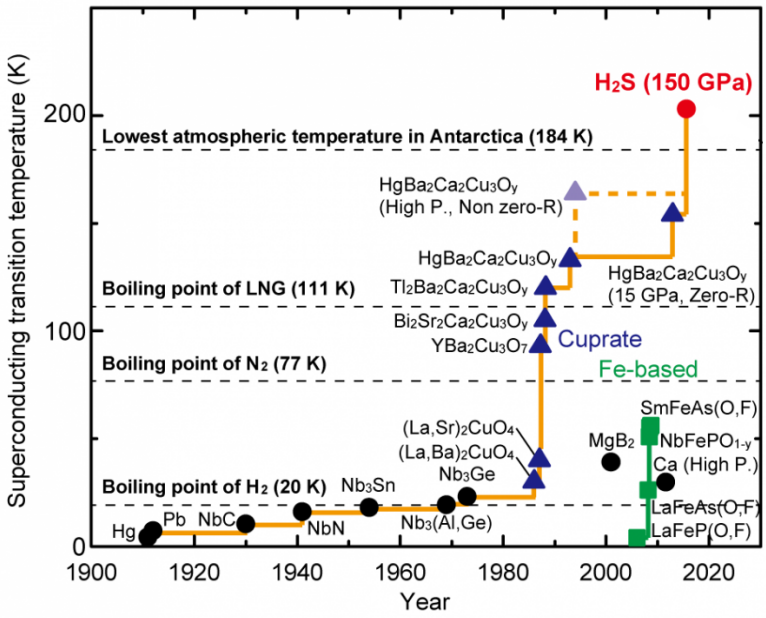

Figure 1.1: Superconducting critical temperatures versus year of discovery for different families of superconductors. Figure adapted from Ref. [2].

to a metal under a pressure of around 90 GPa. Furthermore, when pressure is approx. 150 GPa, probably due to the formation of the H_3S phase, this material is superconducting with a T_C of 203 K [3]. A last remark is about the first proof of room-temperature superconductivity. It was observed in a photochemically synthesised carbonaceous sulfur hybride (C-S-H system) in October 2020 [4]. Its critical temperature assumes a value of 15 °C at a pressure of 267 GPa.

A major characteristic of HTS is that most of them are unconventional superconductors. A superconductor is said to be conventional when its properties can be described and explained in the framework of the Bardeen–Cooper–Schrieffer (BCS) theory of superconductivity. By opposite, this theory fails in explaining how superconductivity works in unconventional superconductors. BCS theory, published in 1957 [5], is the first truly microscopic theory of the superconducting state. It is capable of making several predictions, such as the existence of an energy gap at the Fermi level below T_C, or explaining a number of important experimental phenomena, for instance the isotope effect [6]. The key idea of this theory is that an effective attraction exists between the electrons with energy close to the Fermi level. Cooper [7] suggested that an electron, during its motion inside the solid, has an impact on the positions of the ion cores and, thus, it causes a deformation of the lattice. This is due to the electric charge carried by the electron. A second electron can

feel an attractive force due to the increased density of positive charges associated with the ion cores. Overall, the two electrons attract each other via this weak interaction mediated by the lattice deformation. The electron pair goes under the name of Cooper pair. In a quantum framework, lattice vibrations can be described by quasi-particles called phonons. Then, it is possible to refer to this interaction as electron-phonon coupling. The electron-phonon interaction is crucial because it is able to provide a microscopic explanation of superconductivity in conventional superconductors. H_2S, despite being a HTS, is a BCS-supercondcutor. Its incredible high T_C is justified by the extremely light mass of hydrogen and the consequent high-energy lattice vibrations [8]. Nevertheless, the majority of HTS, cuprates included, belongs to the class of unconventional superconductors. Their high superconducting critical temperature cannot be explained in the frame of BCS theory, since the energy provided by the electron-phonon coupling is too weak to account for the energy scale associated with their higher T_C.. Another more energetic, many-electron interaction should be responsible for the formation of the superconducting ground state below T_C. At present, even though various theories were proposed, mostly supporting spin fluctuations as glue for the Cooper pairs, high-temperature superconductivity remains ones of the main unsolved problem in condensed matter physics. That is why the investigation of cuprates results to be so fascinating and it could contribute to unveil the mechanisms at the heart of HTS.

1.2. Cuprates

Since their discovery in late 1986, cuprates have attracted more and more interest. Their high critical temperature would allow several potential technological applications. Even though the physical mechanism underlying superconductivity in such materials is not still completely clear, various experimental evidences seem to suggest that some theories are more plausible than others. Hereafter, experimental findings informing these theories will be described. This section will mainly focus on the crystal structure of cuprate materials and their electronic, magnetic and superconducting properties. Cuprates can be divided into families, according to their chemical composition. Our attention will be primarily directed to the Yttrium Barium Copper Oxide (YBCO) family.

1.2.1. Crystal structure

Cuprate superconductors possess a crystal structure which is derived from the ideal perovskite structure. Perovskites are ceramics described by the generalised formula ABX_3. Their structure is depicted in Fig. 1.2. Cation B is in 6-fold coordination and is sur-

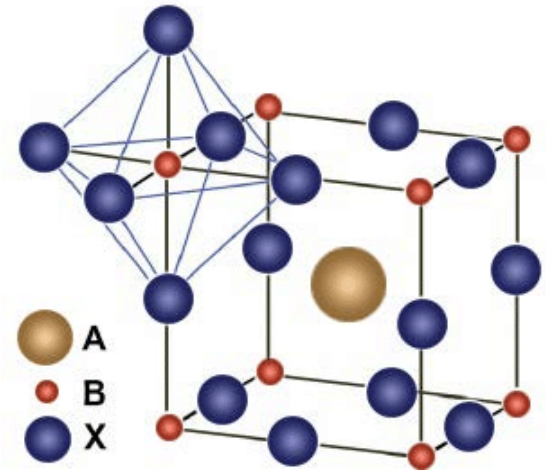

Figure 1.2: The general structure of a perovskite material. Figure taken from Ref. [9].

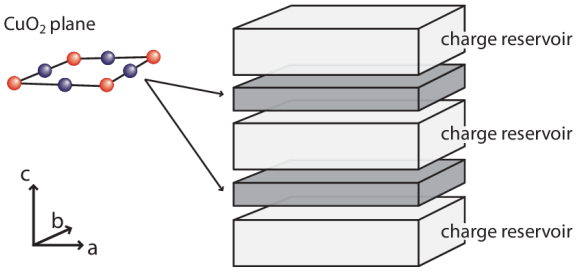

Figure 1.3: The general structure of a cuprate material as the alternation of CuO_2 planes and charge reservoir layers. Figure taken from Ref. [10].

rounded by an octahedron of X anions. Cation A finds itself in the middle of the cube defined by B ions.

Fig. 1.3 can help visualise the crystal structure of cuprate materials. The common feature of all cuprate families is a layered structure which consists of CuO_2 planes. Between these planes other layers are located, which contain oxygen and one or more heavy atoms (such as Hg, Ba, or rare earths). These take the name of charge reservoirs. Although the superconductivity and many of the physical properties of cuprates are strictly related to the CuO_2 planes, the interaction of these planes with the intermediate layers is of crucial importance in determining such properties.

To date a large variety of different cuprate compounds is known. The difference between the various systems lies in the composition of the intermediate layers or in the number N of consecutive CuO_2 layers. Indeed, a possible distinction of cuprates is based on N. We can classify them as monolayer, bilayer or trilayer compounds, etc. Due to the layered structure, it is evident that a substantial anisotropy is present between the in-plane axes (a and b) an the out-of-plane axis (c). The presence of the out-of-plane apical oxygen atoms gives rise to Cu-O octahedra. The typical distance between the CuO_2 planes and the apical oxygens is in the order of 2.3 Å–2.7 Å, instead the Cu-O in-plane distance is approx. 1.91 Å–1.94 Å.

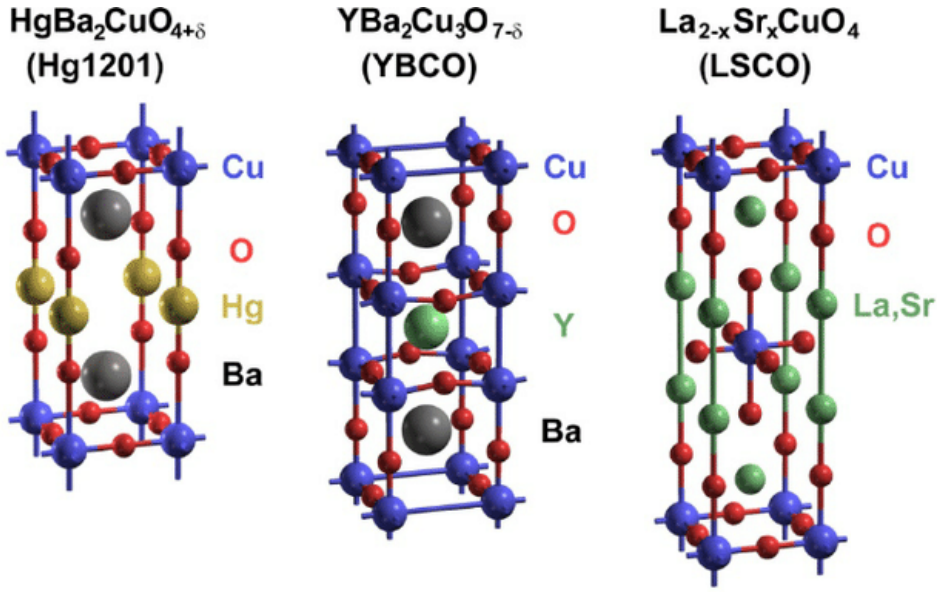

Figure 1.4: Crystal structure of selected monolayer cuprates. Figure adapted from Ref. [11].

1.2.2. Electronic and magnetic properties

The heart of cuprates is represented by the CuO_2 planes. Here, copper ions are nominally divalent (Cu^{2+}), i.e., they possess a $3d^9$ electronic configuration. They are surrounded by four in-plane oxygens which, considering a situation with full $2p$ orbitals, are O^{2-} ions. A $3d^9$ configuration means that only one electron is missing to complete the $3d$ shell. It is much simpler, rather than dealing with nine electrons and thus a many-body problem, to consider the $3d$ shell as populated by a single hole. More specifically, this hole is going to occupy the $3d_{x^2-y^2}$ orbital as depicted in Fig. 1.6. Since the copper ion lies in the middle of an octahedral environment, given by the eight surrounding oxygens, the spherical symmetry is broken and the five $3d$ states are not energetically degenerate anymore. In the framework of the crystal field model [12], this is explained in terms of electrostatic interaction: a substantial overlap of $3d$ orbitals with surrounding orbitals, which are the $2p$ oxygen orbitals in the case of cuprates, brings to a higher energy level due to the repulsion between electrons. Thus, considering the situation in the xy-plane (shown in Fig. 1.5), d_{xy} orbital is energetically favourite with respect to $d_{x^2-y^2}$. Moreover, the copper ion in cuprates lies in a distorted octahedral environment, with apical oxygens farther from the CuO_2 planes than in a regular octahedron. As a consequence, due to the smaller overlap, orbitals with z-component are lowered in energy. Therefore, the nine copper electrons (Cu^{2+}) will occupy all the $3d$ levels leaving a hole in the $3d_{x^2-y^2}$ state, the most energetic one. Thanks to resonant inelastic x-ray scattering (see Chapter 2) it is

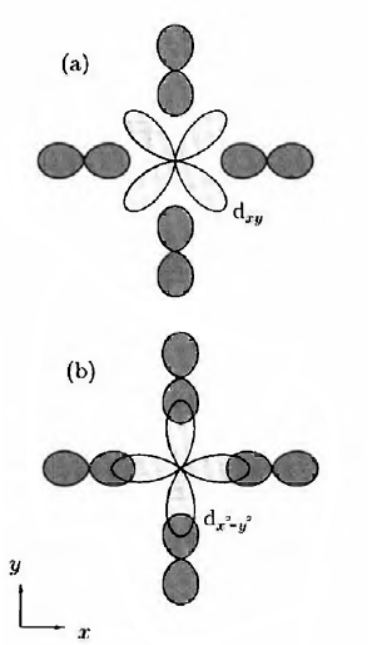

Figure 1.5: Spatial distribution of d_{xy} (a) and $d_{x^2-y^2}$ (b) orbitals and overlapping with surrounding orbitals in a octahedral environment. Figure taken from Ref. [12].

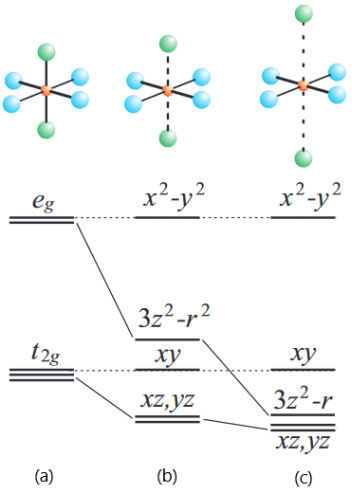

Figure 1.6: Illustration of the $3d$ levels splitting in a octahedral environment. (a) is the case of a regular octahedron, whereas (b) and (c) show a distorted octahedron with apical oxygen atoms farther from the xy-plane. Figure adapted from Ref. [13].

possible to obtain information about the energy and the symmetry of *dd* excitations and determine the Cu electronic configuration. Furthermore, values of effective crystal field parameters can be inferred [13].

From the point of view of the magnetic behaviour, each copper ion is carrying a spin 1/2 given by the single hole in the $3d_{x^2-y^2}$ orbital. The superexchange interaction between these spins, typical of various ionic solids such as fluorides and oxides, is crucial for the physics of cuprates. Superexchange is an indirect exchange interaction between non-neighbouring magnetic ions which is mediated by a non-magnetic ion which is placed in between the magnetic ions [14]. The result is that there is an energetic advantage in forming an antiferromagnetic (AFM) ground state. A brief explanation can be found in the caption of Fig. 1.7, where, for the sake of simplicity, the case of a magnetic moment due to a single unpaired electron on the transition metal atom M is considered. In the case of cuprates, the magnetic ion is copper and the non-magnetic ion is oxygen. Below Néel temperature, around 300 K in layered cuprates, the Cu^{2+} spins are ordered antiferromagnetically. The strong interaction between electrons is at the basis of the electrical behaviour of undoped cuprates. They can be classified as Mott insulators [15]. Such materials should be metallic according to band theory, but actually they exhibit insulating character. Band theories fail because one of their fundamental assumptions is

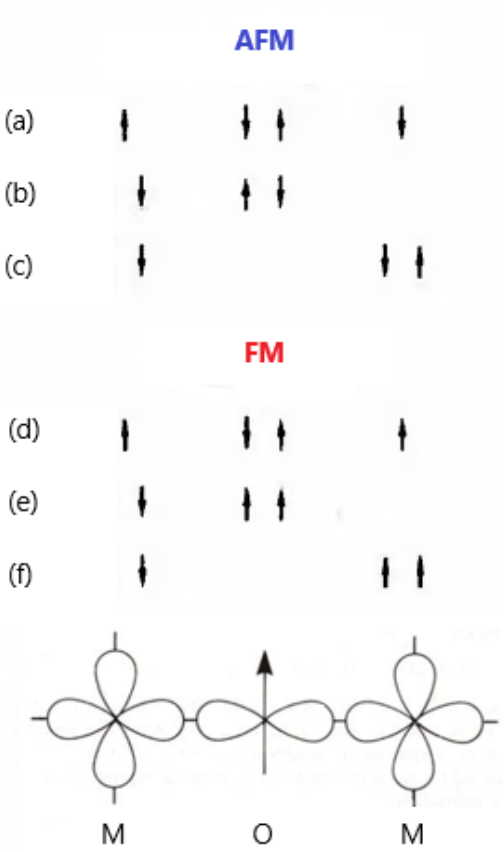

Figure 1.7: Superexchange in a magnetic oxide. In a purely ionic picture, the oxygen would have two electrons in the $2p$ orbital and the ion M a single unpaired electron in a d orbital. If the spins on M ions are antiferromagnetically oriented, electrons can jump between B and O since the exclusion principle is respected. The ground state (a) can be mixed with (b) and (c) which are excited configurations. Thus, the unpaired M electrons result to be delocalised over the M-O-M unit and an energy advantage is gained. Vice versa, if a ferromagnetic coupling took place between the M unpaired spins, only the ground state (d) would be possible as the excited states (e) and (f) are forbidden by the Pauli principle. The FM configuration is energetically unfavourable. Figure adapted from Ref. [14].

to neglect the interaction between electrons and other electrons, phonons, etc. and thus giving rise to single-electron states. In cuprates, the addition of a second electron to the $3d_{x^2-y^2}$ costs a great amount of energy, usually referred as the on-site Coulomb repulsion energy U. Cuprates are strongly correlated electron systems, where the motion of one electron is inevitably subject to the presence of all the other electrons. One important consequence of Coulomb and superexchange interactions is the 2D nature of the electronic and magnetic physical properties in cuprates. Schematic representations of the direct and reciprocal bi-dimensional spaces are shown in Fig. 1.8. Due to the AFM order, the nuclear and magnetic first Brillouin zones do not coincide: since in the real space the magnetic period is twice the distance between two neighbouring Cu atoms, in the reciprocal space the magnetic period will be half of the nuclear period.

When the case of doped cuprates is considered, the long-range spin order is destroyed and, below critical temperature, the superconducting phase arises. This mechanism is going to be clarified soon. But before it is important to say that magnetic fluctuations do not disappear and they can still play an essential role for superconductivity even above T_C. Although the long-range AFM order is destroyed, spins have still the possibility of creating local arrangements of magnetic moments if the exchange length is large enough.

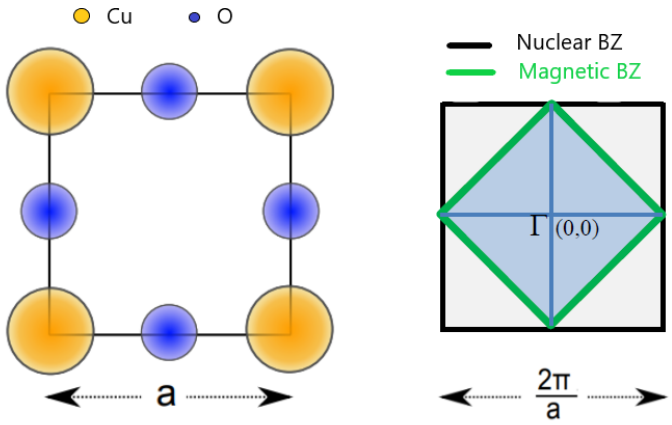

Figure 1.8: On the left, real space of a CuO_2 plaquette. On the right, both the corresponding nuclear and magnetic Brillouin zones in the reciprocal space. a is the distance between two neighbouring Cu ions. Figure adapted from Ref. [16].

Therefore, spin fluctuations survive in the form of damped magnons, i.e., paramagnons. Many of the theories which try to explain the mechanism at the base of HTS consider these magnetic excitations as the possible acting force that drives the pairing mechanism [17]. Indeed, one observation is that high-T_C superconductors are strong spin-density wave systems and the superconducting phase is close to a magnetic transition, usually towards an AFM phase.

1.2.3. Hole-doped cuprates and phase diagram

Let us focus now on the case of doped cuprates. The doping is realised through the charge reservoir layers. Indeed, acting on their chemical composition allows to control the number of electrons in the CuO_2 planes. More precisely, the doping quantifies the extra-electrons or extra-holes per planar Cu atom. We refer to this two cases as electron-doped and hole-doped cuprates, respectively. The manipulation of the doping can be achieved either by replacing one atom in the charge reservoir layer with another of different valence or by adding oxygen. The former strategy is used, for instance, in LSCO, where La is replaced by Sr or Ba. The latter is used in the 123 family: the symbol δ in the formula $YBa_2Cu_3O_{6+\delta}$ indicates the degree of oxygenation in the buffer layer. The buffer layers can also act as blocking layer preventing electronic transfer between consecutive CuO_2 planes.

From now on we will just focus on hole-doped cuprates. Looking at the phase diagram

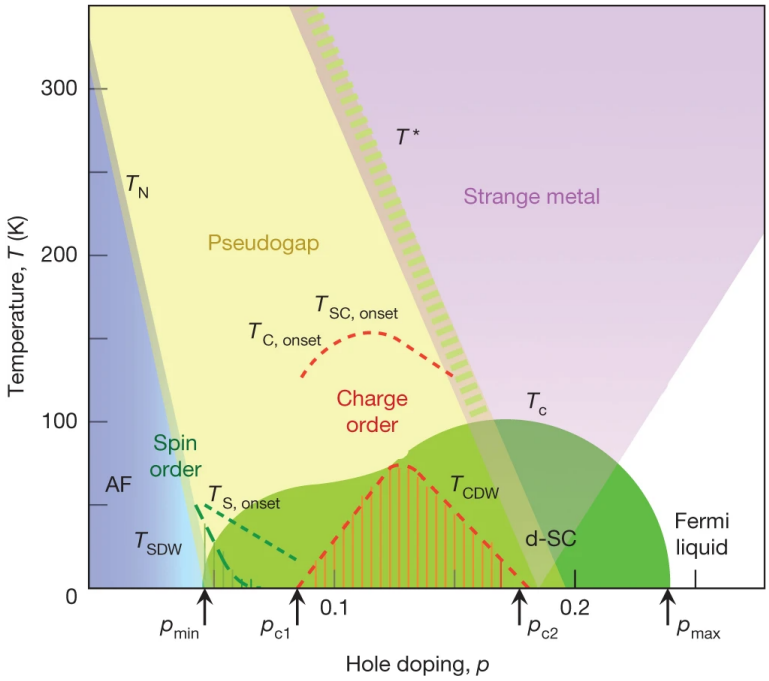

Figure 1.9: Phase diagram of hole-doped cuprates as a function of temperature and doping level. T_N and T_C indicate the antiferromagnetic Néel and the superconducting critical temepratures, respectively. Figure taken from Ref. [2].

in Fig. 1.9, where the main phases of hole-doped cuprates are reported, one can realise that the hole doping (p) quickly suppresses the antiferromagnetic order until the superconducting state appears in the range $0.05 \leq p \leq 0.27$. The superconducting transition temperature varies with p and it is possible to identify an optimal doping value p_{opt} for which T_C is the highest. p_{opt} allows to distinguish between underdoped ($p < p_{opt}$) and overdoped regimes ($p > p_{opt}$).

The addition of charges causes the loss of the long-range AFM order. One can verify this by making a comparison between the spin textures for the undoped and for the hole-doped cases, respectively in Fig. 1.10 and Fig. 1.11. Let us consider the latter case. Focusing on a copper ion surrounded by the four in-plane oxygens, the added hole carries an opposite spin with respect to the one in the Cu due to its unpaired electron. Nevertheless, it seems that the extra-hole is not localised on the Cu site, but rather delocalised over the four neighbouring oxygens in the xy-plane (Fig. 1.11). This entity can be seen as a new quasi-particle characterised by zero net spin and named as Zhang-Rice singlet (ZRS) after his proposers Zhang and Rice [18]. As in BCS theory the coupling between two electrons of opposite spin gives rise to a zero-spin Cooper pair, the propagation of such ZRS particles along the CuO_2 planes could be the possible mechanism at the heart of HTS in cuprates.

The difference paring mechanism between charges in BCS-superconductors and cuprates

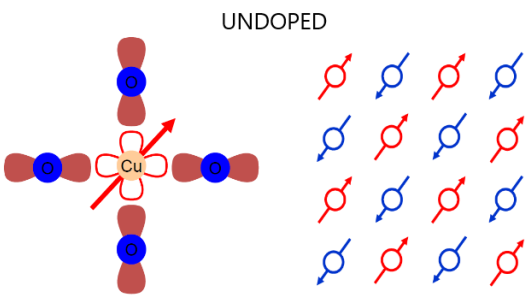

Figure 1.10: Spin configuration for an undoped cuprate where each Cu ion is carrying a single hole (Cu^{2+}, $3d^9$). Figure taken from Ref. [19].

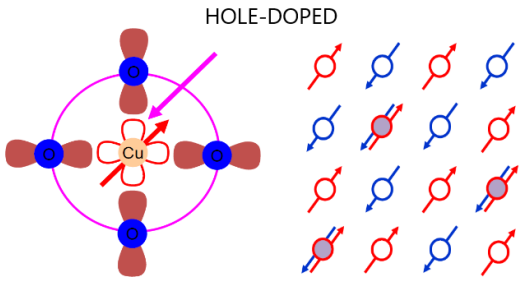

Figure 1.11: Spin configuration for the hole-doped cuprate: the added holes destroy the AFM order. Figure taken from Ref. [19].

is responsible for further dissimilarities in the superconducting properties. The wave-function of the SC state is characterised, as all wave-functions, by a spin and an orbital components. Cooper pairs in conventional superconductors finds themselves in a singlet state, whereas the spatial part of the wave-function shows s-wave symmetry. That is why they are also referred to as s-wave superconductors. Their SC gap, i.e., the region depleted of density of states around the Fermi energy below T_C, is isotropic. On the other hand, in cuprates, if the spin part is still a singlet ($S = 0$), in order to have a total antisymmetric wave-function (electrons are fermions), the orbital component must be even ($L = 0, 2...$). Experimental evidences exist which prove what cuprates are d-wave superconductors ($S = 0, L = 2$). From a general point of view, the SC order parameter can be described by the complex quantity $\Delta(\mathbf{k})e^{-i\phi(\mathbf{k})}$) [20]. Here, $\Delta(\mathbf{k})$ is the magnitude of the SC gap, which can be interpreted, in broad terms, as the energy needed to break a Cooper pair in a BCS-supercondcutor. Instead, $\phi(\mathbf{k})$ is the phase of the order parameter. This is crucial to describe the SC ground state which is the result of a Bose-Einstein-like condensation [21] of the SC carriers in the same quantum state. Both gap and phase can show a dependence on the position in the reciprocal space, that is, the momentum $\mathbf{k}$. For BCS-superconductors the magnitude of the order parameter is simply a constant and the phase is fixed in all directions, that is, the order parameter is isotropic. Whereas for cuprates the order parameter is anisotropic with a d-wave symmetry: it changes sign upon a 90 deg rotation and, thus, the SC gap must be identically zero at the boundary of these regions. More specifically, for cuprates the symmetry results to be $d_{x^2-y^2}$ and the four nodal directions coincide with the diagonals of the first Brillouin zone in reciprocal space. Information about the SC gap can be retrieved through different experimental techniques. One possibility is to exploit a superconducting quantum interference device (SQUID) [22].

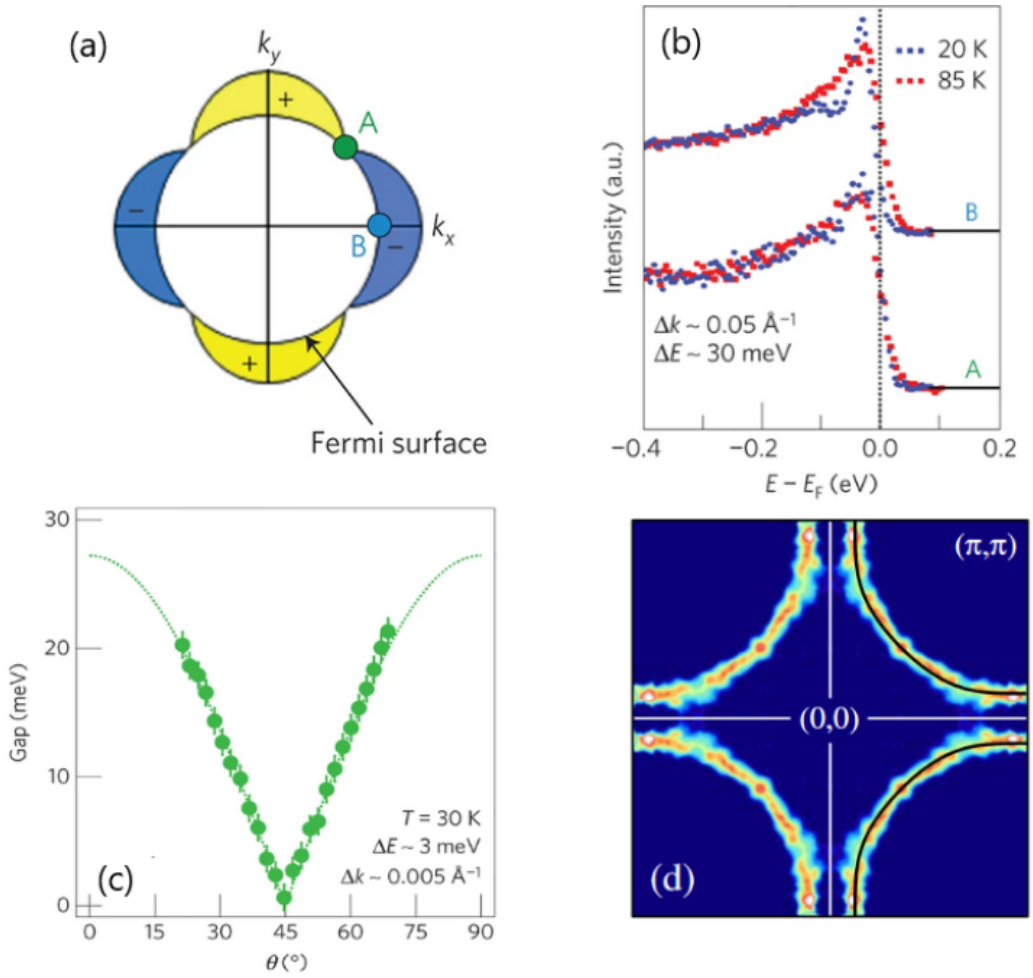

Figure 1.12: (a) Schematic of a $d_{x^2-y^2}$-symmetry order parameter on a circular Fermi surface (A and B are a nodal and an antinodal points, respectively). (b) Anisotropy in the SC gap first observed in $Bi_2Sr_2CaCu_2O_{8+\delta}$ [25]. (c) SC gap measured close to a nodal point by ARPES in $Bi_2Sr_2CaCu_2O_{8+\delta}$. (d) Fermi surface in $Tl_2Ba_2CuO_{8+\delta}$ by ARPES. Figures (a), (b) and (c) taken from Ref. [26], figure (d) taken from Ref. [27].

Its working principle is based on the presence of Josephson's junctions, that is, two superconductors materials which are separated by an insulator. Since the output of this device is strongly affected by the SC order parameter phase, it is possible to verify if the phase shows some momentum dependence by making the junctions on different crystallographic faces [23]. Another way to probe the SC gap is given by angle-resolved photo-emission spectroscopy (ARPES) [24]. It is a a photon-in electron-out technique which gives the possibility of mapping the electronic band structure and the Fermi surface of materials by measuring the energy and the angle distribution of the ejected photoelectrons. Experimental results by ARPES, as those shown in Fig. 1.12, provide a definitive answer on the topic of gap size and symmetry. In panel (a) an illustration of a $d_{x^2-y^2}$ symmetry

order parameter on a circular Fermi surface is depicted. Point A is a node, whereas point B, where amplitude is the biggest, is an antinode. Panel (b) shows the first observation (1993) of the anisotropy in the SC gap in a sample of $Bi_2Sr_2CaCu_2O_{8+\delta}$ (Bi2212) [25]. The bottom data are related to a nodal point (A), instead the top data concerns an antinode (B). One can observe that in the former case there is no clear difference between the measurement at 85 K (few Kelvins below T_C) and the measurement at low temperature (20 K): they both cross the Fermi level (E_F) in the same way. For the latter case, instead, the low-temperature data cross the Fermi level at a lower intensity than the high-temperature data, indicating a lower density of states at E_F and the aperture of gap. These data distinctly show the anisotropy of the SC gap: below T_C, while moving from the antinode towards the node (45 °), the size of the SC gap gradually decreases. It must be zero at the node since a sign change of the order parameter occurs. This is represented in panel (c), where the trend of the SC gap size, close to a nodal point, is provided. Lastly, in panel (d), the bi-dimensional Fermi surface, measured more recently (2010) by ARPES, is illustrated in the (k_x, k_y)-plane.

Looking again at the phase diagram of Fig. 1.9, we have already discussed the antiferromagnetic phase, present at low doping levels, and the superconducting phase. *Charge order* phase, corresponding to the red shaded area in the phase diagram, is the main subject of this thesis and thus will be described separately in Section 1.2.4. The remaining phases will be briefly described hereafter.

To the right of the AFM region and above the underdoped SC region, the so-called *pseudogap* phase occurs. It survives up to much higher temperatures than T_C. In the diagram this upper temperature is indicated as T^* and it depends on the doping level. Also in this case, ARPES remains the tool of choice to investigate the pseudogap phase properties. Indeed, a strong momentum anisotropy in the density of occupied states characterises this phase. This is clear from Fig. 1.13. It shows the experimental results obtained by ARPES on the underdoped Bi2212 [26]. For the purpose of stressing the existence of a gap, the energy distribution curves have been symmetrised with respect to the Fermi energy (E_F). Below T_c (95 K), in panel (a), all the curves taken at different angles (i.e., at different points in the momentum space) present a dip. These are referred as "gapped momenta" and one can notice that the gap is wider at lower angles. Nevertheless, there is an exception: at 45 °, that is, along the diagonal in the reciprocal space, the curve shows a single peak at k_F and no gap exists here. We can talk about "ungapped momenta". Plotting the SC gap as a function of the Fermi angle a simple *d*-wave form is obtained (blue dashed line in panel (c)). This is consistent with the previous discussion about the SC gap. However, unexpected results arise when the temperature is above T_C, as panel (b) displays. For low angles, a gap feature is still present although

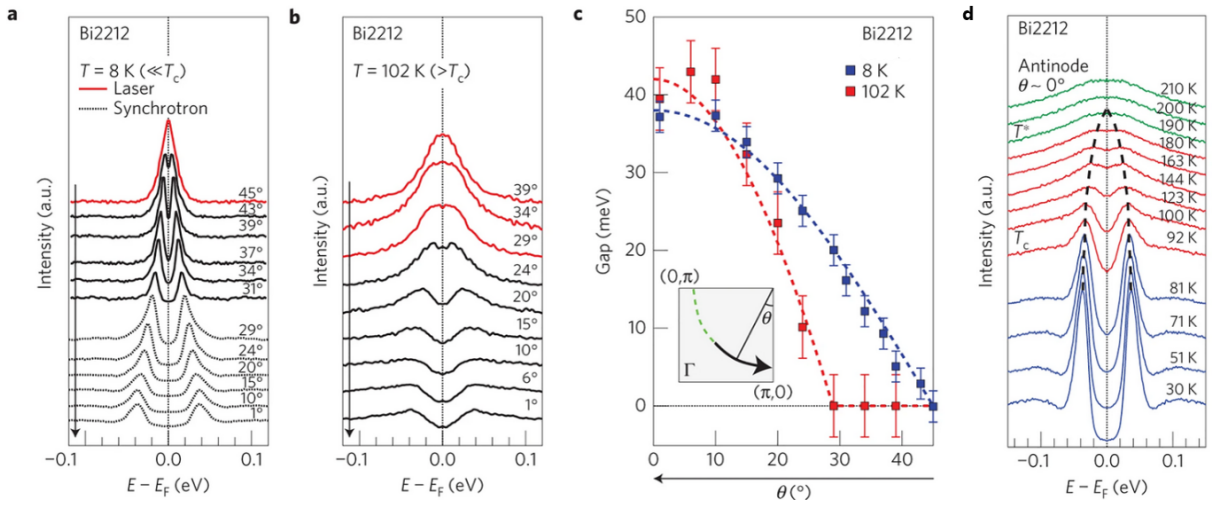

Figure 1.13: (a) and (b) show, respectively, low-temperature and high-temperature measurements by ARPES on Bi2212 samples ($T_C = 95\,\mathrm{K}$). Data consist of energy distribution curves symmetrised with respect to the Fermi energy and collected along different directions in the momentum space. (c) Energy gap size as a function of the Fermi angle θ for both the low-T (blue) and high-T (red) cases. The former trend is d-symmetric, as expected below T_C, whereas the latter is the pseudogap case where the gap is vanishing in an extended region around the nodal point. (d) Temperature dependence of the energy curves at the antinode: the energy gap does not disappear at T_C, but only above T^*. Figures taken from Ref. [26].

one may expect to find a simple metallic normal state above T_C. Instead, close to the nodal region, the gap is vanishing as single peaks appear at k_F. Thus, the pseudogap shows a strong similarity with the d-symmetry of the SC gap with the difference that the latter is vanishing not only at the node but in an extended region around it. This is visible both in panel (c) (red-dashed line) and in the 3D illustration in Fig. 1.14 (a), accompanied by a simple formula describing the SC gap trend. The regions around the nodal point, where the gap is missing, are referred as "Fermi arcs". They are displayed in panel 1.14 (b). Upon increasing temperature, the Fermi arcs expand more and more in the reciprocal space until they almost reach the antinodal direction. The temperature at which this occurs is the pseudogap temperature T^*. For Bi2212 T^* is approx. 190 K since this is the first temperature value when the dip in the energy distribution curves at the antinode disappears. One can observe this in Fig. 1.13 (d). Just as a reference, the different features shown by the energy gap at nodal and antinodal regions are referred to as "nodal-antinodal dichotomy" of the energy gap. This divergence vanishes only for $T > T^*$, when the full Fermi surface is recovered.

A possible interpretation of the divergences from the point of view of momentum, temper-

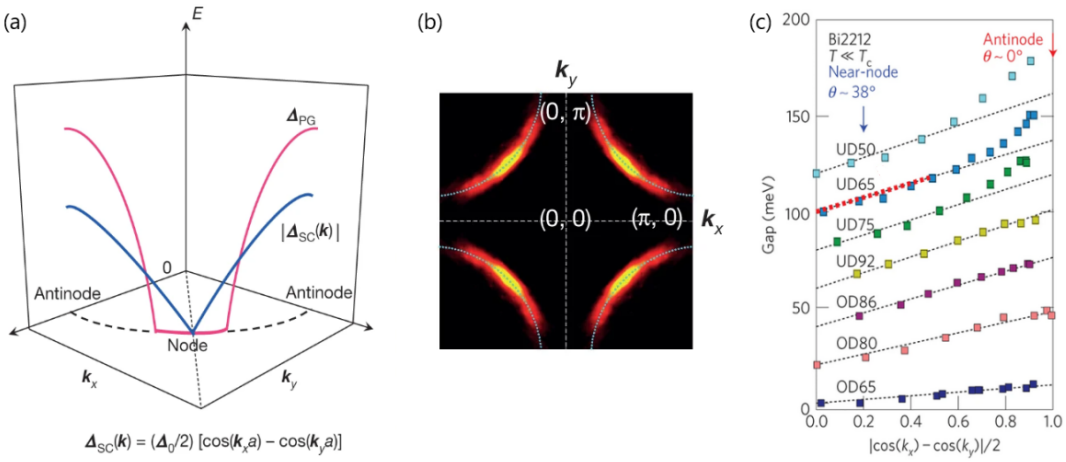

Figure 1.14: (a) 3D illustration in the momentum space of the energy gap trend for both the SC gap and the pseudogap. A formula to analytically describe the SC gap trend is provided. It underlines the d-symmetry of the SC gap. (b) Bi-dimensional Fermi surface for the pseudogap phase: the Fermi arcs are highlighted. (c) Doping dependence of the energy gap below T_C as a function of the d-wave form factor. Data related to different doping levels are vertically shifted. The dashed line indicates a d-wave form of the gap. (UD: underdoped, OD: overdoped, numbers indicates the T_C). Figures taken from Refs. [2, 26].

ature and also doping [26] dependences of the energy gap can be found in the simultaneous existence of two distinct orders [28, 29]. Far below T_C, the d-wave symmetry of the nodal region is mostly due to the superconducting order parameter, whereas the pseudogap order parameter can already have an influence on the gap opening in the antinodal region. At higher temperatures, the gap loses the symmetry typical of the SC phase indicating that the pseudogap order parameter becomes the dominant one in that temperature range. In this framework, the doping dependence of the energy gap (panel (c) of Fig. 1.14) can be accounted as well. In the underdoped regime the strong discrepancy from a simple d-wave trend is explained by a bigger amplitude of the pseudogap order parameter which completely dominates the SC one in the antinodal region. Vice versa, the SC symmetry is maintained for the overdoped regime, indicating a different relative strength between the magnitudes of the order parameters in this region of the phase diagram.

To sum up, pseudogap and superconducting phases can be seen as interplaying and competing orders. However, it is well-documented that the pseudogap region is rich of several arising orders beyond superconductivity. The term "order" indicates any pattern of broken symmetry. Among these, we mention charge orders (see Sec. 1.2.4) and quantum liquids, especially quantum nematic liquid crystal. Nematicity is an electronic state where rota-

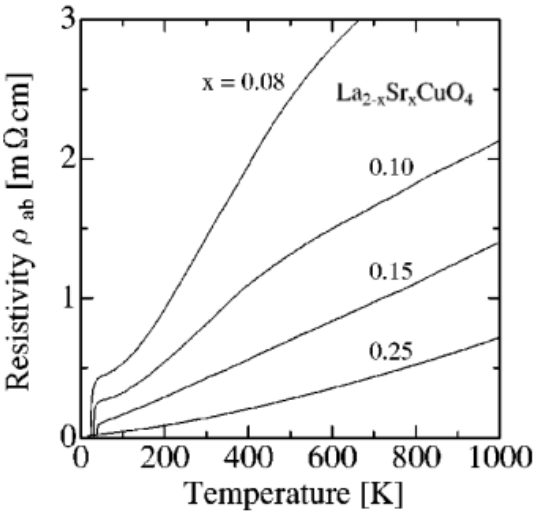

Figure 1.15: In-plane resisitvity of the cuprate $La_{2-x}Sr_xCuO_4$ for different strontium concentrations up to 1000 K. Resistivity is linearly increaing without any saturation.. It is recognisable the onset of superconductivity when resistivity drops to zero. Figure taken from Ref. [34].

tional symmetry is broken while preserving translational invariance [30]. For instance, in $YBa_2Cu_3O_{6+\delta}$ a transition from C_4 down to C_2 rotational symmetry of the copper oxygen planes was observed in the pseudogap region near T^* [31].

The *strange metal* phase arises when temperature is raised above T^* and towards high doping levels. This phase does not appear only in copper oxides, but it is typical of many materials with high electronic correlation. The fundamental difference with a normal metal is the absence of quasiparticles in the strange metal phase [2]. This obviously has big repercussions on the physical properties, first among all the electrical resistivity ρ. In a conventional metal ρ exhibits a saturation in the high-temperature regime. This arises when the electron de Broglie wavelength λ and mean free path l reach the same order of magnitude. A complete different behaviour characterises a strange metal since its electrical resistivity shows a linear trend starting from near T_C up to the melting point, even when $l < \lambda$. The temperature dependence of the resistivity in $La_{2-x}Sr_xCuO_4$ is shown in Fig. 1.15. A further discrepancy from the conventional metal behaviour (as described by the Landau Fermi-liquid theory) is related to the optical conductivity, which in a strange metal does not exhibit a Drude-like frequency trend, but it goes as $\sigma(\omega) \sim 1/\omega$ [32]. Although no microscopic theory exists which is able to explain the physical properties of this region of the phase diagram, the so-called Marginal Fermi Liquid (MFL) theory [33] provides a successful phenomenological framework.

The phase left to be described is the *Fermi Liquid* phase. We find it when doping is

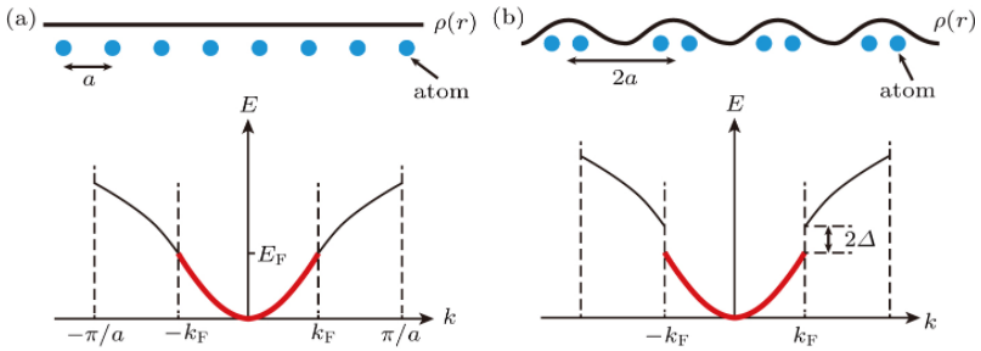

Figure 1.16: Peierls instability in a 1D metallic system. (a) Above Peierls temperarature the system exhibits a constant charge density $\rho(r)$ and electronic levels are filled up to the Fermi level E_F. (b) When temperature is brought below Peierls temperature, the system gains energy by doubling the lattice period. Energy gaps appear at E_F together with a periodically modulated charge density. The characteristic period of $\rho(r)$ is $2k_F$. Figure taken from Ref. [37].

increased beyond the optimal SC doping, in the overdoped regime. As doping is increased, experiments show that the full Fermi surface is restored [35]. RIXS data have highlighted the existence of spin fluctuations at smaller wave vectors [16], indicating that overdoped cuprates are still highly-correlated electrons systems [2]. The concept of Fermi liquid was firstly introduced by Landau. Such a system is composed of strongly interacting particles and has an unbelievably complex ground state wave function. Nevertheless, the fundamental idea of Landau's theory is that the excitations related to this ground state behave as weakly interacting particles or quasiparticles [20]. Inelastic nutron scattering (INS) measurements [36] have reported a pronounced decrease of the magnetic spectral intensity in correspondence of the AFM wave vectors in this phase. This could explain the drop in the SC critical temperature as a result of the lack of the spin-fluctuation pairing force [2]. The transition from Fermi liquid to strange metal is still not so well-understood, especially at low temperatures, as only a weak crossover exists between these two phases.

1.2.4. Charge order in cuprates

Charge order indicates a phase where charges self-organise into superlattice structures. Since resonant inelastic x-ray scattering (see Chapter 2) allows to probe all different kinds of degrees of freedom - lattice, orbital, charge and spin - it is the ideal technique to collect information on elastic and inelastic scattering signals associated with this phase. The high-electronic correlation which characterises cuprate systems could be the driving mechanism behind the appearance of charge order. Indeed, the strong on-site electronic

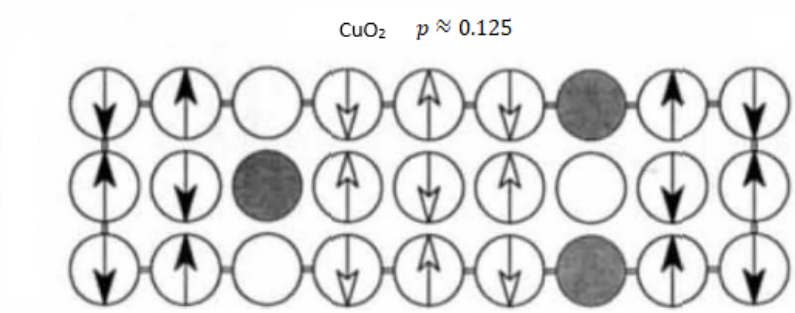

Figure 1.17: Real space representation of the stripe order in LNSCO. Only metal atoms are represented. A filled circle indicates the presence of a doped hole centred on a metal site. Figure taken from Ref. [40].

repulsion between electrons occupying the same d orbital can favour the spontaneous breaking of the original lattice symmetry. For instance, valence electrons can bring an energy gain to the whole system by giving rise to periodic patterns. When charge order takes the shape of a periodical modulation of valence charges, typically with unidirectional character, is usually referred to as charge density waves (CDWs). The first speculation about their existence dates back to 1930s when Rudolf Peierls noticed an electronic instability in pure 1D metals. Indeed, below a characteristic temperature, the system has an energetic advantage in doubling the lattice constant. The net results are the opening of an energy gap at the Fermi level and the formation of an electronic modulation of wave vector $2k_F$, where k_F is the Fermi wave vector. A schematic illustration related to Peierls intsability is provided in Fig. 1.16. Peierls transitions have been observed in several systems characterised by a quasi-2D physics. Layered transition metal dichalcogenides are an example. Dichalcogenides are semiconductors of chemical formula MX_2, where M is a transition metal atom and X is a chalcogen atom (S, Se or Te). In these compounds charge order appears in the form of quasi-2D CDWs. One of the models introduced to describe this phenomenon is Fermi surface nesting (FSN) [38]. FSN key idea is that vectors connecting the Fermi surface zone boundaries can be related to the characteristic wave vectors of CDWs. For instance, an experimental confirmation is represented by ARPES measurements on 2H-$NbSe_2$, which demonstrate the good agreement between nesting and CDW vectors [39].

The existence of a charge order phase have been revealed in many other systems, including cuprates. The first indirect experimental proof of charge order in cuprate systems dates back to 1995. Tranquada *et al.* [40] carried out inelastic neutron scattering (INS) measurements on LSNCO ($La_{2-x}Sr_xCuO_4$ with partial replacement of La by Nd atoms) with a doping level $p \approx 1/8$ per square-lattice unit cell. Neutrons are neutral particles

but, thanks to their intrinsic magnetic moment, they can interact with the electronic spin, revealing information about the magnetic structure. Bragg peaks with $8a$-periodicity were found in the INS data and this modulation was ascribed to the existence of a magnetic superstructure of spins. Later, scattering experiments with x-rays (see e.g. [41]) allowed to make the connection between spin order and another set of reflections characterised by four-unit-cell ($4a$) modulation. Here a is the square lattice parameter. This second modulation picked up by x-rays was ascribed to charges and, in particular, to valence charges. Magnetic and charge order interplay: the doped holes find themselves in 1D-structures which separate nanoscale domains where AFM order is established. Holes are delocalised in such structures. The term *stripe order* was chosen to describe this phase and, more generally, it indicates an electronic ground state where the mutual interaction of charge and magnetic order is accompanied by certain geometrical constraints on the ordering wavevectors [42]. Fig. 1.17 depicts the schematic illustration of the stripe order in LSCO. A further remarkable result is that the superconducting critical temperature experiences a dramatic reduction for this doping level ($p \approx 1/8$). It was soon clear that this peculiar phase is typical of La-based cuprates belonging to the so-called 214 family. Their structure is characterised by slightly distorted octahedra around the Cu atoms and this brings to the stabilisation of the stripe phase [43]. INS measurements on other cuprates, such as those belonging to the 123 family, did nor reveal any magnetic modulation which could be linked to the stripe order.

Huge improvements in scanning tunnelling microscopy (STM) led to the discovery of charge order in a different cuprate family. In 2002, Hoffman *et al.* [44] carried out STM measurements on slightly overdoped Bi2212 ($Bi_2Sr_2CaCu_2O_{8+\delta}$) samples under the application of a 5 T magnetic field. The effect of the applied magnetic field is to create vortices where superconductivity is destroyed and, thus, where a different, competing order could settle in. STM gives information about the local density of states (LDOS) with atomic resolution and makes it possible to reveal modulations of the density even characterised by incredibly short correlation lengths. Within the vortex cores, period-4 density modulations were observed (see Fig. 1.18). The Fourier transform analysis shows peaks at $(\pm 0.25, 0)$ and $(0, \pm 0.25)$ which are present only when the external magnetic field is applied. These peaks are related to the vortex-induced states. By a Lorentzian fitting, a correlation length of ~ 30 Å was estimated for the charge modulation. The bi-dimensional momentum structure of the charge order is depicted in panels (b) and (c). It is undeniable that the appearance of a periodic modulations only in the regions where superconductivity is suppressed supports the idea that charge order and superconductivity are competing phases.

Charge order was thus observed in La-based, Bi-based and Ca-based [46] compounds. Its

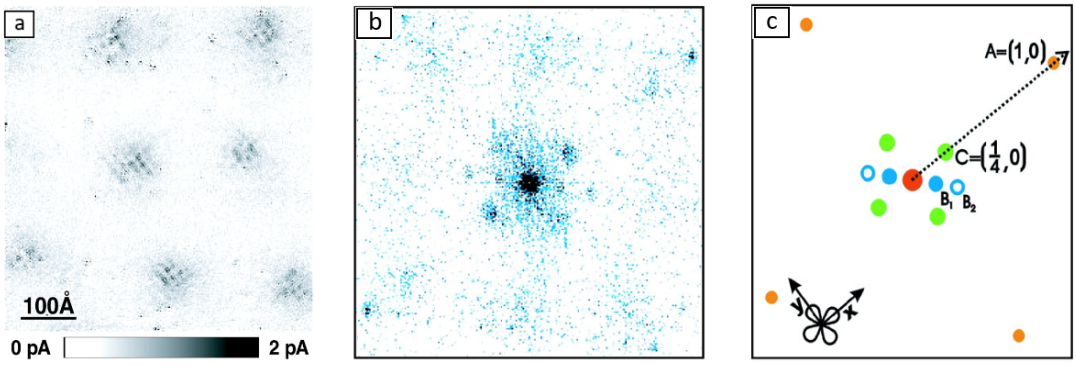

Figure 1.18: (a) STM measurements on Bi2212 under a 5 T magnetic field. The quantity represented is the differential tunnelling conductance dI/dV (integrated between 1 and 12 meV). The presence of magnetic vortices with dimension around 100 Å is evident. (b) and (c) report the bi-dimensional power spectrum of the map in (a). Distances are measured in reciprocal lattice units. Orange points at (±1,0) and (0,±1) correspond to peaks due to the Bi lattice. Blue peaks B_1 and B_2 indicates a supermodulation which is also present when the external magnetic field is removed. Green points appear only when a magnetic field is applied and correspond the vortex-induced states. Figures taken from Ref. [44].

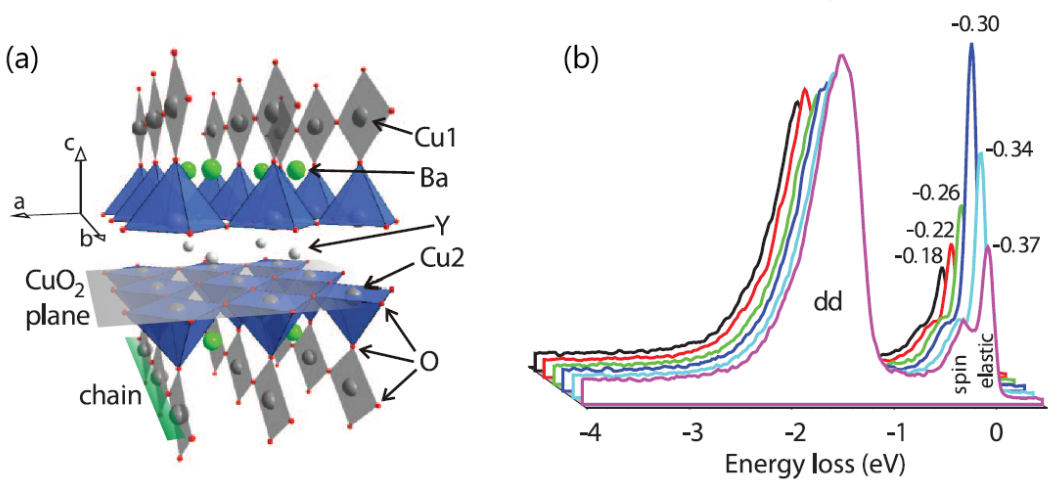

Figure 1.19: (a) Crystalline structure of $YBa_2Cu_3O_{6+x}$. Copper planes and chains are highlighted. For $x < 1$ some oxygens of the chains are missing. (b) RIXS spectra of underdoped $Nd_{1.2}Ba_{1.8}Cu_3O_7$ at $T = 15$ K ($T_C = 65$ K) collected at different values of the in-plane transferred momentum. Elastic, spin and interorbital (dd) spectral features are indicated. Figures taken from Ref. [45].

presence in the 123 cuprate family ($RBa_2Cu_3O_{6+x}$, where R indicates a rare earth) was not clear, even though several signs could suggest the existence of a charge modulation. Among these, the dip in the superconducting dome around $p = 1/8$ ($x = 0.67$) [47], as similarly observed in the 214 family. Nevertheless, discrepancies in the spin dynamics between the two families could be the hint of a different kind of charge order. Resonant inelastic x-ray scattering (RIXS) turned out to be the ideal technique to detect charge density waves in materials. Thanks to the use of resonant photons a reasonable scattering intensity is ensured and the energy-resolving capability of the spectrometer allows one to single out the charge order signal, free of other spurious scattering contributions at finite energy.. Ghiringhelli *et al.* [45] studied samples of $(Y,Nd)_{1+x}Ba_{2-x}Cu_3O_7$ by using RIXS. Their crystal structure can be seen in Fig. 1.19 (a). A characteristic of the 123 family compounds is the presence of copper both in the CuO_2 planes (Cu2) and inside CuO chains (Cu1). These chains are located between the copper planes and play the role of charge reservoirs. Cu1 and Cu2 lie in nonequivalent chemical environments and thus they are characterised by slightly different absorption edges: a simple energy absorption experiment can be employed to discern among Cu1 and Cu2. The authors collected RIXS data with a combined instrumental resolution of approx. 130 meV. This means that the quasielastic contribution, ascribable to CDWs, is disentangled from inelastic spectral features characterised by higher energy-loss. The quasielastic component, which from now on will be referred to simply as elastic, derives from many elastic scattering contributions, including thermal diffuse scattering and tails of nearby Bragg reflections but, most crucially, it can include zero- or low-energy fluctuations of the charge density related to valence electrons. Fig. 1.19 (b) shows RIXS spectra of underdoped $Nd_{1.2}Ba_{1.8}Cu_3O_7$. Each spectrum has been collected at a different H value, where H is the Miller index associated with a component of the in-plane transferred momentum $q_{\parallel} = (H, K)$ in a RIXS event. K has been kept fixed to zero value. In addition to the elastic component, also the magnetic (spin) and interorbital excitations (dd) are visible in the spectra. One can notice that the elastic component reaches a peak of intensity when $H = 0.31$ reciprocal lattice units (r l u). This feature is shared by all compounds of the 123 family. It must be underlined that this exceptional intensity peak is observed only when the incoming photon energy is set resonant to the Cu atoms in the planes, irrefutably proving that this spectral feature is to be ascribed to those ions in the CuO_2 planes. Furthermore, measurements performed in untwinned $YBa_2Cu_3O_{6.6}$ samples present intensity peaks scanning along both the in-plane directions, i.e., both parallel and perpendicularly to the copper chains. Even though an anisotropy was detected between the measurements along H and K [48], these peaks cannot be compatible with the 1D nature of the Cu chains. A fundamental result was obtained by performing measurements with different incident photons polarisation. This

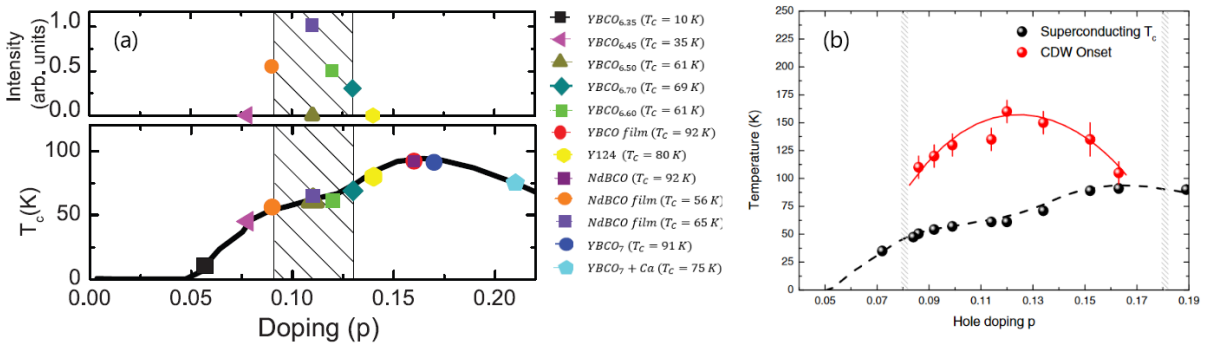

Figure 1.20: (a) Doping-dependence of the CDW signal at $T = 15\,\mathrm{K}$ in several cuprates. The range where CDWs are observed is shaded ($0.9 \leq p \leq 1.3$). (b) Doping dependence of the onset temperature of the CDW in $YBa_2Cu_3O_{6+x}$. The optimal doping is approx. $p = 0.12$. Figures taken from Refs. [45, 48].

has been done to understand if the quasi-elastic signal derives from the contribution of charge scattering or spin excitations. At the end, by comparing data and a theoretical model for spin-flip from Cu2 sites, the polarisation dependence of the quasielastic peak clearly relates it to charge modulation [45]. The authors also created a plot (panel (a) of Fig. 1.20) showing that the doping range where charge density waves are observed ($0.9 \leq p \leq 1.3$) is the same where the 123-family cuprates experience a drop in the superconducting transition temperature. The lowering of T_C is one more time connected to a competition between charge order and superconductivity phases. We point out that, concerning the sample Y124 ($YBa_2Cu_4O_8$), the authors did not observe any kind of CDWs and its doping level ($p = 0.14$) is placed outside the range where the quasielastic peak appears. The focus of this thesis is indeed aimed at investigating the presence of CDWs in Y124 crystals. One can find details about this compound in Section 1.3 and the results of the experimental investigation in Chapter 3. Through a temperature dependence of the quasi-elastic peak, the authors further investigated the mutual interaction between CDWs and SC phase. Fig. 1.21 (a) shows the energy integrated CDW signal at different temperatures in $YBa_2Cu_3O_{6.6}$. The peak is present both below and above critical temperature ($T_C = 60\,\mathrm{K}$). The peak first becomes narrower upon cooling from high temperature and then broadens again below T_C (look at the FWHM trend in panel (c)). This means that the correlation length is temperature dependent and that it would be more appropriate to talk about charge density fluctuations rather than static CDWs. The CDW intensity is the biggest at $T = T_C$. Its decrease for $T < T_C$ provides a direct proof of the "fight" between superconductivity and charge modulation. A final comment is that charge order in 123 cuprates shows features completely different from the stripe order in LSCO. In first place, the periodicity of the charge modulation is uncorrelated to the periodicity of

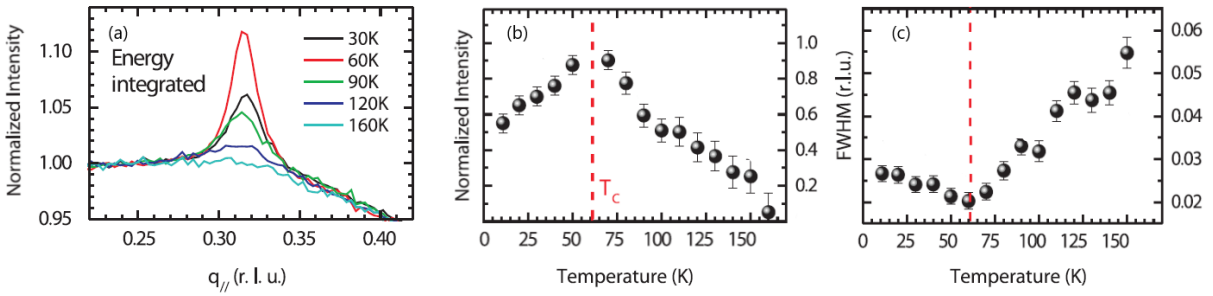

Figure 1.21: (a) Temperature dependence of the CDW signal in $YBa_2Cu_3O_{6.6}$. Temperature dependence of the quasielastic intensity (b) and full width at half maximum (c) derived from energy-integrated data. Figures adapted from Ref. [45].

the underlying lattice, giving rise to an incommensurate CDW. A second observation is that charge order does not come together with a spin modulation. The competition here is really just between SC and charge order. Blanco-Canosa *et al.* [48] confirmed all the previously presented result on YBCO and they further investigated its the doping dependent behaviour. In particular, they focused on the doping dependence of the CDW onset temperature T_{CDW}. We can identify T_{CDW} as the threshold temperature above which the quasielastic peak is not present anymore, indicating a disappearance of any charge modulation. The highest T_{CDW} is obtained for the optimal doping level $p = 0.12$. Fig. 1.20 (b) shows details about T_{CDW} dependence on hole doping.
A different experimental approach to investigate the CDW signal in $YBa_2Cu_3O_{6+\delta}$ was employed by Gerber *et al.* [49]. The authors performed x-ray scattering experiments by using free electron laser (FEL) radiation under the application of pulsed high magnetic fields. The high brilliance of the x-ray FEL ensures the detection of the CDW signal, even though it may be weak. It was possible to detect the scattering signal by using just a 50 fs single x-ray pulse together with the simultaneous application of a millisecond magnetic field pulse. By doing so, the application of high magnetic fields, beyond 17 T, is practicable. In previous discussions, we pointed out the competition between superconductivity and charge order. Since high magnetic fields destroy the SC phase, it is reasonable to expect a stronger CDW signal below T_C. Indeed, the authors observed that the only field-induced changes in the quasi-elastic signal appear when $T < T_C$: peaks measured at 20 T are stronger in intensity and sharper than the corresponding peaks at zero-field. One can verify this looking at the blue points in panel (A) of Fig. 1.22. Nevertheless, they noticed (look at 1.22 (A)) that the field-induced enhancement is bigger at $L \sim 1$ and not at $L \sim 1/2$, where the CDW signal is the highest in the absence of any magnetic field [45]. Measurements at $T = 10$ K under applied magnetic field revealed that up to 15 T the intensity of the quasi-elastic peaks at both $L \sim 1$ and $L \sim 1/2$ are comparable.

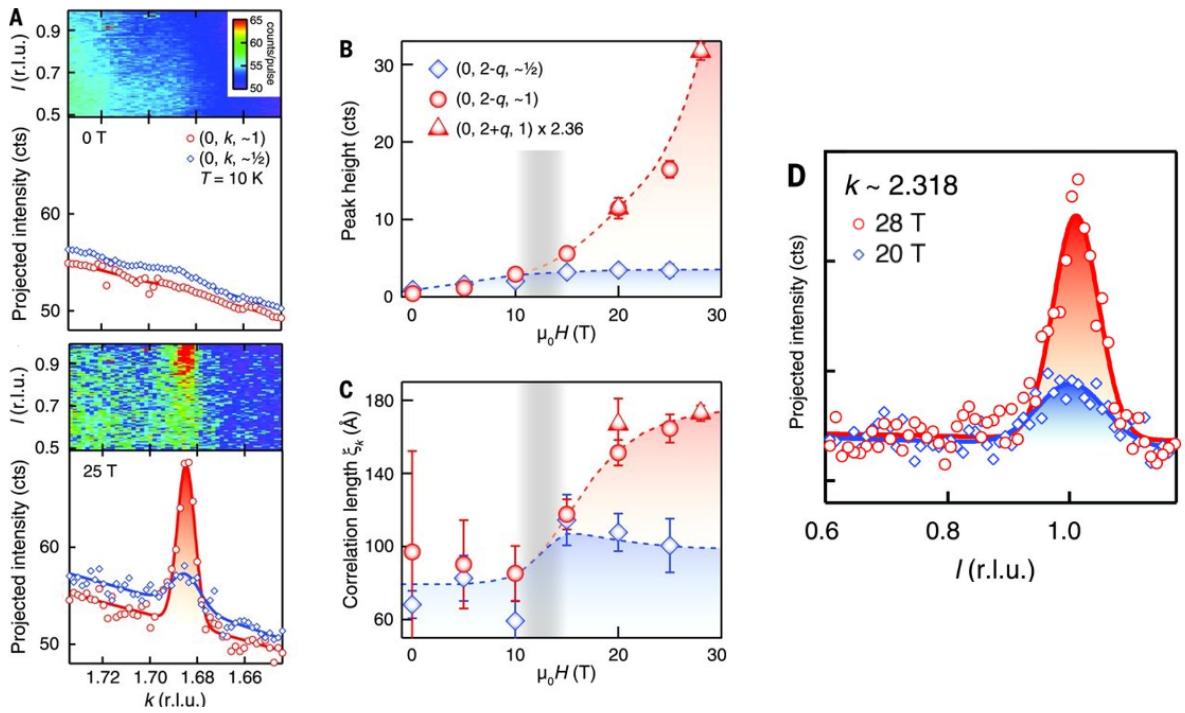

Figure 1.22: X-ray scattering measurements under applied magnetic field carried out on $YBa_2Cu_3O_{6.67}$ samples. (A) CDW diffraction patterns and projected CDW peak profiles near $L \sim 1$ and $L \sim 1/2$ at zero-field and $B = 25\,\mathrm{T}$: CDW signal arises only when superconductivity is suppressed by the high magnetic field. Field dependence of the peak height (B) and coherent length (C) of the projected CDW profile at $L \sim 1$ and $L \sim 1/2$. The diffenrent trend is evident for magnetic fields above 15 T. (D) L-dependence of the field-induced CDW signal. Figures taken from Ref. [49].

However, for higher magnetic field the former keeps on growing in intensity, whereas the latter saturates. The field dependence of the peak intensity is shown in panel (B). The different field dependence related to CDW intensity but also to the correlation length (panel (C)) is an evidence that the two CDW order at $L \sim 1$ and $L \sim 1/2$ are distinct, even thought they both exist at the same time. Furthermore, the onset of the field-induced order for fields greater than 15 T is in agreement with nuclear magnetic resonance (NMR) measurements [50]. The fact that the field-induced peak becomes sharper, not only in the K-direction but also along the L-direction (panel (D)), indicates the 3D-nature of this field-induced CDW. Checking again the phase diagram of Fig. 1.9, one can realise that the 3D-CDW exists in a region inside the supercondcuting dome. At zero-temperature it terminates at the doping levels $p_{c1} \sim 0.08$ and $p_{c2} \sim 0.16$. These two points, which mark phase transitions at $T = 0\,\mathrm{K}$, are identified as quantum critical points. So far, as far as CDWs are concerned, we dealt with short/medium range incommensurate CDWs existing in the pseudogap phase and weakly competing with superconductivity. Moreover, below

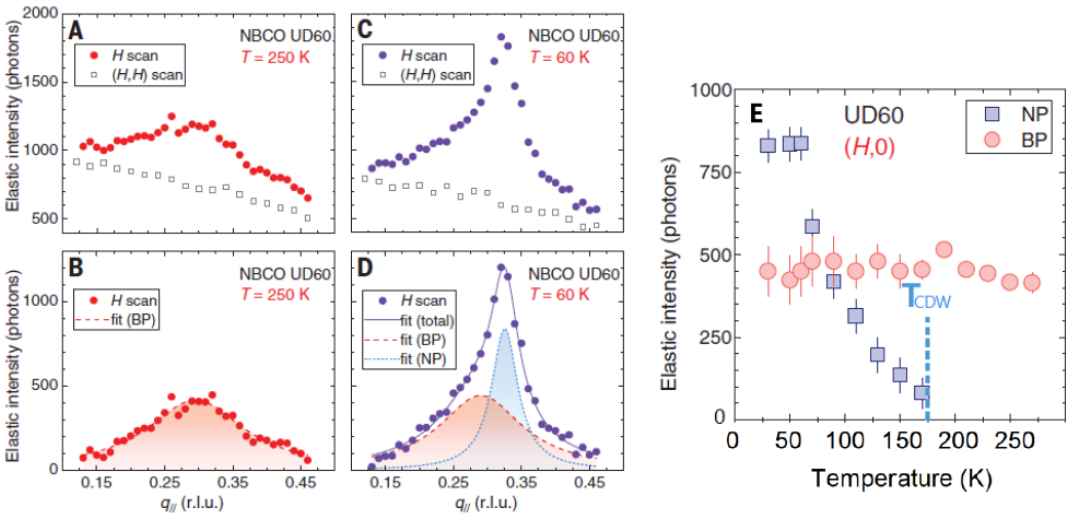

Figure 1.23: (A) and (C) report the data collected on NBCO samples at $T = 250\,\mathrm{K}$ and $T = 60\,\mathrm{K}$, respectively. The linear background has been retrieved from measurements along the (H,H)-direction. (B) and (D) are the data after background subtraction. The high-temperature peak is fitted by a single broad Lorentzian peak, whereas the low-T peak is fitted by a broad and a narrow Lorentzian profiles. They are centred at $q_{BP} = (0.295, 0)$ and $q_{NP} = (0325, 0)$, respectively. (E) shows the temperature dependence of the intensity for the BP and NP. The NP intensity vanishes above the CDW critical temperature T_{CDW}. Figures taken from Ref. [51].

T_C and under applied strong magnetic fields, long-range 3D-CDW can arise for a certain doping range. However, by RIXS measurements on (Y,Nd)$Ba_2Cu_3O_{6+\delta}$ samples, Arpaia *et al.* [51] found out that short-range charge density fluctuations exist in a wide region of the phase diagram. Thin films characterised by several doping levels were employed so as to investigate the phase diagram from the AFM region to the weakly overdoped region. This way the pseudogap temperature T^* has also been crossed. The authors collected data along the $(H,0)$ direction at several temperatures. Then, they decomposed the quasielastic peak at high temperatures as the sum of a single Lorentzian curve and a linear background. Instead, at lower temperatures a second Lorentzian peak is necessary to fit the data. Whereas the former peak is similar to the broad peak found for the high-T data, the latter peak is narrower and centred at a nearby H value. The subtraction of the linear background and the decomposition with the Lorentzian peaks is reported in Fig. 1.23. By analysing the behaviour of the narrow peak (NP) and broad peak (BP), they realised that the NP shows all the features typical of the incommensurate CDWs observed in several underdoped cuprates. Its temperature dependence (panel (E)) shows the presence of a critical temperature T_{QC}, the one we have called T_{CDW} so far, which indicates the onset of CDWs. Instead, the BP presents an almost constant temperature dependence and this is why the authors thought of relating it to short-range charge density fluctua-

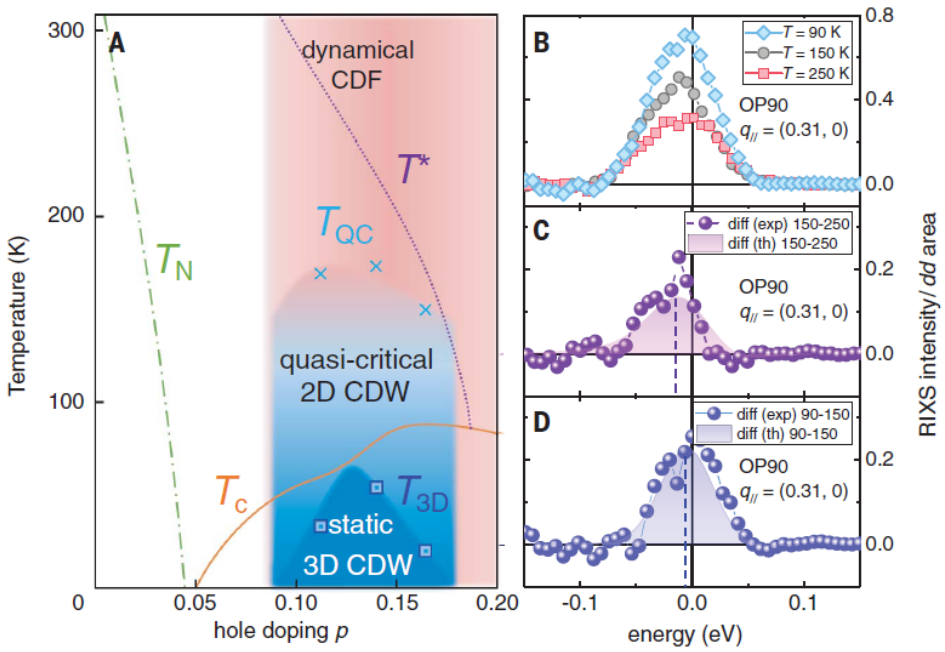

Figure 1.24: (A) Hole- doped cuprate phase diagram where all the possible forms of charge order are indicated. Here T_{QC} stands for what we have called T_{CDW}. Dynamical CDFs occupy a great portion of the phase diagram and coexist with quasi-critical and 3D CDWs. (B) Quasielastic peak measured by RIXS on NBCO samples at different temperatures. (C) and (D) are the 150 K − 250 K and 90 K − 150 K difference spectra, respectively. They highlight the dynamical nature of CDFs and quasi-critical behaviour of CDW. Figures taken from Ref. [51].

tions (CDFs). A further comment is that the total intensity of the peaks, evaluated as the underlying area, is dominated by the BP component, even though the NP reaches higher amplitude values at low temperatures. To investigate the possible dynamical character of the CDFs, high-resolution RIXS spectra (40 meV) were collected at the wave vector of the BP maximum. The quasielastic peak is the result of several contributions, but the only component which presents a marked temperature dependence are the CDWs, whose intensity increases upon cooling. Thus, to better focus on the CDW contribution, the high-T spectra were subtracted from the low-T spectra (see panels (C) and (D) of Fig. 1.24). The 150 K − 250 K difference gives rise to a peak centered around 15 meV which indicates the dynamic fluctuating nature of the charge density fluctuations (CDFs) related to the BP. The 90 K − 150 K difference spectrum is centred around zero energy indicating that the NP, which appears at lower T, is connected to a nearly-static, quasi-critical CDW. A huge difference is that quasi-critical CDWs are in competition with superconductivity, as highlighted by the temperature dependence of their correlation length and intensity, instead, the weak temperature dependence of the CDFs confirms that they do not com-

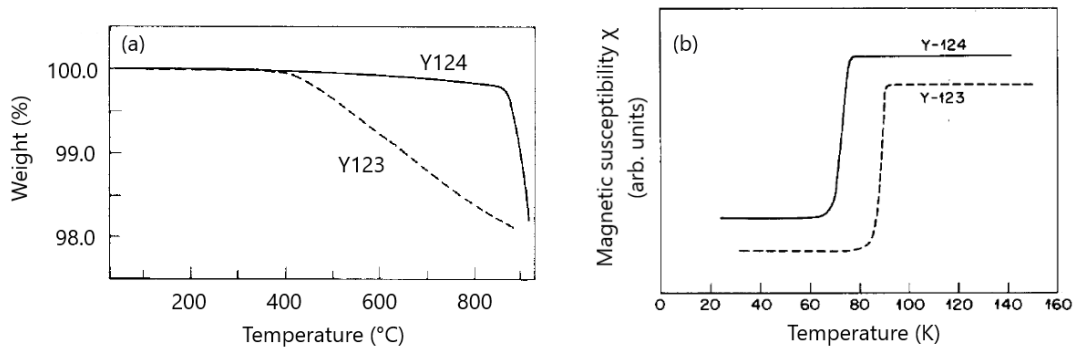

Figure 1.25: (a) Thermogravimetric curve for the 124 sample and comparison with the 123 sample. The oxygen loss for the 123 sample is already clear above 400 °C. (b) Magnetic susceptibility vs. temperature for Y124 and Y123 samples. The drop in resistivity indicates the transition to the SC regime. Figures taken from Ref. [52].

pete with superconductivity and that they occupy a wide area of the phase diagram. An illustration of the phase diagram in light of what we have exposed so far is given in Fig. 1.24 (A). The authors finally suggested that the existence of CDFs provides an effective low-energy scattering mechanism which could explain the linear trend of resistivity versus temperature present in normal and strange metal phases of cuprates.

1.3. $YBa_2Cu_4O_8$

In this Section a summary of the properties and studies concerning the superconducting cuprate $YBa_2Cu_4O_8$ (Y124) will be provided. Indeed, this thesis work is aimed at the investigation of the presence of charge density waves in this compound.

1.3.1. Synthesis, structure and electronic properties

$YBa_2Cu_4O_8$ (Y124) is the only cuprate which possesses a stable stoichiometry at all temperatures with a highly robust oxygen content. Thus, it represents a unique, defect-free system to retrieve information within the underdoped region of the phase diagram without further complications given by variable oxygen stoichiometry.
A simple synthesis method was proposed for Y124 production [52], where a stoichiometric powder of $YBa_2Cu_3O_7$ ($T_C = 90\,K$) is used as a precursor. First, the 123 powder is mixed with a suitable amount of CuO. Later on, the mixture is dried, ground and subject to a pressure of 680 atm while temperature is kept around 800 °C. The mixture is exposed to a constant flux of oxygen.The sintered samples undergo several analysis in order to confirm their quality. X-ray powder diffraction confirmed that the samples are mainly made of

the 124 phase. Moreover, the desirable property of stability in the oxygen content is clearly visible in Fig. 1.25 (a). Y124 decomposes only above 850 °C, whereas the oxygen loss for the 123 sample is evident starting from 400 °C. Panel (b) of the same figure reports the temperature dependence of the AC magnetic susceptibility from which the Y124 superconducting critical temperature can be extracted. It results to be around 73 K which is consistent with the 80 K retrieved from resistivity measurements (midpoint of the resistivity drop) [52].

The thermal stability of Y124 extends to its structural phase as well. No evidence of phase transitions have been observed, differently from $YBa_2Cu_3O_7$ which experiences an orthorhombic-to-tetragonal phase transition at high temperatures [53]. The crystalline structure of Y124 was obtained through experiments based on neutrons [54]. We are dealing with a base-centered-orthorombic structure characterised by the following lattice constants:

$$a = 3.8402\,\text{Å}, \qquad b = 3.8708\,\text{Å}, \qquad c = 27.2309\,\text{Å}. \tag{1.1}$$

A schematic illustration of the Y124 crystalline structure is depicted in Fig. 1.26. One major structural difference from Y123 is the presence of double chains of Cu(1)-O(1) between the BaO-planes. The vertical distance between two nearby chains is 1.8740 Å, very similar to the Cu(1)-O(4) distance of 1.8337 Å. By contrast Y123 is a single-chain system. As a consequence, in Y124 each O(1) atom is chemically bound to three Cu(1) atoms, differently from Y123 where each O(1) has only two near-neighbours. The three-fold coordination could be responsible for the higher stability in the oxygen content.

The Y124 electronic band-structure was theoretically studied by Yu *et al.* [53] and compared to the Y123 compound. A substantial similarity lies in the strong bi-dimensionality of the electronic properties: moving in the reciprocal space in the z-direction (from Γ to Z) states are almost flat in energy ($\Delta E \approx 0.05\,\text{eV}$). Both Y124 and Y123 have two 2D dp-σ bands crossing the Fermi level coming from the CuO_2 planes and their orbital character

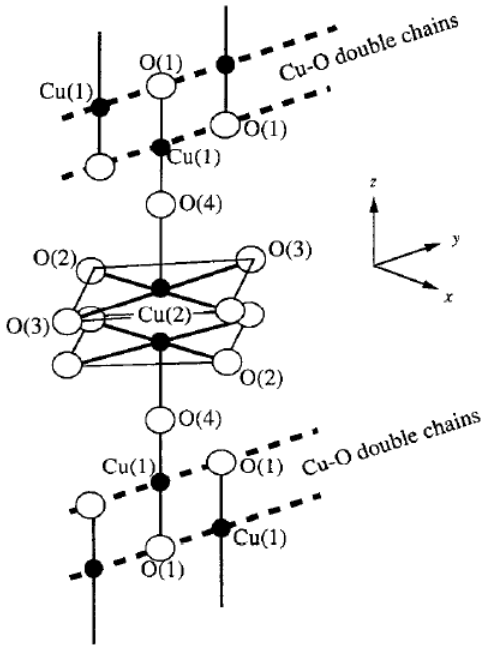

Figure 1.26: Illustration of the Y124 crystalline structure. Y and Ba atoms are not shown. Y atoms are placed between the two Cu(2) planes, whereas Ba atoms lie on the Cu(2) and Cu(1) planes. Figure taken from Ref. [53].

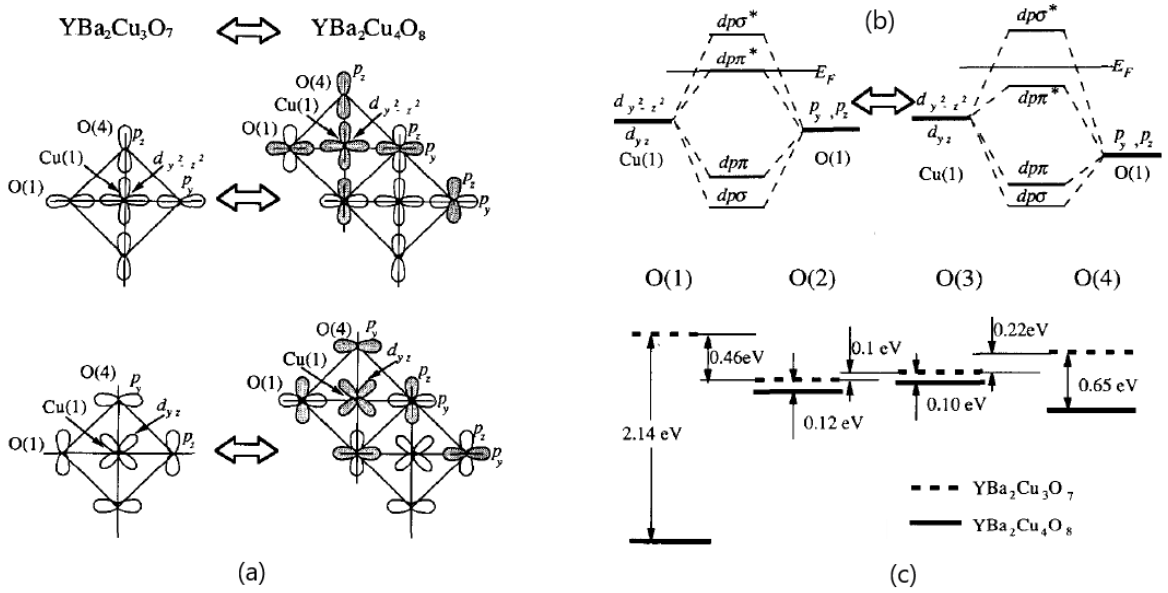

Figure 1.27: Comparison between Y123 and Y124: representation of the bonding and antibonding configurations (a) and energy position of the hybrid electronic levels (b). Comparison of O 1s energy levels as predicted by Madelung potentials in Y124 and Y123 (c). Figures taken from Ref. [53].

is very similar in the two compounds. Concerning the copper chains, two 1D dp-σ bands which crosses the E_F are present in Y124 band-structure, whereas the single-chain in Y123 is responsible for a single 1D dp-σ band. Moreover, the bands given by the chains show discrepancies in the two compounds. The reason must be searched in the difference of coordination for the copper atoms inside the chains: the way in which oxygen 2p-orbitals and copper 3d-orbitals overlap differs in the two cases. The representation in Fig. 1.27 (a) can be useful to understand the orbital hybridisation. In Y123 compound the presence of the 1D $dp\pi^*$ antibonding band at the Fermi energy explains why the density of states (DOS) structure near E_F is non-equivalent in the two cases. The same band in Y124 finds itself at energy lower than the Fermi level justifying why the total DOS of Y124 at E_F, $N(E_F)$, is almost half of the Y123 $N(E_F)$. Since $N(E_F)$ in Y124 is not influenced by the Cu(1)-O(1)-O(4) $dp\pi$ states, its value is independent of the Fermi energy position, i.e., of the oxygen content.

A further explanation of Y124 stability in the oxygen stoichiometry is provided by analysing the electronic structure in the Madelung potentials framework [53]. Madelung potentials are different in Y124 and Y123 one more time because of the coordination of oxygens inside the chains. It was noted that the direct consequence is a higher electronic stability of oxygens O(1) and O(4) in Y124 with respect to the same oxygens in Y123. This is clarified in Fig. 1.27 (c) where the energy position of oxygens 1s core states are

given for both compounds.

1.3.2. Quantum oscillations in underdoped cuprates

Several experimental techniques exist which can be employed to map the Fermi surface of a metal under the application of a strong magnetic field. Their working principle is based on the fact that electrons, when subject to a magnetic field, occupy a series of quantised levels. These states go under the name of Landau levels and are a direct consequence of considering the vector potential $\mathbf{A}$ inside the Hamiltonian [55] of the system. The energy separation between these levels results to be proportional to the strength of the magnetic field. During an experiment, by varying the external magnetic field, it happens that the energy of the Landau levels coincides with the Fermi energy. At that point, the electronic density of states at E_F undergoes oscillations which also reflect in many other physical properties, such as the Hall resistance and the magnetic susceptibility. That is why the term "quantum oscillations" (QOs) is used to indicate this variety of techniques. Furthermore, the presence of such oscillations can be regarded as evidence that the material under study behaves as a Fermi liquid. Just to have it as a reference, the energy of the quantised levels produced by the application a magnetic field B on a free fermions system is given by

$$E = \frac{qB}{m^*}\left(l + \frac{1}{2}\right) \tag{1.2}$$

where q and m^* are the fermion charge and effective mass, respectively, and l is an integer. Actually Eq. 1.2 reports only the B-dependent part of the energy. A period of $1/B$ is expected for oscillations arising from Landau levels.

Experimental observations of quantum oscillations in underdoped $YBa_2Cu_3O_{6.5}$ ($p = 0.1$) demonstrate that it possesses charged quasiparticles and the existence of a Fermi surface. Nevertheless, data do not show distinct oscillations versus $1/B$ [56]. The low frequency of quantum oscillations reported for $YBa_2Cu_3O_{6.5}$ could be explained in terms of a reconstruction of the Fermi surface, in particular by the presence of small Fermi surface pocket associated with the low oscillation frequency [57]. This reconstruction may be induced by a variety of symmetry-broken states which populates the phase diagram in the underdoped region. A biaxial CDW reconstruction was proposed by Chan *et al.* [58] and it is shown in Fig. 1.28 (a). One can observe a diamond-shape electron pocket (red) at nodal position and two smaller hole pockets (blue). These further structures could account for the multi-frequency behaviour observed in the Y123 QOs.

Yelland *et al.* [60] reported the observation of QOs also in the Y124 compound. Mea-

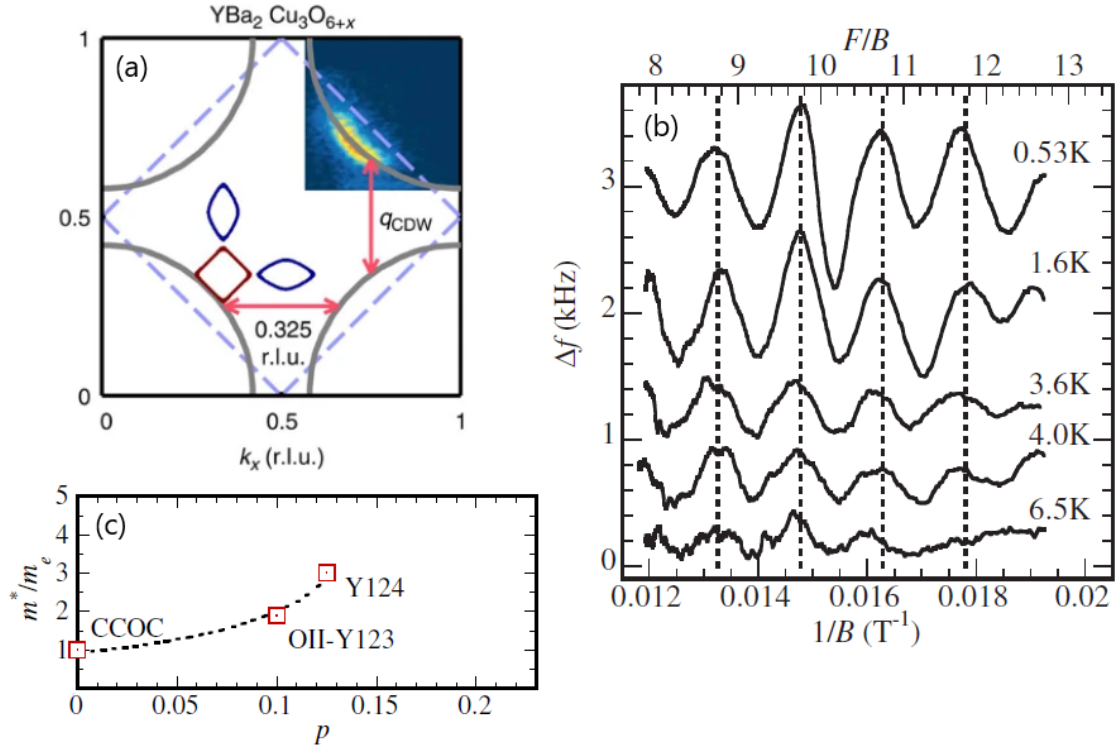

Figure 1.28: (a) Unreconstructed (grey lines) and reconstructed (color lines) Fermi surface of $YBa_2Cu_3O_{6+x}$. For the reconstruction it was assumed a biaxial CDW wavevector (Q_{CDW},0) and (0,Q_{CDW}) with $Q_{CDW} = 0.325$ r l u [48]. (b) Changes in resonant frequency Δf in a TDO experiment as a function of $1/B$. Data have been collected at various temperature under applied magnetic pulses of 85 T and the background has been subtracted. The periodicity of the signal is $F = 660 \pm 15$ T. (c) Values of the quasiparticle mass for Y124, Y123 [57] and $Ca_2CuO_2Cl_2$ (CCOC) [59]. A trend for the doping dependence is traced (dashed line). Figure (a) taken from Ref. [58] and figures (b) and (c) taken from Ref. [60].

surements were performed by using a tunnel-diode oscillator (TDO) technique under the application of a pulsed magnetic field up to 85 T. After the subtraction of a smooth monotonic background, the behaviour of the TDO frequency Δf as a function of $1/B$ is plotted in Fig. 1.28 (b). As expected, the oscillations have $1/B$ periodicity. The presence of a peak at $F = 660 \pm 15$ T in the fast Fourier transform confirms the presence of Fermi surface pockets. Furthermore, by comparison with heat capacity data, the authors concluded the Fermi surface of Y124 presents four hole pockets near the nodal points, as similarly proposed in the original model for $YBa_2Cu_3O_{6.5}$ [57]. The observation of Fermi surface pockets also in Y124 can be a signal of their ubiquity in underdoped cuprates. A difference lies in the quasiparticle mass whose value in Y124 is $m^* = 3.0 \pm 0.3\, m_e$,

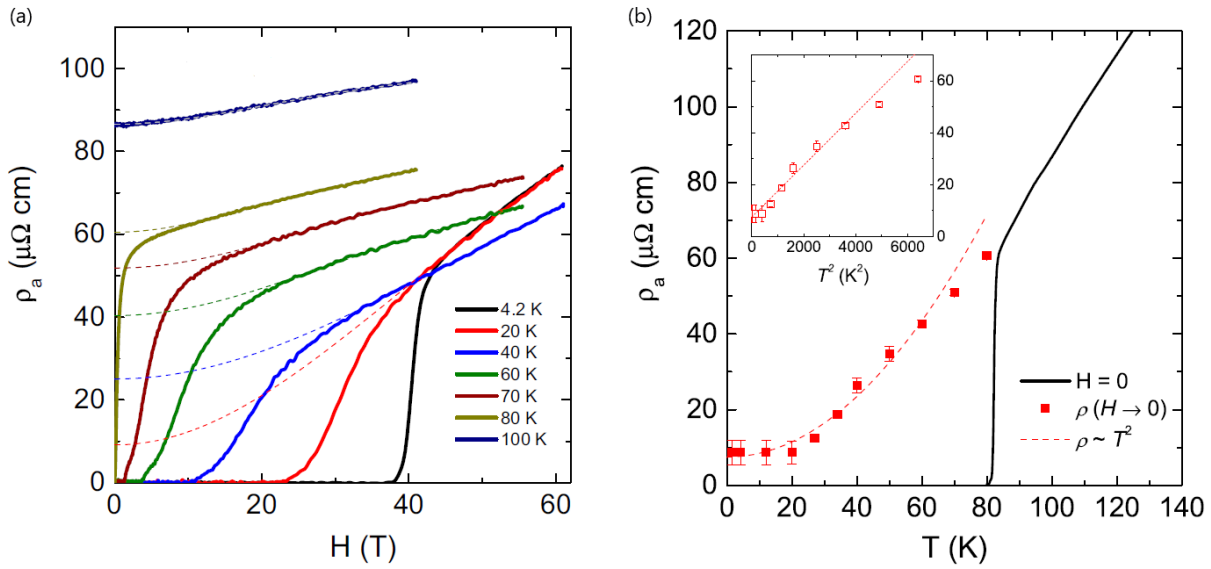

Figure 1.29: (a) In-plane resistivity versus magnetic field in Y124 sample. Current was set along a-axis and magnetic filed has been applied parallel to the c-axis. The dashed-lines are the result of a two-carrier model fitting on high-field data points. (b) Extrapolated normal-state data at $H = 0$. The dashed-line is a fitting based on the typical quadratic behaviour of Fermi-liquid at low temperatures. The inset reports the dependence against T^2, whose linear trend underlines the parabolic behaviour of $\rho_a(T)$. Figures taken from Ref. [61].

considerably larger than in Y123. Fig. 1.28 (c) suggests a possible doping dependence of the effective mass by combining the available results.

Many signs, such as quantum oscillations [57] and optical conductivity [62], seem to confirm the Fermi-liquid behaviour exhibited by underdoped cuprates at low temperatures. Moreover, Proust *et al.* [61] provided evidences showing that electrical resistivity in $YBa_2Cu_4O_8$ goes as the square of T, at low temperatures. This is one more time typical of the Fermi liquid regime. The plot in Fig. 1.29 (a) reports in-plane magnetoresistance data in Y124 under applied magnetic fields up to 60 T and for several temperatures, the majority of which below $T_C = 80\,\mathrm{K}$. The upper critical field has been derived from thermal conductivity data and has a value around 45 T [63]. A two-carrier model [64] was employed to fit the data outside the SC phase and it has been extended to extrapolate the value $\rho(0) = \rho(H \to 0, T)$ at each temperature. The extrapolated $\rho(0)$ values have been plotted as a function T and they have been fitted using a function of the form $\rho_0(T) = \rho_0 + AT^2$. It follows pretty well the data points as shown in Fig. 1.29 (b). This trend is a further confirmation that we are dealing with Landau quasiparticles. In addition, the authors underlined that the value $A = 10.0 \pm 1 \mathrm{n\Omega \cdot cm \cdot K^{-2}}$ retrieved from the

data fitting is close to the same parameter measured in Y123 ($p = 0.11$) above $T = 50\,\mathrm{K}$ [65]. Taking again the biaxial CDW reconstruction as hypothetical cause, the presence of an electron pocket, coming from the residual DOS in the nodal region, seems to be well-established. Nevertheless, the extracted value for the A parameter is not compatible with the presence of just the electron pocket, but suggests the existence of at least an additional hole pocket. This agrees with the previously proposed reconstruction by Chan *et al.* [58]. A final comment concerns the long-range static charge order which is known to arise in underdoped cuprates below a certain temperature and in presence of applied magnetic fields. Since no abrupt changes appear in the $\rho(0)$ behaviour, we can state that no Fermi surface reconstruction is happening in this phase transition.

To conclude, both the observation of quantum oscillations in Y124 and its doping level similar to the one of cuprates where charge order was observed are clues suggesting the existence of CDWs in Y124. In particular, $YBa_2Cu_3O_{6.5}$ and Y124 display similar quantum oscillation frequencies, indicating that under high magnetic fields a similar Fermi surface reconstruction occurs in both compounds, which was suggested to involve CDW formation. The missed observation of CDWs in the first work on this compound by Ghiringhelli *et al.* [45] may be due to several reasons, such as a weak signal, a non-optimised alignment (samples are characterised by a very small size) or other experimental details. All these thoughts lay the foundations for this thesis work.

2 | Resonant inelastic x-ray scattering and experimental setup

In this Chapter resonant inelastic x-ray scattering (RIXS) will be introduced. It is a photon-in photon-out spectroscopy which allows to study several intrinsic excitations of the material under study. In this thesis we will confine ourselves to the soft RIXS, where the energy of the incoming radiation is limited to $\approx 2\,\mathrm{KeV}$ (soft x-rays range), in which the $3d$ metals L edges lie. This makes this techniques particularly suitable for the characterisation of transition metal oxides, such as high-T_C cuprate superconductors. After discussing the main features of RIXS, i.e, the physical process and all kinds of excitation that can be probed, a brief description of the experimental setup of the ID32 beamline at the European Synchrotron Radiotion Facility (ESRF), where the experiments were carried out, will be provided.

2.1. Resonant inelastic x-ray scattering

RIXS is a powerful spectroscopic technique where x-rays interact with matter. An incident photon interacts with the sample and undergoes the scattering process, possibly losing energy and changing momentum or polarisation. Elementary excitations are thus created inside the material under study and measuring variations in the physical properties of the scattered photon allows to retrieve information about those excitations. This technique is called "resonant" because the energy of the incident photon is not randomly chosen, but is selected such that it corresponds to a specific atomic x-ray transition of the system, in our case the L edge. This way the scattering cross section of the process is strongly enhanced. In order to match the photon energy to a particular edge a tunable x-ray photon source is essential. This can be achieved with synchrotron radiation sources.
Throughout this Section, a general description of RIXS will be provided along with a quick theoretical treatment of its cross-section. Refs. [66, 67] will be mainly followed.

2.1.1. Features and comparison with other techniques

RIXS is the perfect choice for our experimental purposes thanks to its very favorable characteristics. We summarise them in the following points.

1. RIXS is element specific. X-rays are tuned to the edge of a particular atomic ion inside the material under study. Furthermore, if two atoms of the same element find themselves in nonequivalent lattice sites RIXS is able to distinguish them. This is due to the fact that usually there is a little variation in the absorption edges which makes the two atoms distinguishable. We refer to this feature as chemical sensitivity.

2. RIXS is bulk sensitive. Even if the penetration depth of x-rays depends on the material and on the scattering geometry, as far as the soft x-ray regime (around 1 keV) is concerned the typical penetration depth is on the order of 0.1 μm. Whereas, for 10 keV x-rays in the hard x-ray region the penetration depth is on the order of few microns [66].

3. RIXS requires just small sample volumes. Compared with other techniques, for example inelastic neutron scattering, the scattering cross section of the photon-matter interaction is considerably higher. For instance, inelastic neutron scattering requires milligrams of materials while RIXS can measure thin film samples.

4. RIXS can exploit the polarisation of the photon. This can be an useful tool to distinguish different excitations in the material. Indeed, in each possible physical event which can take place, the conservation rules have to be respected. This translates into a rotation of the polarisation of the (linearly) polarised incoming x-rays if the excited quasi-particle carries angular momentum (for example a spin-flip excitation).

5. RIXS preserves the charge neutrality of the sample. Since no variation in the electrical charge takes place during the scattering process, no problems related to charging can arise, even though the sample is insulating.

6. RIXS is a fast process. Absorption and emission happen within few fs. The direct consequence is that RIXS is capable of probing even small energy excitations, such as fluctuating charge order, as the signal is not averaged out.

7. In the case of cuprates and of the Cu L_3 edge, RIXS allows for the investigation of a significant portion of the reciprocal lattice space. If we consider a photon of energy E, the corresponding momentum is $k = E/c\hbar$. Indeed, by using $E = 931$ eV (Cu L_3 edge) and evaluating the momentum in reciprocal lattice units (the in-plane lattice

parameter for cuprates is approx. 3 Å–4 Å [68]) we get $\approx 0.25\,\mathrm{r\,l\,u}$.

Therefore, RIXS can probe a wide class of intrinsic excitations of the system under study. It is possible to observe the electron-hole continuum and excitons in band metals and semiconductors, charge transfer and *dd* (intraband) excitations in strongly correlated materials and lattice excitations. Moreover, magnetic excitations are also symmetry allowed in RIXS since the impinging photon carries angular momentum and this can be transferred to the electron spin angular momentum in the scattering process. The elementary excitations of a material are at the base of important physical properties, such as transport properties. That is why we are so interested in the excitations of the systems, because they let us understand the system itself.
As this description should have clarified, RIXS can be a versatile, powerful and complex tool, all at the same time. It is necessary to deal with feature-rich spectra since all these excitations are present together.

2.1.2. The RIXS process

RIXS is a photon-in photon-out technique. An illustration of the process from the initial state to the final one is dispayed in Fig. 2.1. As a starting point, we can consider a photon characterised by a certain energy value E (chosen such that it resonates with an atomic transition) and momentum $\mathbf{k}$. Inside the material, the atoms of the targeted chemical species are in their ground state. When the photon impinges on the system, it interacts with an atom and causes the transition of a core electron up to the valence band. The atom finds itself in an excited state we can refer to as the intermediate state, whose lifetime is typically very short, approx. 1 fs–2 fs. This is clearly an unstable condition. In order to reduce the overall energy of the ion, an electron from the valence band decays filling the core hole back. This can come with a radiative decay, where a photon is emitted with energy E', given by the difference in energy between the starting valence level and the final core level, and momentum $\mathbf{k}'$. It is important to underline that, as a whole, this is a two-step process with a very short-living intermediate state. If the energy of the impinging photon coincides with the energy of the emitted photon, i.e. $E = E'$, then an elastic scattering event has occurred. Instead, if the difference $\Delta E = E - E'$ is non-zero, this means that some sort of excitation has been created in the system. Many different kinds of excitations can be produced as listed in Section 2.1.3. Thanks to the conservation laws we can say that the excitation created in the system is characterised by energy ΔE and momentum $\mathbf{q}$ given by

$$\begin{aligned} \Delta E &= E - E' \\ \hbar\mathbf{q} &= \hbar\mathbf{k} - \hbar\mathbf{k}' \end{aligned} \tag{2.1}$$

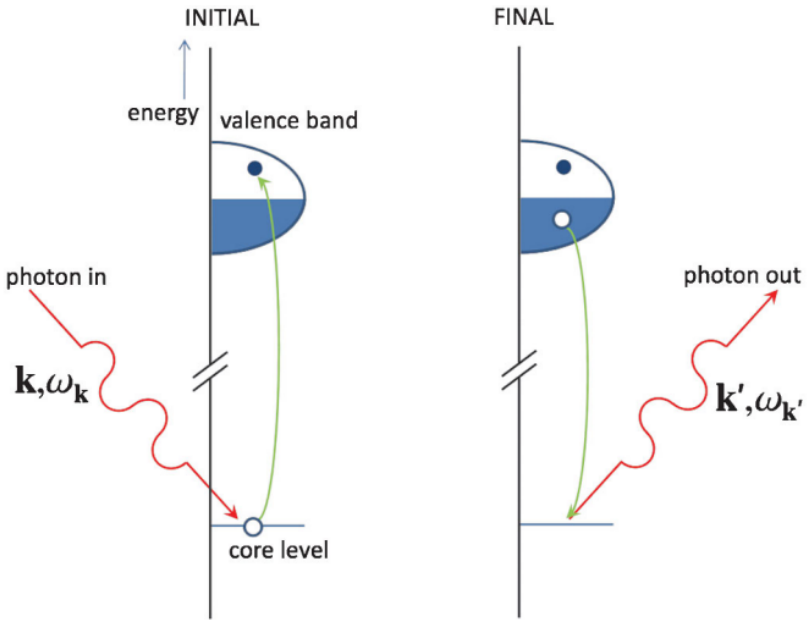

Figure 2.1: Phases of the RIXS process. The incoming photon promotes a core-level electron up to the valence band. A core hole is thus created. A few fs later, a valence band electron decays in order to fill the hole. This process results in the emission of a photon whose energy and momentum may differ from the ones of the original photon. Figure taken from Ref. [66].

It should be noted that the fluorescent decay, which is the one relevant for RIXS, is not the only possible de-excitation mechanism. A possible non-radiative decay channel is represented by an Auger process where the excess energy is used to eject a deep electron from the atom.

Focusing on copper-oxide materials, we can choose the incoming photon energy so that it resonates with the copper K, L, or M absorption edges. The electron configuration of copper of interest in these compounds is Cu^{2+} ($[Ar]3d^9$). The transition in the soft x-ray regime is the $L_{2,3}$ ($2p \rightarrow 3d$) one, at energies around 930 eV. This transition is electric dipole allowed. Whereas the Cu K edge is in the hard x-ray regime, and therefore at too high energies, it is possible to select the oxygen K edge as well, deciding to excite an $1s$ electron to an empty $2p$ valence state ($\sim$ 500 eV). This would allow to look into things from the "point of view" of the oxygen ions. However, we will not deal with this type of experiment in this work. The Cu L absorption edge, as well as the Cu M edge ($3p \rightarrow 3d$), allows to study dd excitations and orbital effects. Moreover, electrons in $2p$ (and $3p$) orbitals are subject to a strong spin-orbit interaction. Once a $2p$ electron is promoted to the d band, the spin is not a good quantum number anymore and spin mixing occurs. Thanks to this phenomenon, magnons can be excited in the system. An illustration of

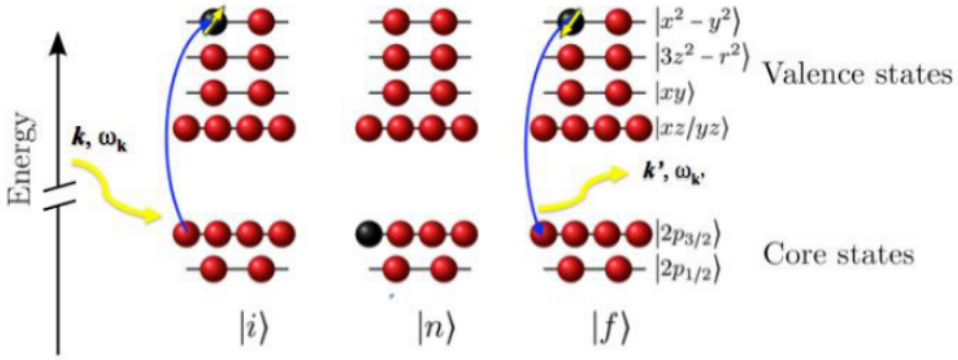

Figure 2.2: Excitation of a magnon in a RIXS process. The incoming photon promotes an electron which fills the single empty $3d$ level. A core hole is thus created, leaving the system in an unstable intermediate state $|n\rangle$. The spin quantum number is not a good quantum number anymore for $3d$ states. Therefore, when the same electron decays in order to fill the core hole it can leave in the $3d$ state an opposite spin with respect to the original one. The net result is the creation of a magnon. Figure taken from Ref. [69].

the mechanism bringing to the excitation of a magnon (spin-flip excitations) is depicted in Fig.2.2. Braicovich *et al*. [70] demonstrated that x-rays are an alternative to neutrons in probing magnetic excitations. In Fig.2.3 the dispersion of the single magnon measured in underdoped La_2CuO_4 both by RIXS and INS are shown. The two data sets are in excellent agreement with each other, confirming the equivalence of the two techniques in measuring magnetic excitations. The momentum dependence can be easily tracked in a RIXS experiement by changing the scattering geometry and, thus, the transferred momentum. Bimagnons, i.e. multiple magnons excitations, can be probed as well [71].

2.1.3. Intrinsic excitations

In this Section, all the possible elementary excitations which can be studied by using RIXS will be described. As Fig. 2.4 shows, the energy range of elementary excitations goes from plasmons and charge-transfer (CT) excitations at a few eV down to lattice vibrations (phonons) at the meV scale. Theoretically, RIXS should allow to measure the momentum dependence of all these spectrum features, thanks to the fact photons do not carry just energy but also momentum. This would not be possible with optical photons, characterised by energy on the order of few eV and thus carrying a negligible momentum with respect to the quasi-momentum of the elementary excitations of a solid. That is why, in order to probe the dispersion of elementary excitations in a reasonable part of a typical Brillouin zone, x-rays are necessary. Hereafter, we will discuss the different elementary

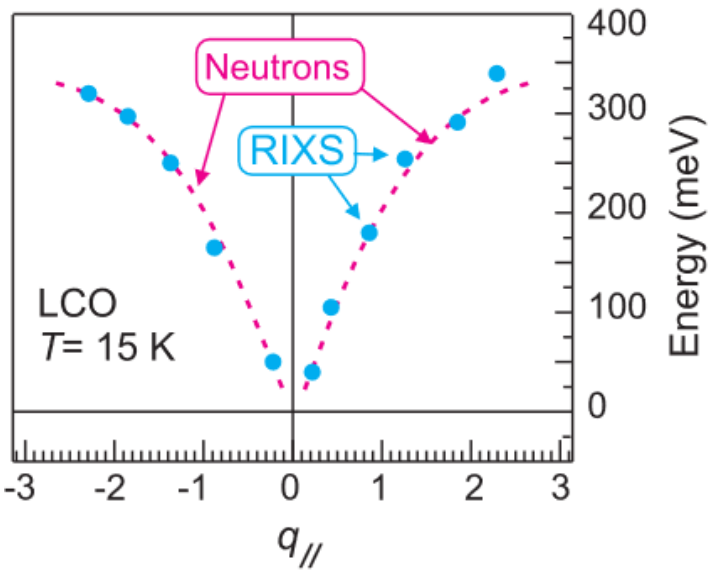

Figure 2.3: Comparison between the single magnon momentum dependence probed by INS and RIXS in a underdoped La_2CuO_4 sample. Figure taken from Ref. [70].

excitations accessible to RIXS.

a. Interband excitations and plasmons When considering a wide-band insulator, such as silicon or diamond, after a RIXS process an electron from the valence band can be promoted to the conduction band. The final result is that an excitation has been created in the form of an electron-hole pair across the gap. Differently, in a metallic material collective oscillations of the free electron gas density can be excited. They go under the name of plasma oscillations and the corresponding quasi-particles are called plasmons.

b. Charge-transfer excitations They consist of the motion of electrons from one lattice site to another. Let us consider a transition-metal oxide material. If the hole is created on the metal site some electric charge moves from a nearby ligand site closer to the metal ion in order to screen the electric field of the core hole. If this rearrangement of the charge survives after the decay, a CT excitation is created. Another possibility is that the hole is produced on the oxygen site (when we work at the oxygen K edge). The excited electron is promoted to an empty O $2p$ orbital and another O $2p$ electron fills the O $1s$ core hole. There are two relevant scales for this process in the case of a transition-metal oxide: Δ, the energy difference between the metal and ligand site, and U, the energy required for an electron to jump among two metal sites. The bulk of transition-metal oxide compounds is in the charge-transfer limit (i.e. $U > \Delta$), meaning that the lowest lying excitations across

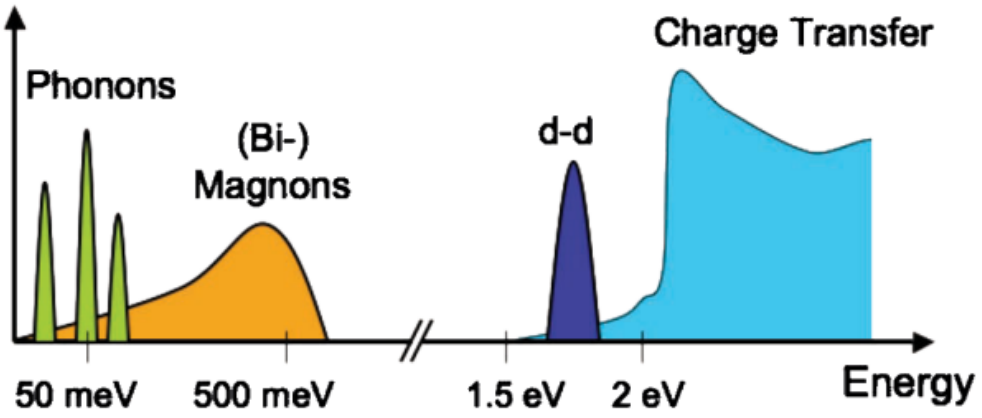

Figure 2.4: Excitations which can be probed by RIXS in a strongly correlated electron material. Figure taken from Ref. [66].

the optical gap are CT excitations. They are of main importance in determining physical properties of these materials.

c. Crystal-field and orbital excitations Depending on the way ions are positioned in the crystal structure, a split between electronic levels occurs (see Section 1.2.2). We can describe this by saying that there is a crystal electric field which is responsible for the splitting of electronic levels. We refer to the transitions between these crystal-field levels as orbital (intraband) excitations. When d orbitals are involved these transitions are called dd excitations. They appear in RIXS spectra and can be used to gain insight on the local symmetry of the ions [13]. Note that dd excitations are $\Delta L = 0$ transitions and thus electric-dipole forbidden. They are visible in RIXS because it is a second-order process.

d. Magnetic excitations When a material presents magnetic order, collective magnetic excitations emerge. They are called spin waves and can be described from a quantum point of view as quasi-particles called magnons. Their energy is typically limited to few hundreds of meV. When temperature is raised above the Curie temperature and long-range order is destroyed, some magnetic excitations can still exist in the form of damped spin waves. This is possible because a short-range magnetic order can survive.

e. Phonons The quantisation of the lattice vibration modes in a solid results in quasi-particles called phonons. They are bosons whose characteristic energy is typically below 0.1 eV. This is the reason why a good energy resolution is essential to be able to observe them in a RIXS spectrum. A RIXS process alters the charge distribution

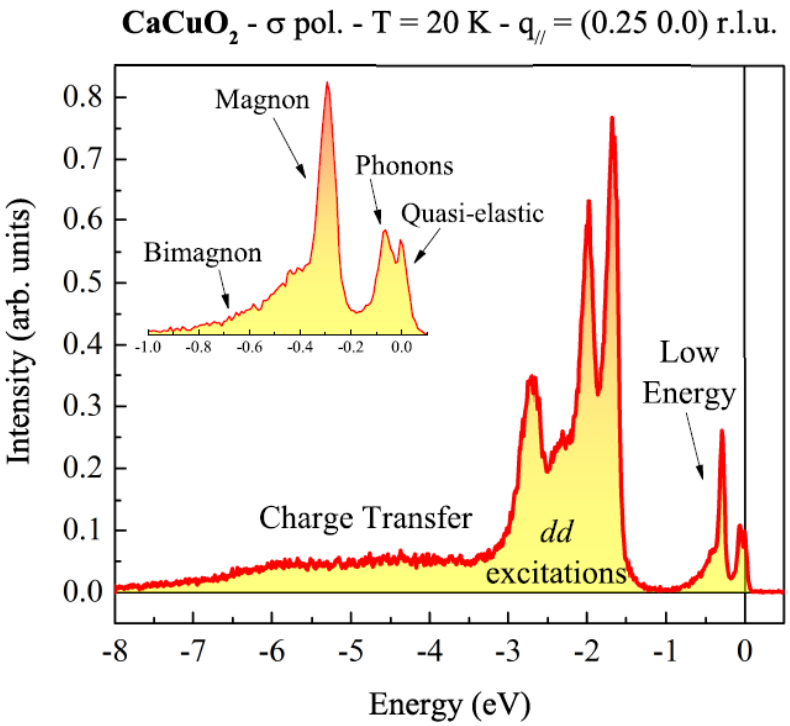

Figure 2.5: Example of a typical RIXS spectrum from a $CaCuO_2$ sample. One can distinguish charge transfer and *dd* excitations. The inset shows more clearly the low-energy excitations: phonons, magnons and bimagnons. The quasielastic peak appars at $\sim 0\,\text{eV}$. Figure taken from Ref. [67].

in the system. As a consequence, atoms repel or attract each other giving rise to lattice distortions.

In Fig. 2.5 an example of a typical RIXS spectrum is shown. It is possible to distinguish all the previously discussed features.

2.1.4. Further notes on RIXS spectra

The elastic peak is an important component of a RIXS spectrum. It is crucial to have in mind the phenomena which contribute to it. For instance, it could be required for the purpose of the experiment to minimise the elastic peak as much as possible in order to make the inelastic features more evident. A first contribution to quasi-elastic scattering is represented by low-energy phonons. Depending on the energy resolution of the RIXS measurement, scattering from phonons can be unresolved thus giving a signal at $E \approx 0$. Other contributions are instead related to diffuse scattering. This can be caused by defects or strain in the crystal. It is possible to minimise this phenomenon by working

with crystals of high crystalline quality. However, the condition of the sample surface could be relevant as well. The lower the quality of the surface of the sample, the higher the diffuse scattering and the more intense the elastic peak.
Additionally, it must be considered that an attenuation of the incident and outgoing photons takes place while they travel through the material. This attenuation, due to Auger processes and core-level fluorescence, is known as self-absorption. The scattering geometry is determinant since it defines the sample portion which interacts with the x-rays. When working on spectra collected at different scattering geometry it could be necessary to take into consideration this effect.

2.1.5. Theory of RIXS: brief introduction and results

In this Section the RIXS process will be discussed from a theoretical point of view. We will closely follow [66]. Let us consider a system initially at its ground state with energy E_g. The final state will be at energy E_f. The energy and momentum of the excitation are set by the conservation laws reported in Eq. 2.1. The energy equation can be also written using the frequencies, with ω representing the characteristic frequency of the excitation. Thus, the RIXS intensity can in general be defined as

$$I(\omega, \boldsymbol{k}, \boldsymbol{k'}, \boldsymbol{\epsilon}, \boldsymbol{\epsilon'}) = \sum_f |\mathcal{A}_{fg}(\boldsymbol{k}, \boldsymbol{k'}, \boldsymbol{\epsilon}, \boldsymbol{\epsilon'}, \omega_k)|^2 \times \delta(E_f + \hbar\omega_{k'} - E_g - \hbar\omega_k) \tag{2.2}$$

$\mathcal{A}_{fg}$ is the scattering amplitude which reflects which excitations are probed. The polarisation of the incoming and outgoing x rays appear as $\boldsymbol{\epsilon}$ and $\boldsymbol{\epsilon'}$, respectively. The first step is then to find a reasonable expression for $\mathcal{A}_{fg}$. For this purpose, the interaction between light and matter must be taken into account. The RIXS process consists in the absorption of a photon, in an intermediate short-lived unstable state and in the following decay through the emission of a photon. We are dealing with a two-step process which is not possible to characterise simply with the Fermi's golden rule. Instead, the Kramers-Heisemberg equation allows to describe higher order processes.
A system of N electrons, using the vector potential $\mathbf{A}(\mathbf{r}, t)$ to take into account the electromagnetic field of the incident x-ray beam, is described, in SI units, by

$$\begin{aligned} H = \sum_{i=1}^{N} \Big(\frac{[\mathbf{p}_i + e\mathbf{A}(\mathbf{r_i})]^2}{2m_e} + \frac{e\hbar}{2m_e}\boldsymbol{\sigma}_i \cdot \mathbf{B}(\mathbf{r}_i) + \frac{e\hbar}{2(2m_e c)^2}\boldsymbol{\sigma}_i \cdot \{\mathbf{E}(\mathbf{r}_i) \times [\mathbf{p}_i + e\mathbf{A}(\mathbf{r}_i)] + \\ - [\mathbf{p}_i + e\mathbf{A}(\mathbf{r}_i)] \times \mathbf{E}(\mathbf{r}_i)\} \Big) + \frac{e\hbar^2\rho(\mathbf{r}_i)}{8(m_e c)^2\epsilon_0} + H_{Coulomb} + H_{EM} \end{aligned} \tag{2.3}$$

where $\mathbf{p}_i$, $\mathbf{r}_i$, and σ_i are, respectively, the momentum and position operators and the Pauli matrices acting on i-electron. $\mathbf{E}(\mathbf{r})$ and $\mathbf{B}(\mathbf{r})$ are the electric and magnetic fields, respectively. The second term accounts for the Zeeman splitting, the third for the spin-orbit interaction. Moreover, the electron-electron interactions, electron-nucleus interactions and the presence of an external electric potential are all associated with the term $H_{Coulomb}$. Finally, H_{EM} is the Hamiltonian describing the electromagnetic field itself. It can be written using the annihilation and creation operators for the electromagnetic field. Perturbation theory will then be applied: the total Hamiltonian H is composed of an electron-phonon interaction part, named H', and by all the other terms which represent the unperturbed system and go under the name H_0. H' is thus seen as a perturbation of H_0. The transition rate for the electron-phonon scattering is given by the Fermi golden rule, which at second order yield:

$$w = \frac{2\pi}{\hbar} \sum_f \left| \langle f|H'|g\rangle + \sum_n \frac{\langle f|H'|n\rangle\langle n|H'|g\rangle}{E_g + \hbar\omega_k - E_n} \right|^2 \times \delta(E_f + \hbar\omega_{k'} - E_g - \hbar\omega_k), \tag{2.4}$$

where $|g\rangle$, $|n\rangle$ and $|f\rangle$ are, respectively, the initial, intermediate and final states. Note that they are also eigenstates of the unperturbed Hamiltonian H_0. Generally, the second order term is negligible with respect to the first order one. However, in resonance conditions, $E_g \approx E_f$ and the second term becomes relevant. Therefore, we have to only focus on the significant terms in H', i.e., those which are associated with the resonant process. We will not consider terms independent of the vector potential $\mathbf{A}$, which can be included in H_0, and all terms proportional to A^2. which are linked to non-resonant inelastic x-ray scattering. In addition, with the aim to take into account the possibility of non-radiative decay, a correction factor is introduced in the resonant part of the second order amplitude in the form of a lifetime broadening Γ_n. It is possible to show that resonant scattering occurs mainly via non-magnetic terms. Thus, ignoring the magnetic terms, the relevant operator for RIXS cross section is

$$\mathcal{D} = \frac{1}{im\omega_k} \sum_{i=1}^{N} e^{i\mathbf{k}\cdot\mathbf{r}_i} \boldsymbol{\epsilon} \cdot \mathbf{p_i} \tag{2.5}$$

Finally, the scattering amplitude is given by

$$\mathcal{A}_{fg}(\boldsymbol{k}, \boldsymbol{k'}, \boldsymbol{\epsilon}, \boldsymbol{\epsilon'}, \omega_k, \omega_{k'}) = \sum_n \frac{\langle f|\mathcal{D}'^{\dagger}|n\rangle\langle n|\mathcal{D}|g\rangle}{E_g + \hbar\omega_k - E_n + i\Gamma_n} \tag{2.6}$$

where the operator $\mathcal{D}'$ refers to transitions related to the emitted photon. Equations 2.2 and 2.6 together are called Kramers-Heisemberg equations and are usually employed to

evaluate the RIXS cross section.

2.2. Experimental setup

A RIXS experiment requires an x-ray beam with certain properties: it has to be a well-collimated and highly monochromatic beam impinging on the sample. Characteristics like these can be achieved by exploiting a synchrotron source and it is remarkable to say that great efforts have been recently done to improve the brightness in the energy ranges relevant for RIXS experiments. The spectrometer is the second essential component. It should allow to adjust the scattering geometry to vary the momentum transfer, collect the scattered radiation over an appropriate solid angle, and analyse the energy of the scattered radiation.
Over several years, incredible efforts have been made in order to obtain an outstanding improvement from the point of view of the energy resolution, maintaining a count rate high enough to carry out the experiments in a reasonable amount of time. This has allowed to distinguish features which was not possible to see with previous RIXS instrumentation. Furthermore, other limitations have been overcome in terms of scattering intensity, outgoing polarisation analysis and sample environment.
In this Section, after a brief illustration of synchrotron radiation, the basic ideas of a RIXS beamline will be introduced and the attention will be directed to the description of the main features of the ERIXS spectrometer at the ID32 soft x-ray beamline of the ESRF - the European Synchrotron, where the data which will be discussed in this thesis were obtained.

2.2.1. Synchrotron radiation

A synchrotron is an extremely powerful source of x-rays. It is basically a large ring in which electron bunches are accelerated to produce electromagnetic radiation. The resulting x-rays are directed towards beamlines located around the ring. The ESRF was the very first synchrotron of the third generation to be built. It was completed in 1991, delivering a stable source of high energy x-rays in Europe. Since then, many upgrades have been carried out, for example from the point of view of brilliance and beam size at the sample. The last project, the Extremely Brilliant Source (EBS) was launched in 2015, whose main purpose was the design and implementation of a new low-emittance storage ring. In Fig. 2.6 (a) the historical evolution of syncrotron sources and the ESRF upgrades are shown.

It is possible to identify several structures which compose a synchrotron facility. The

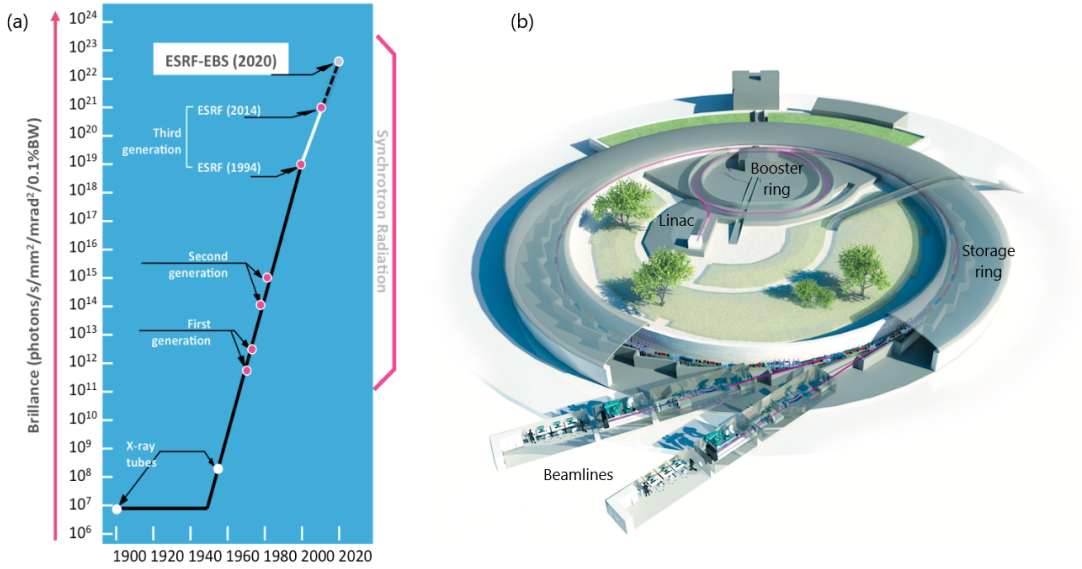

Figure 2.6: (a) Historical evolution of syncrotron sources and the ESRF upgrades. (b) The European synchrotron radiation facility (ESRF). Figures taken from Refs. [72, 73].

storage ring is a tube where the electrons travel at speeds close to the speed of light. Their trajectory is modified by the presence of different types of magnets and this leads to the emission of EM radiation. The tube is kept at very low pressure, around 1×10^{-9} mbar. In the specific case of the ESRF, the ring is 844 m long. The production of the electrons does not occur inside the storage ring, but in a nearby linear accelerator (LINAC). The electrons are generated by means of an electron gun and accelerated up to approx. 200 MeV. This energy value is sufficient for the injection of electrons in a smaller ring, which takes the name of booster synchrotron. Here, the electrons reach an energy of 6 GeV and finally are ready to be injected in the storage ring. Fig. 2.6 (b) displays the structure of a synchrotron radiation source.

The ESRF storage ring is characterised by 32 straight and 32 curved sections. In each curved section, two large bending magnets deflect the trajectory of the electrons. Instead, the straight sections accommodate many focusing magnets and also the undulators. The bending magnets creates a uniform magnetic field which forces the electron to move on an arc of circumference, whose radius is set by the magnetic field strength. Due to the deflection, the electrons emit x-rays tangentially to the plane of the electron beam. In the vertical direction, the radiation is emitted in a narrow cone with typical opening angle given by $1/\gamma$ rad, where γ is the relativistic gamma factor. The synchrotron light from a bending magnet covers a wide and continuous energy spectrum and, by comparison with the radiation leaving an undulator, it is much less focused, or brilliant. One disadvantage of the radiation coming from bending magnets is that it is not tunable. On the other

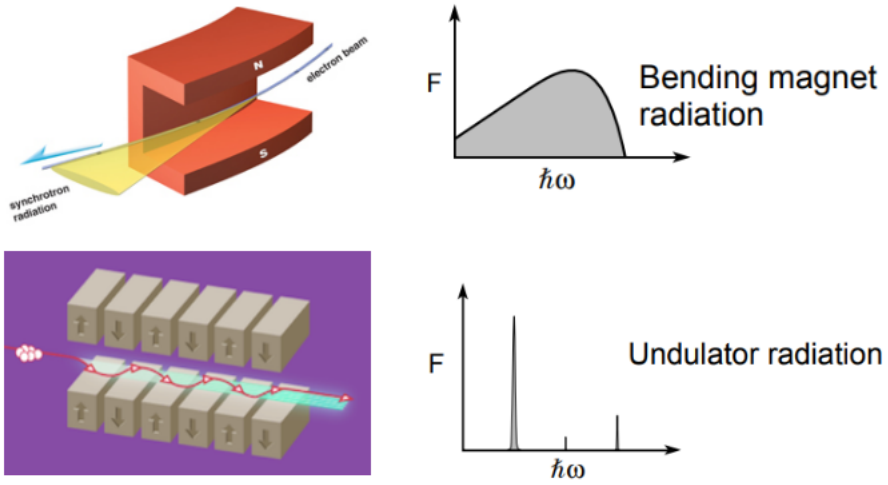

Figure 2.7: Two different kinds of EM radiation which can be generated in a synchrotron radiation facility. Top pictures are related to bending magnet radiation, whereas bottom pictures concern the radiation coming from undulators. In the graphs, F represents the photon flux. Figure adapted from Refs. [73–75].

hand, an undulator consists of a sequence of magnets. The magnetic fields are arranged so that the electrons undergo many small oscillations. Overlap and interference take place between the EM radiation at each consecutive bend. This has two main consequences on the properties of the radiation produced by an undulator: it is much more brilliant with respect to the radiation emitted by a single magnet, and, moreover, the emission does not cover a wide energy spectrum, but it is concentrated at particular energy values. This is a tunable source: by changing the gap between the rows of magnets, it is possible to get a peak of intensity for the desired wavelength. In Fig. 2.7 a summary of these two kinds of radiations is shown.

2.2.2. The experimental scheme

In this Section, a brief description of the standard experimental geometry used in a RIXS experiment will be outlined. In Fig. 2.8 both the real and reciprocal space are depicted. The meaningful vectors and angles are reported in panel (a). Letters a, b and c stand for the three real-space orthogonal base vectors of an orthorombic system (like YBCO and other cuprates). a and b point along the Cu-O bonds, whereas it is supposed that vector c is directed perpendicolar to the sample surface and lies in the scattering plane. This is the

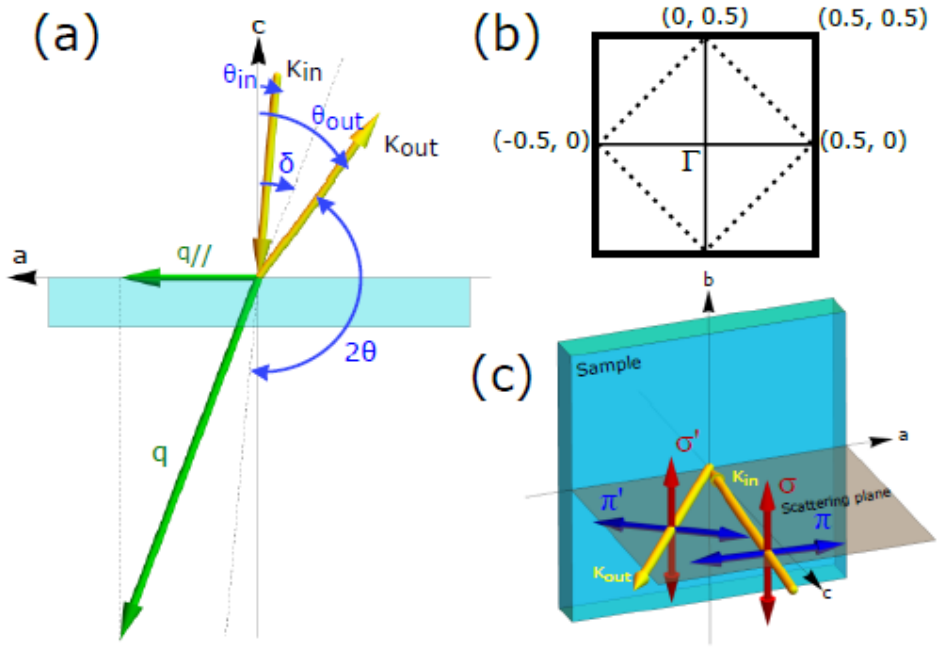

Figure 2.8: Meaningful vectors and angles involved in a RIXS event (a). Schematic illustration of the first 2D nuclear and magnetic Brillouin zones (b). 3D visualisation of the scattering geometry with emphasis on the photon polarisation (c). Figure adapted from Ref. [76].

situation for the majority of experiments. $\mathbf{k_{in}}$ and $\mathbf{k_{out}}$ represent the wavevectors of the incident and scattered photon, respectively. The total transferred moment is indicated by the vector $\mathbf{q}$ and obtained as the difference between $\mathbf{k_{in}}$ and $\mathbf{k_{out}}$. Nevertheless, since the main physics of cuprates occurs in the CuO_2 planes, a more relevant quantity is the projection $q_{\parallel}$ of the vector $\mathbf{q}$ onto the ab plane. Thus, the bi-dimensional nature of cuprates makes for easier experiments, allowing, for example, to limit our focus on the 2D Brillouin zone (shown in panel (b) of Fig. 2.8). The angle 2θ is the scattering angle, i.e., the angle between the directions of the vectors $\mathbf{k_{in}}$ and $\mathbf{k_{out}}$. It determines the maximum reachable amplitude of the vector $\mathbf{q}$ and directly appears in the analytical definition of $q_{\parallel}$ given by

$$q_{\parallel} = 2|k_{in}|sin\left(\frac{2\theta}{2}\right)sin(\delta) \tag{2.7}$$

where δ is the angle between the transferred momentum vector $\mathbf{q}$ and the c-axis. As described in Section 2.2.3, the sample orientation in the beam can be fully controlled through the 4-circle in-vacuum goniometer which allows to vary angles θ, χ and ϕ. They are also shown in Fig. 2.9 together with the hexagonal sample holder and their ranges of variations. The components of the total transferred momentum $\mathbf{q}$ can now be defined

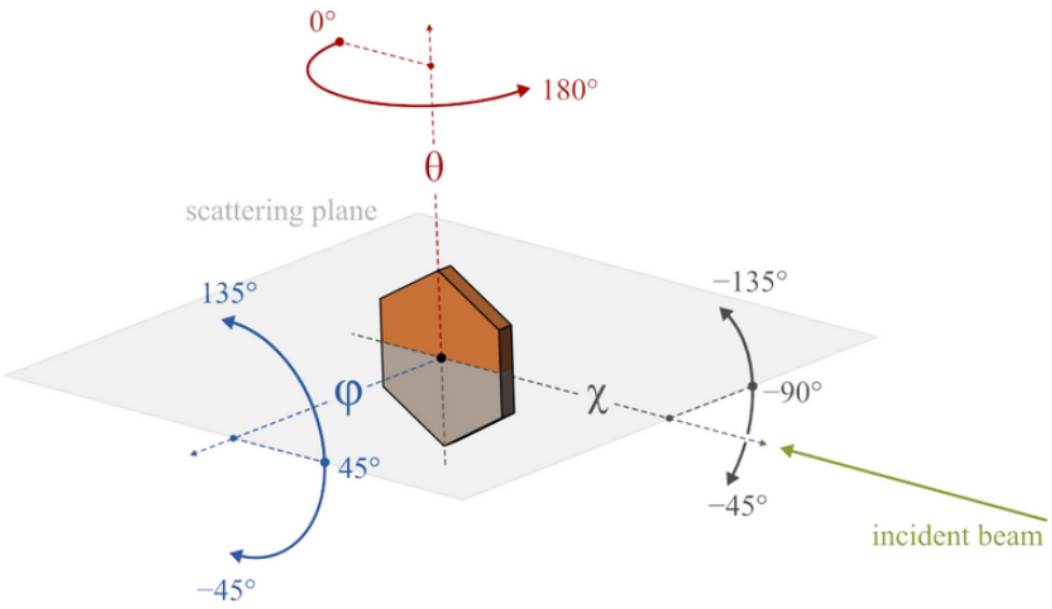

Figure 2.9: The hexagonal sample holder and the angles adjustable by the goniometer with their ranges of variation. Figure taken from Ref. [77].

through these angles. In particular, the Miller indices correspond to the components of $\mathbf{q}$ normalised with respect to the reciprocal lattice vectors $2\pi/a$, $2\pi/b$ and $2\pi/c$, where a, b and c are the real lattice constants of the material under study. Assuming an orthorombic unit cell and $\phi = 0$, the analytic definition of the Miller results to be

$$\begin{aligned} H &= \frac{a}{2\pi}|\mathbf{q}|sin(\delta) \\ K &= \frac{b}{2\pi}|\mathbf{q}|cos(\delta)sin(\chi) \\ L &= \frac{c}{2\pi}|\mathbf{q}|cos(\delta)cos(\chi) \end{aligned} \tag{2.8}$$

where the modulus of $\mathbf{q}$ is given by $|\mathbf{q}| = 2|\mathbf{k}_{in}|sin(2\theta/2)$. By gradually varying δ angle and keeping 2θ fixed, there is the possibility of mapping the spectral features in momentum space. The angle δ is directly linked to the angle θ by the relation $\delta = \theta - 2\theta/2$.
It is important to make a remark about the sign of Miller index H. The same holds for K. Positive and negative values correspond to two different geometries. To positive H values is assigned the almost normal-in grazing-out configuration, whereas the inverted configuration is assigned to negative H values.
Finally, panel (c) of the same figure points out that the photon polarisation is a further degree of freedom available for the investigation of the sample. The direction of the electric field vector $\mathbf{E}$ can be chosen either parallel (π) or perpendicular (σ) with respect to the scattering plane. These two components can be differentiated thanks to the polarimeter

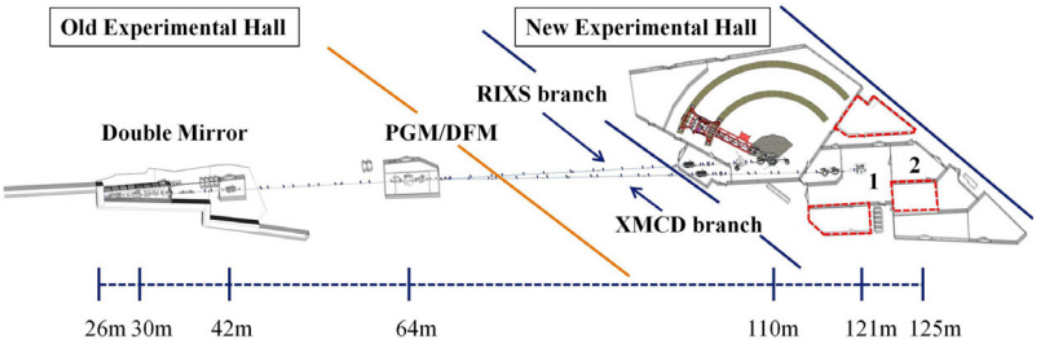

Figure 2.10: ID32 beamline floor plan – the distances are given from the source. The control cabins are highlighted by red dashed lines. Figure taken from Ref. [78].

device the ID32 beamline is equipped with. Polarisation degree of freedom is useful to investigate phenomena where a transfer of photon angular momentum takes place. This is the case, for instance, of magnon excitations.

2.2.3. The ID32 beamline and the ERIXS spectrometer

Information provided in this Section are mainly based on Ref. [78]. The ID32 soft x-ray beamline is an ESRF upgrade beamline for x-ray absorption (XAS) and resonant inelastic x-ray scattering (RIXS) studies. It supplies polarised soft x-rays whose energy is tunable in the 400 eV–1600 eV range. This energy range is suitable for the study of materials based on $3d$ transition metals as well as on $4f$ rare earths. Indeed, the $L_{2,3}$ absorption edges of 3d transition metals (Ti-Cu) is in the 400 eV–1000 eV energy range and the rare-earth $M_{4,5}$ edges lie in the 900 eV–1500 eV range. Therefore, the beamline allows to investigate materials such as high-temperature superconducting cuprates. Moreover, the photon polarisation can be fully controlled; circular, linear vertical, and linear horizontal beam polarisation rates are basically 100%.
Two branches are present (see Fig. 2.10): one branch allows to carry out x-ray magnetic dichroism experiments, both linear (XMLD) and circular (XMCD). The other branch is designated to very high energy resolution resonant inelastic x-ray scattering experiments. The spectrometer is characterized by an 11 m long scattering arm which is able to continuously rotate over 100 degrees without breaking the ultra-high vacuum (UHV) conditions. A full control of the sample position is guaranteed by a four-circle sample goniometer. It makes possible the accurate positioning of the sample and, therefore, the 3D mapping of q space. A last feature of interest is the availability of the polarisation analysis of the radiation scattered from the sample.

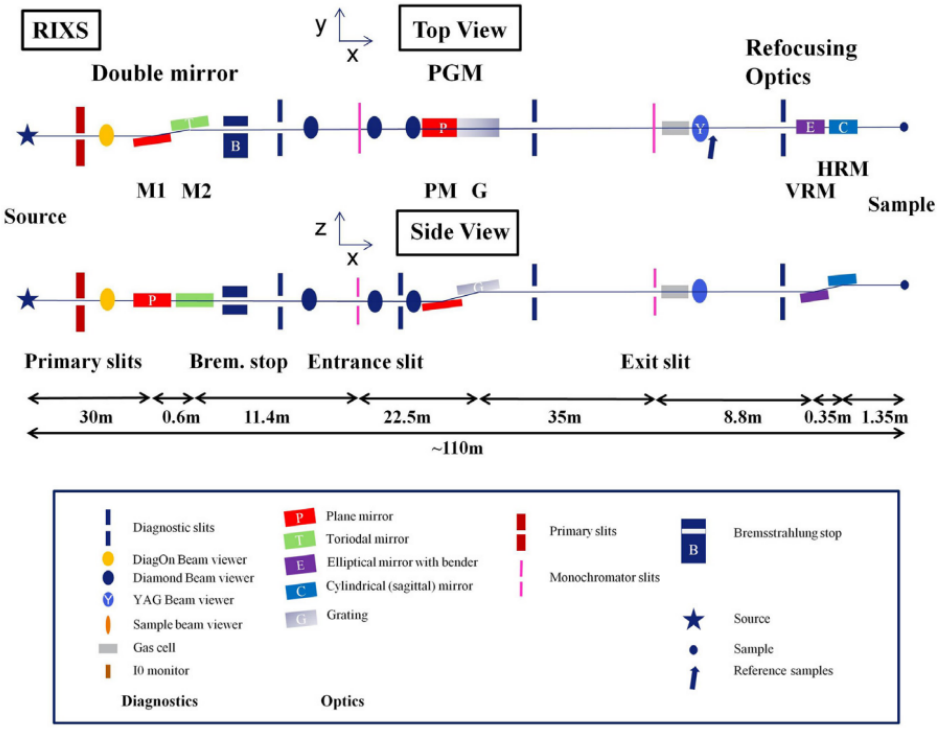

Figure 2.11: ID32 beamline optical layout of the RIXS branch. Figure from Ref. [78].

In Fig. 2.11 the ID32 beamline optical layout of the RIXS branch is displayed. Some of the illustrated components are shared with the XMCD branch, but we will just describe some of the main components belonging to the RIXS branch.

a. RIXS sample chamber This is a UHV vacuum chamber where a a four-circle UHV diffractometer is placed. Two ion pumps and one turbomolecular pump guarantee a pressure in the order of 1×10^{-9} mbar or less. Furthermore, samples can be stored in another small chamber and they can be moved from air up to the main chamber, without breaking the vacuum, through a fast load lock. This process takes more or less thirty minutes.

b. RIXS diffractometer It is shown in Fig. 2.12. A full sample control is available, in order to set the desired scattering geometry and investigate the targeted region of the reciprocal space. In addition to the regulation of the angles θ, χ and ϕ, the translation of the sample with respect to the centre of rotation is allowed. Moreover, the detector stage 2θ, even though it shares the same axis as θ, it is completely independent of it. The resolution is at least 0.001 deg for rotations and within 1 μm for translations. If needed, the sample can be cooled through copper braids by a liquid helium flow. Normal low operating temperature is 20 K. Finally, the possibility of performing transport measurements or applying electric fields is made

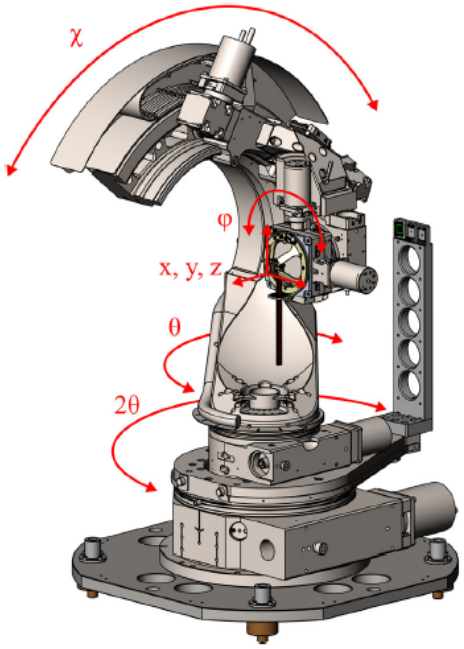

Figure 2.12: The in-vacuum sample goniometer and the allowed motions. Figure taken from Ref. [78].

possible by eight electrical connections to the sample.

c. RIXS spectrometer The spectrometer is composed of three vacuum chambers in succession. The pressure inside them is kept at a base value less than 2×10^{-9} mbar. The first chamber houses a collimating parabolic mirror, whereas the second chamber holds two variable line spacing spherical gratings. These have been optimised to obtain a resolving power $E/\Delta E$ around 25000 at optimum flux condition, or 40000 for the highest resolution scheme. The third chamber is placed at the end of the scattering arm. Here the multilayer for polarimetric analysis is positioned and can be moved in or out of the direct beam depending on the purpose of the experiment. Lastly, two soft x-ray detectors, one for the direct beam and one for the beam scattered by the multilayer, are placed at the end of the chamber. Exploiting a single photon detection and centroid determination, their in-plane spatial resolution is approx. $7\,\mu$m. There is the possibility to continuously vary the scattering angle from 150 deg to 50 deg by moving the scattering arm. The vacuum is only weakly perturbed during the motion, but it is quickly restored.

From the point of view of RIXS performance, the Tab. 2.1 summarise the three configurations which are normally used, depending on the desired energy resolution and photon flux. Not only the gratings, but also the aperture of the exit slits are directly involved in

the determination of the photon flux on the sample and of the achievable energy resolution.

	Monochromator grating $[lines/mm]$	Spectrometer grating $[lines/mm]$	Relative through-put	Energy resolution at Cu L_3 edge $[meV]$
low resolution, high through-put	800	1400	x12	42
medium resolution, medium through-put	800	2500	x4	32
high resolution, low through-put	1600	2500	x1	28

Table 2.1: Three different configurations and the corresponding achievable energy resolution with exit slit aperture fixed at 15 μm. Values taken from Ref. [77].

As a final remark, it should be noted that several diagnostic tools are available for visualising the beam and testing each component in the beamline. They include screen monitors, intensity monitors, variable slits and spectral characterisation tools.
In the following and last Chapter the experimental results will be presented.

3 | Samples and experimental results

In this Chapter we will present the analysis performed on the experimental data. After a brief description of the samples and related experimental details, the results will be discussed in two different sections. The former is related to the quasielastic part of the RIXS spectra and the investigation of the presence of charge density waves in $YBa_2Cu_4O_8$, along with their temperature dependence. The latter deals with the data analysis of the inelastic part of the high-resolution RIXS spectra, which allows the study of the phononic and magnetic excitations.

3.1. Samples

$YBa_2Cu_4O_8$ samples represent the heart of the experimental study which will be presented hereafter. They have been grown by the "Crystal Growth" group at Max Planck Institute for solid state research (Stuttgart, Germany). They performed the growth at ambient air pressure by using a flux method [79]. KOH (potassium hydroxide) was selected as a flux to grow Y124 samples, which allows to obtain high-quality single crystals without overcoming 550 °. It is important to mention that we are dealing with Y124 samples with unprecedented dimensions (≈ 1 mm in lateral size). Some of the samples, especially the one characterised by a smaller size, had smooth and clean surfaces. On the contrary, other samples have undergone polishing in order to get cleaner surfaces and reduced roughness. Finer and finer polishing papers have been employed. Polishing has the advantage of reducing the elastic scattering contribution due to the roughness. One can see the difference between unpolished and polished surface on a Y124 sample in panels (a) and (b) of Fig. 3.1. It is also evident the presence of regions characterised by two different colours. Indeed, Y124 exhibits in-plane anisotropy because of the presence of the copper chains (as discussed in Section 1.3): the chains are oriented along the b-axis making it non-equivalent to the a-axis. Since we took these pictures with a microscope with a polarisation filter, we have been able to distinguish the two different types of

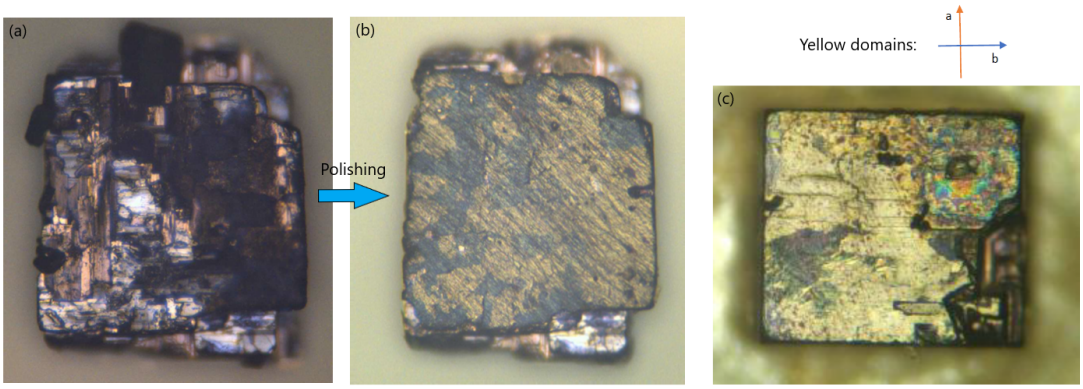

Figure 3.1: All the pictures display Y124 samples and have been collected with a microscope with a polarisation filter. (a) Surface of a sample before polishing. It appears dirty and holes are clearly visible, indicating the the sample thickness is not uniform. (b) The same surface after polishing. It is now cleaner and smoother. Regions characterised by different colours correspond to different domains, depending on the orientation of the a and b axes of the crystalline Y124 structure. The sketch above picture (c) helps understand the orientation of the axes in each domain displaying a yellow color under the polarized light of the microscope. (c) Sample on which the majority of measurements have been performed. It exhibits a huge "yellow" domain. This is a non-polished sample.

domain according to the orientations of the two axes. Panel (c) displays the sample on which the majority of measurements have been performed. It was chosen because it exhibits a large untwinned domain at the surface, likely expanding in volume in the bulk as well, in order to collect data from a single domain. The yellow color in the image corresponds to a domain with a and b axes aligned as in the sketch of Fig. 3.1 (c), with chains running along the b-axis. Importantly, the beam size at the sample is $4 \times 60\,\mu\text{m}^2$ (FWHM). The capability of discerning between the two domains is important to study how charge density waves and inelastic scattering features can be affected depending if the incident beam polarisation is set parallel or perpendicular to the copper chains.

3.2. Experimental details

We collected RIXS spectra on $YBa_2Cu_4O_8$ (Y124) at the ID32 beamline of the ESRF. We measured the Cu L_3 edge and, thus, the impinging photon energy was set at $E_{res} = 931.38\,\text{eV}$ for most of the measurements, corresponding to a wavelength $\lambda \approx 1.32\,\text{nm}$. Vertical ($\sigma$) polarisation has always been used to maximise the RIXS signal coming from charge ordering phenomena [45].
For the measurements we used to investigate charge density waves, we decided to employ

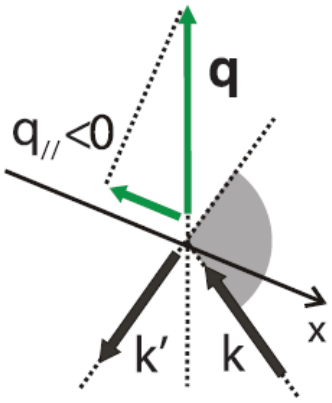

Figure 3.2: The grazing-in almost normal-out configuration is depicted, highlighting the corresponding negative value for the transferred in-plane momentum. Here **k** is the incoming photon momentum and **k'** is the momentum of the scattered photon. Figure from Ref. [45].

the 800 lines/mm monochromator grating and to keep the exit slit aperture at 30 μm. This choice ensures faster measurements and an energy resolution $\Delta E \approx 65.5$ meV which is appropriate for the energy-integrated analysis. Differently, spectra aimed at investigating the dispersions of magnetic and phononic excitations require to distinguish between the different kinds of low-energy spectral features and thus have been collected by setting the exit slit aperture at 15 μm, yielding an energy resolution $\Delta E \approx 35$ meV.
We performed most of the measurements with the incoming beam polarisation vertical (σ geometry) and aligned perpendicular to the sample b-axis, that is parallel to the copper chains, unless otherwise specified. We measured in grazing incidence geometry with the outgoing beam near the normal to the surface, corresponding to negative values for the Miller indices H and K as shown in Fig. 3.2. Since we are interested in investigating the $2D$-reciprocal space corresponding to the CuO_2 planes, the scattering angle 2θ was kept at 150 °. This is the maximum allowed 2θ value and it maximises the in-plane momentum as Eq. 2.7 demonstrates. By varying the angle θ is then possible to collect spectra at different H (or K) value and thus to map the dispersion of a specific spectral feature in the momentum space. The analytic formulas to calculate the Miller indices are reported in Eq. 2.8.

3.3. Observation and temperature dependence of charge density waves in $YBa_2Cu_4O_8$

This Section is dedicated to the investigation of the presence of charge density waves in Y124. After explaining the motivations for this experiment and presenting the raw data, the collected spectra will be fitted and analysed.

3.3.1. Motivation of the experiment

Charge density waves have been observed in a huge variety of cuprates materials characterised by different chemical compositions and doping levels. Their existence in Y124 have been inferred since this compound exhibits the presence of Fermi surface electron pockets, as confirmed by quantum oscillations experiments [60]. This is a typical feature of cuprates in which charge order arises. Nevertheless no direct evidences of CDWs in Y124 have been reported to date. Moreover, Y124 gives us the exceptional opportunity of investigating a compound with a clean stoichiometry, even at high temperatures. This is a huge difference with respect to its relative Y123, in case CDWs were observed also in Y124, as their evolution upon temperature is believed to be affected by the presence of defects, acting as pinning centers for the CDWs.

3.3.2. RIXS spectra and energy-integrated data

Spectra have been collected at several K values in the range $[-0.46, -0.17]$ r l u with a 0.01 r l u step. First of all, we will take into account the RIXS spectra collected at $T_C = 80\,\mathrm{K}$ [52] as CDWs are expected to be maximized at T_C, if present. As a reference, the CDW signal in Y123 [45] increases upon cooling as long as $T > T_C$. Below T_C, superconductivity arises and charge order gets weaker since these two phases compete with each other. Fig. 3.3 (a) reports some RIXS spectra collected on the Y124 sample at different K values. Three major features can be identified in each spectrum. The elastic peak is the one centred around zero energy loss. It derives from elastic scattering events but it also includes the contribution coming from low-energy excitations such as phonons. That is why it would be more appropriate to refer to it as quasielastic peak. Phonons cannot be easily disentangled from the elastic peak since these data have been collected with an energy resolution of 65.5 meV. They will be further investigated in Sec. 3.4 where we will discuss high-energy resolution spectra.
The spectral feature which corresponds to the magnetic excitations is marked by the label "spin". Since Y124, characterised by a doping level $p = 0.14$ [80], lies well outside the

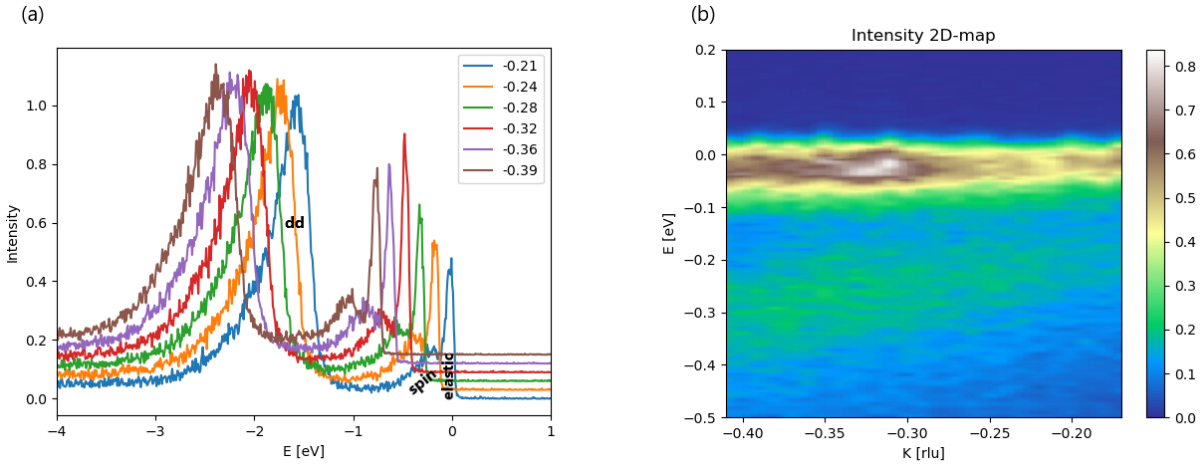

Figure 3.3: Data collected at $T_C = 80\,\mathrm{K}$. (a) Selected spectra collected at different K values. Elastic, spin and *dd* spectral features are indicated. The elastic line of the spectrum at $K = -0.32\,\mathrm{r\,l\,u}$ shows an enhancement with which can be ascribed to the presence of CDWs. (b) Colormap showing the RIXS intensity as a function of the energy and momentum K. A clear higher-intensity white spot appears around $K = -0.32\,\mathrm{r\,l\,u}$, which can be ascribed to the presence of CDWs. The shaded green area below $-0.15\,\mathrm{eV}$ is related to magnetic excitations.

antiferromagnetic phase (see Fig. 1.9), the antiferromagnetic order exists only locally and no more as a long-range order. Therefore, these spin excitations observed in RIXS spectra are not magnons but rather paramagnons, that is, damped spin waves.

The last evident spectral feature is represented by the *dd* (intraband) excitations. They are the result of electronic transitions between different $3d$ states. Thus, *dd* excitations are not allowed by dipole transition, but they are possible in RIXS via the two dipole allowed transitions of absorption and emission of a photon that make up the resonant scattering process. Analysing *dd* excitations allows one to assign the spectral contributions coming from transitions involving different $3d$ states [81] and retrieve crystal field characteristic parameters [13]. However, this is not the focus of this thesis. We will just make use of *dd* excitations as a normalisation factor for the spectra. We remind as well that the spectral features have been discussed in detail in Sec. 2.1.3.

Focusing now on the quasielastic peak, we observe that its amplitude changes as a function of K reaching a maximum at $K = -0.32\,\mathrm{r\,l\,u}$. The relative increase is not as marked as in Y123 data [45], but it is nonetheless very evident and recognisable. Moreover, the maximum is found at a similar K value. Charge order is a modulation of the charge density of Fermi electrons. Even though it typically comes together with a lattice distortion, it represents an energetically favourable configuration since the reduction in the

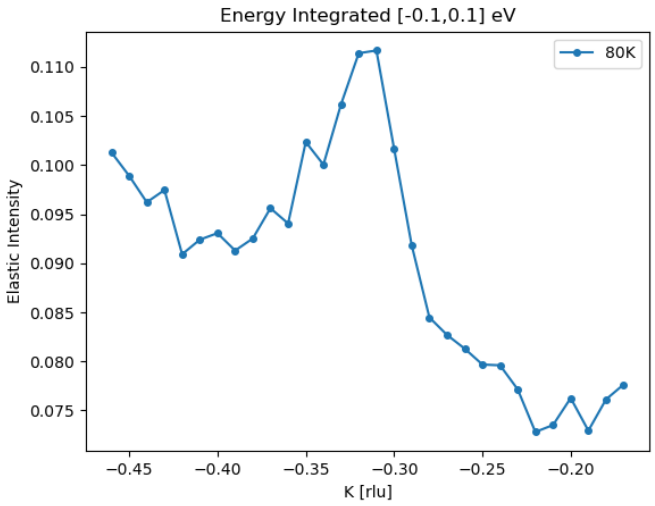

Figure 3.4: Energy integrated spectrum in the quasielastic range $[-0.1, 0.1]$ eV at T_C. The peak exhibits the maximum value at $K = -0.31$ r l u .

electronic energy compensates any other energy growth. It is a new ground state which appears in RIXS spectra as a static elastic scattering due to the modulation of the valence charge. Fig. 3.3 (b) supplies a more comprehensive view. It shows a colormap of the RIXS intensity as a function of both energy and momentum. It is even clearer the presence of a charge density waves as indicated the higher-intensity white area in the range $K = [-0.34, -0.30]$ r l u. An increase of the intensity for large $|K|$ values should be ascribed to an increasing background. It is possible as well to identify the spin excitations as the shaded green region included between -0.4 eV and -0.15 eV. We will discuss paramagnons later on in Sec. 3.4. In the following, we will considered the energy-integrated RIXS spectrum in the range $[-0.1, 0.1]$ eV. As one can realise from the colormap the quasielastic contributions, modulated by the CDW signal, are well confined within this energy range, which excludes the contribution deriving from spin waves. Integrating over this energy range can thus allow to monitor the intensity of the CDW signal as a function of the momentum. In Fig. 3.4 the above-mentioned energy-integrated spectrum at the SC critical temperature is reported. One can observe a roughly linear background above which CDW peak is present. It reaches the largest intensity at $K = -0.31$ r l u . In the following, we will analyse the intensity and shape of CDW signal and background.

3.3.3. Energy dependence

We will now discuss the energy dependence of the quasielastic signal together with the x-ray absorption spectroscopy (XAS). They are reported in Fig. 3.5 (a). Two sepa-

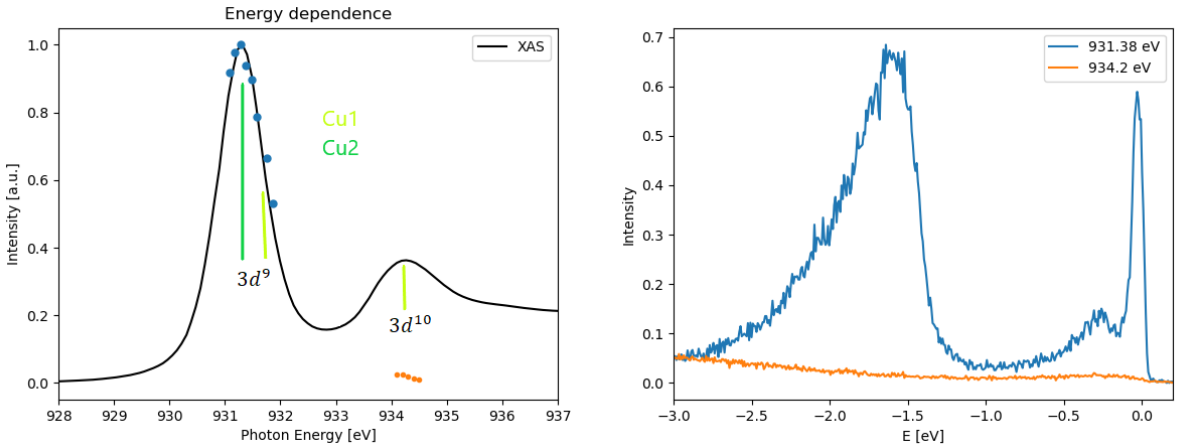

Figure 3.5: (a) The black line corresponds to the XAS, whereas blue and orange points show the energy dependence of the quasielastic signal obtained by RIXS. Quasielastic signal refers to the integration of the RIXS spectra in the energy range $[-0.1, 0.1]$ eV. XAS and RIXS data have been collected at room temperature and 80 K, respectively, and have been normalised. Cu1 and Cu2 label copper atoms in CuO chain layers and CuO_2 planes, respectively. Vertical bars indicate relevant absorption peaks. (b) RIXS spectra collected at $K = -0.32$ r l u when the incident photon energy is set at the resonant (blue) or off-resonant (orange) energies.

rated peaks are identifiable in the XAS. The first peak lies at energy around 933.2 eV in correspondence of the Cu1 $3d^{10}$ configuration. Therefore, it confirms that this is the electronic configuration for copper atoms inside Y124 chains. The second peak is localised at $E \approx 931.4$ eV and it is associated with the Cu2 $3d^9$ configuration of the copper atoms belonging to the CuO_2 planes. Let us consider now the data points related to the RIXS quasielastic intensity. Its energy profile shows an enhancement in correspondence of the electronic configuration of planar coppers, whereas a suppression is present at the energy of chain Cu. This incident photon energy dependence is clear as well in raw RIXS spectra shown in Fig. 3.5 (b). They were collected at 931.38 eV (blue) and 934.2 eV (orange). The direct conclusion is that charge order must be only connected to the modulation of planar coppers' valence electrons.

3.3.4. Temperature dependence

We took RIXS spectra for a large set of temperatures, thus allowing to obtain a detailed temperature dependence. We will take into account the energy integrated data in the interval $[-0.1, 0.1]$ eV. Fig. 3.6 displays the temperature evolution of the CDW signal in the analysed Y124 sample. Upon increasing temperature, the background signal in-

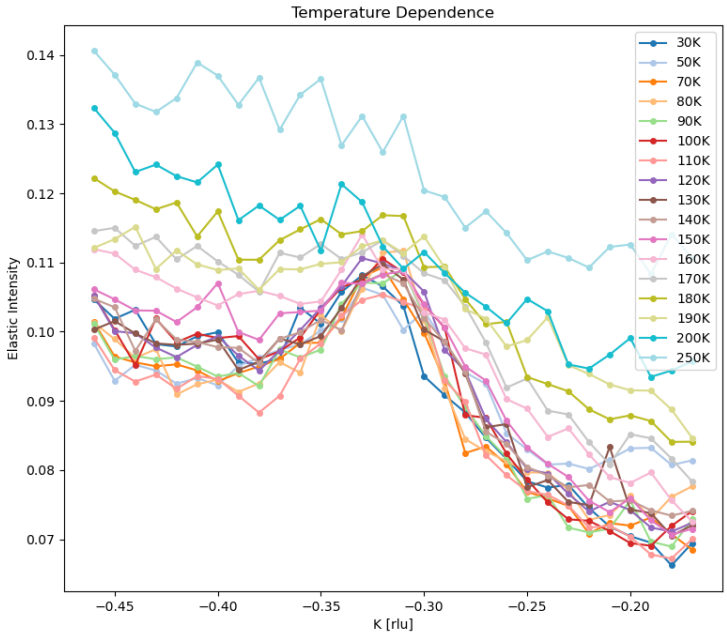

Figure 3.6: Energy integrated spectra in the quasielastic range $[-0.1, 0.1]$ eV at several temperatures between 30 K and 250 K. The underlying background is progressively increasing with temperature. At lower temperatures a CDW signal is recognisable as the presence of a peak. By raising temperature the CDW peak seems to decrease in intensity and to broaden until it is not evident anymore at 200 K and 250 K.

creases. By considering one spectrum at a specific temperature, it is also evident, that the background is monotonically increasing with $|K|$. The peak in the energy integrated data, which is present for temperatures both below and above T_C, indicates the existence of CDWs in a wide temperature range. The peak seems to decrease in intensity (with respect to the background) and to broaden upon warming until it is not recognisable anymore in the 200 K and 250 K scans. In the following Section we will discuss how to subtract the background, in order to extract a detailed temperature dependence,

Background

The presence of CDWs have been clearly observed in several cuprate materials when moving along K and H directions in the reciprocal space. Peaks in energy integrated data are the sign of their existence. Nevertheless, no peaks appear in the data when an (H, H)-scan is performed, i.e., when moving along the reciprocal space diagonal. Some theories tries to explain this by taking into account the shape assumed by the Fermi surface

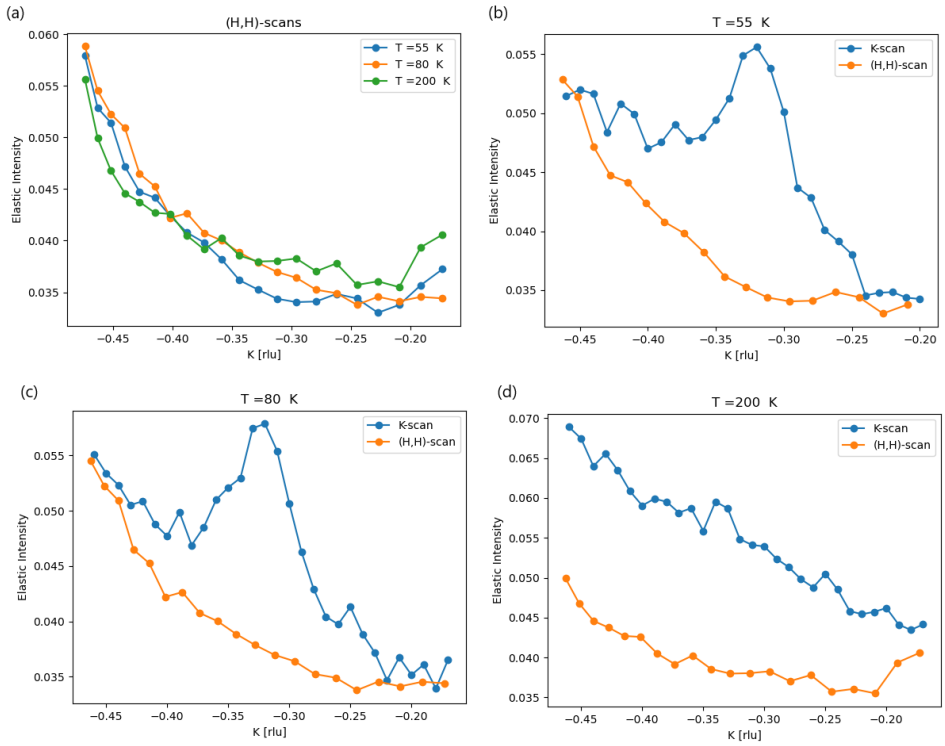

Figure 3.7: (a) Measurements taken along the reciprocal space diagonal at temperatures 55 K, 80 K and 200 K. Intensity always corresponds to the energy integration of spectra between -0.1 eV and 0.1 eV. No strong differences between the three measurements are visible. Others panels reports each (H, H)-scan together with the corresponding K-scan. At 55 K (b) and 80 K (c) the diagonal scan nicely matches the edges of the K-scan, whereas at 200 K the two data sets do not show any kind of relation.

in the pseudogap regime. The nesting vectors, which connects the closest point of nearby Fermi arcs, seem to be directly connected to the CDW characteristic momentum [42, 82]. We collected spectra along the reciprocal space diagonal at 55, 80 and 200 K. To do so, the angle theta has been varied in the range $[20, 60]$ degrees with a $2\,^\circ$ step. One can see the corresponding quasielastic intensities in Fig. 3.7 (a). Indeed, no peak is recognisable. The three curves are pretty much similar between each other, both in intensity and in the shape characterised by a positive concavity. Since CDWs are not observed in the diagonal scans, one may have the idea to use them as backgrounds for the scans along the H and K directions. This was the method followed by Arpaia *et al.* [51] as discussed in Section 1.2.4. Therefore, we tried making a comparison between each diagonal scan and the corresponding K-scan at the same temperature. The plots are shown in Fig. 3.7. The diagonal background matches the CDW scans at the extremes of the investigated K range at 55 K (b) and 80 K (c). Nevertheless, the diagonal scan collected at 200 K cannot be used as a background for the corresponding K-scan. Due to this incompatibility and

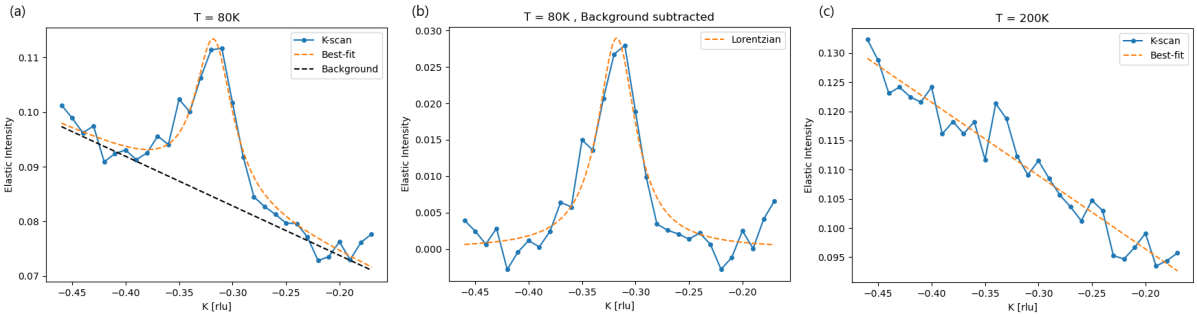

Figure 3.8: (a) Best fit and linear background for the scan at 80 K. Panel (b) shows the same data as panel (a) after subtracting the straight line. A Lorentzian lineshape fits the peak which is left. (c) The scan at 200 K can be fitted by the linear component alone.

looking at the extremes of the K-scans, we decided that a simple linear background is the easiest solution compatible with all scans. This is further supported by the linear trend shown by the two measurements at the largest temperatures (200 K and 250 K) where no peak associated with charge order is identifiable, in stark contrast with the evident residual broad peak, present in the work of Arpaia *et al.* [51].
We fitted the data with a Lorentzian lineshape on top of a linear background. Fig. 3.8 shows the result at T_C and at high temperature, whereas the fits for all the T values can be found in Appendix A. Panel (a) shows the best fit and the linear background for data at $T_C = 80$ K. One can notice that the straight dashed line is capable of fitting properly the edges of the K-scan. After subtracting the linear background the residual signal is plotted in panel (b). The CDW peak well-fitted by the Lorentzian lineshape is evident. The last panel reports the K-scan collected at 200 K. In this case the linear component alone is sufficient to fit the data.

Temperature dependence after background subtraction

After subtracting each background from the corresponding K-scan, we plotted all the obtained curves in Fig. 3.9 (a). The temperature dependence is now straightforward. At high temperatures the peak, centred around -0.32 r l u , is broad, whereas it becomes narrower when cooling down towards the critical temperature. This is also the temperature at which the quasielastic intensity reaches the largest value. By further decreasing the temperature below T_C, the CDW signal seems to decrease. For the two highest temperatures (200 K and 250 K) we have previously shown that the linear component of the fit alone is already able to fit the data. Indeed, what is left after the background subtracted for these two spectra is essentially only noise. In Fig. 3.9 (b) a colormap shows the temperature evolution, confirming a maximum at $T_C = 80$ K.

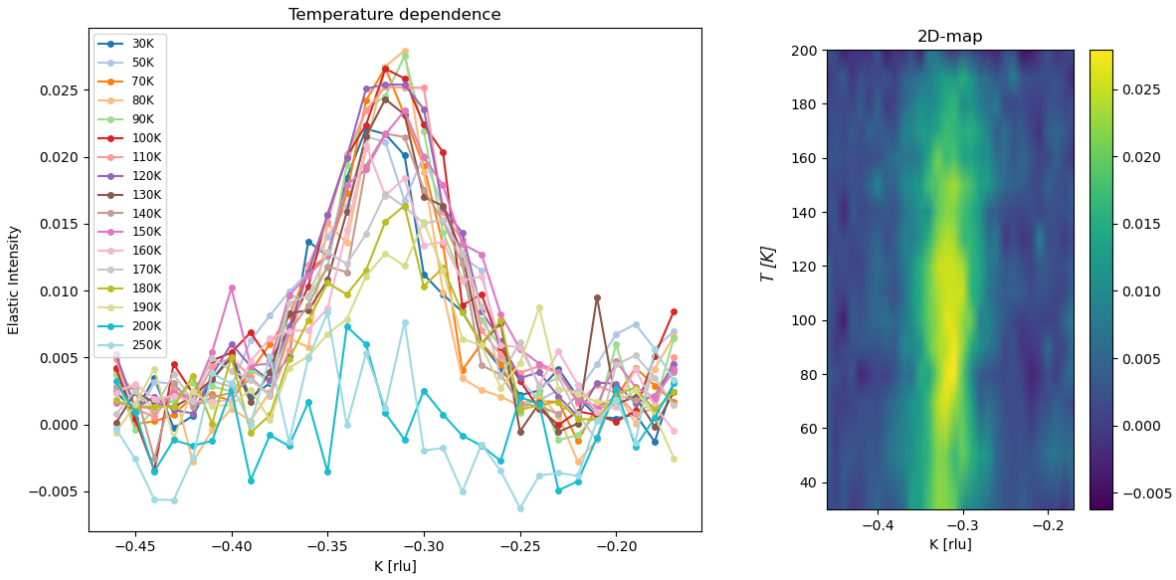

Figure 3.9: Temperature dependence after background subtraction. In panel (a) elastic intensity as a function of K is represented for each temperature value, in analogy with Fig.3.6. The colormap in panel (b) shows the temperature evolution. From both panel it is evident that a CDW arises at momentum $K \approx -0.32\,\mathrm{rlu}$ and that a peak of elastic intensity is reached when $T = T_C$.

Fig. 3.10 (a) displays the height of the Lorentzian fit of the CDW peak as a function of temperature. According to our data, since any evidence of CDWs is not present at 200 K or above, we can consider the value $T_{CDW} \approx 190\,\mathrm{K}$ as onset temperature for charge order in Y124. The concave-downward shape of the quasielastic peak intensity resembles an order parameter of broken symmetry. Thus, we decided to use the power law of an order parameter to fit the data points.

$$Intensity \propto (order\ parameter)^2 \propto (T_{CDW} - T)^{2\beta} \tag{3.1}$$

Since our data show the first zero-intensity point at 200 K, we used this temperature value as critical temperature T_{CDW} of the order parameter law. The fit, realised by considering the data points in the interval 80 K–200 K, is depicted in the same picture. The best fit value for the β parameter is 0.173 ± 0.011. The good agreement between the data and the power law fit strongly suggests that the clean stoichiometry of Y124 allows CDWs to develop as a true phase transition starting from high temperatures and with the correlation quickly converging to a finite value.
To make a comparison with the related Y123 compound, 3.10 (b) reports our results together with the data collected on $YBa_2Cu_3O_{6.6}$ by Blanco-Canosa *et al.* [48]. Data have

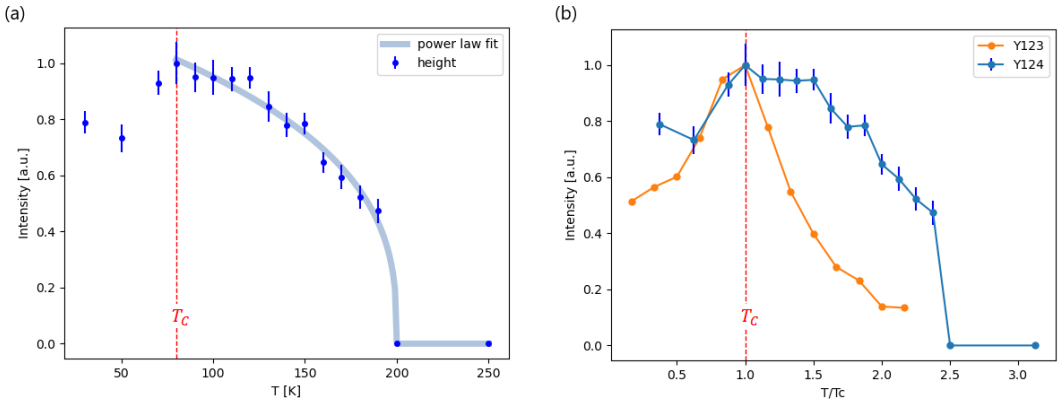

Figure 3.10: (a) Temperature dependence of the CDW peak height. Error bars, which represent a standard deviation of the fitting parameter, are also indicated. The maximum value is reached at the SC critical temperature. The blue curve is the result of the power law fitting. (b) Comparison between temperature dependence in Y124 and Y123 compounds. Data have been normalised according to their critical temperature ($T_C(Y123) \approx 60\,\mathrm{K}$). Y123 points have been extrapolated from Ref.[48].

been normalised along both axes. Both data sets are peaked at the critical temperature, but the temperature dependence exhibited by Y124 is markedly different from that of Y123, especially above T_C. One possible explanation for this discrepancy could be attributed to the oxygen stability which characterises the Y124 compound, in contrast with Y123, which carries intrinsic stoichiometric defects associated with the oxygen content in the CuO chain layers. Additionally, for Y123 the onset temperature for charge order assumes the lower value of approx. 150 K [83]. Below T_C, the two data sets are more similar, reconfirming the competition between charge order and superconductivity.

Fig. 3.11 displays the full width at half maximum (FWHM) of the Lorentzian fitting component showing a weak minimum at T_C. The correlation length at T_C assumes a value $\xi = a/(\pi \cdot FWHM) \approx 22\,\text{Å}$, where a is one of the in-plane lattice parameters. The characteristic CDW momentum in Y124 is nearly identical to the one of Y123 with similar doping level [48] at all temperatures, i.e. $K = -0.32 \pm 0.005$.

3.3.5. Measurement along the (1,0)-direction

So far, we have studied CDWs in Y124 by moving in reciprocal space along the $(0, 1)$-direction, i.e., by varying the K value. This corresponds to a configuration in which the vertical (σ) polarisation of the incoming x-ray beam is oriented perpendicular to the copper chains. We will now compare these data with H-scans measured only at T_C, along the $(1, 0)$-direction and across $K = K_{CDW}$. For these scans the σ polarisation

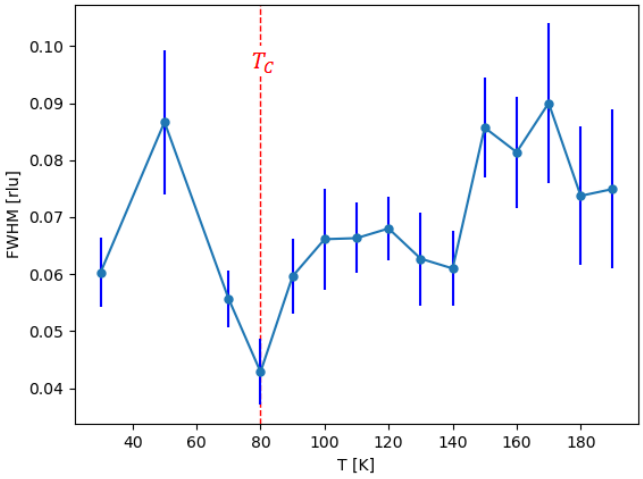

Figure 3.11: FWHM of the Lorentzian peak as a function of temperature. Error bars, which represent a standard deviation of the fitting parameter, are indicated. The FWHM exhibits a weak minimum at the critical temperature and it seems to grow by moving away from T_C.

is parallel to the Y124 chains, that is, parallel to the b-axis. Fig. 3.12 (a) shows the quasielastic intensities across $(H, K) = (0, -0.32)$ and $(H, K) = (-0.32, 0)$, where linear backgrounds have been subtracted. Along both H- and K-directions, it is possible to observe the quasielastic peak, which is characterised by similar FWHMs. Additionally, the characteristic momenta for CDWs along the two directions, H_{CDW} and K_{CDW}, share the same value around $-0.32\,\mathrm{r\,l\,u}$. Fig. 3.12 (b) displays the H-scan at $(H, K) = (0, -0.32)$. Its FWHM is approx. two times wider than those of a-CDW and b-CDW. This obviously reflects on the correlation lengths whose anisotropy is represented in the inset of Fig. 3.12 (a) by an ellipse. What is important to notice is that the a- and b-CDW peaks in reciprocal space in Y124 samples are very similar to those observed in Y123 [48]. This means that the a- and b-CDW domains in real space are also similar. In particular, their elongated form in the direction of the CuO chains (exactly as in detwinned Y123) also confirms we are mostly probing a single detwinned domain. Supplementary material related to the fitting results can be found in Appendix A.

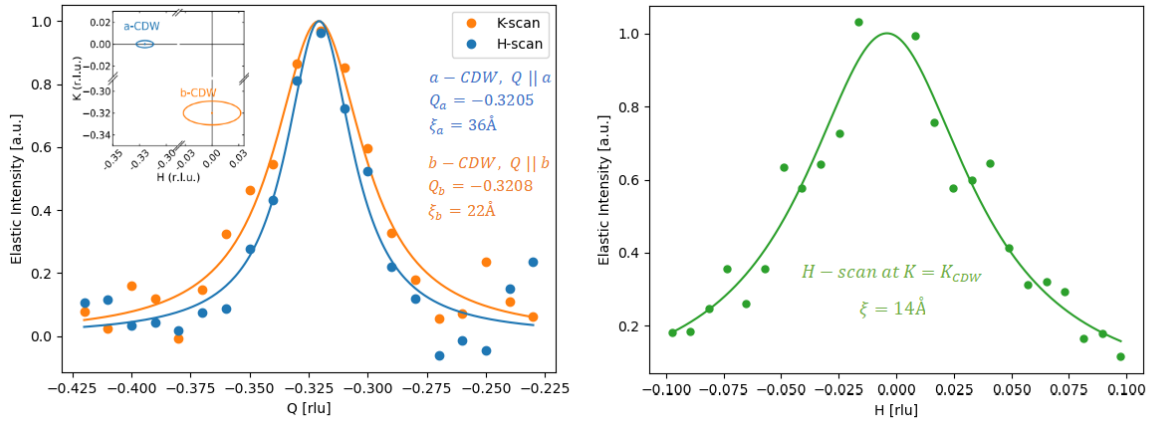

Figure 3.12: (a) Comparison between H- and K-scans around $-0.32\,\mathrm{r\,l\,u}$ collected at the SC critical temperature. Data points refer to the quasielastic intensity after background subtraction and lines are the fitted Lorentzian profiles. Inset: peak positions in the reciprocal space based on FWHMs of Lorentzian fits. In panel (b) the H-scan at $(H, K) = (0, -0.32)$ is reported. Correlation lengths ξ have been calculated in each case highlighting that the quasielastic peak in (b) is approx. two times wider than peaks in (a).

3.4. Phonons and magnetic excitations in Y124

This Section is dedicated to a detailed analysis of the inelastic part of high-resolution RIXS spectra collected on Y124. The RIXS data we have analysed so far were collected with an energy resolution around 65.5 meV. Hereafter, we will exploit high-resolution measurement with $\Delta E \approx 35\,\mathrm{meV}$ to study phonons and magnetic excitations in Y124. Particular interest will be dedicated to their dispersions in the reciprocal space.

3.4.1. High-resolution RIXS spectra

We performed high-resolution RIXS measurements at the SC critical temperature $T_C = 80\,\mathrm{K}$. We collected spectra moving along the $(H, K) = (0, 1)$ direction in the reciprocal space, in particular, for K belonging to the interval $[-0.50, -0.06]\ \mathrm{r\,l\,u}$, with a step of 0.02. An extra point has been taken at $K = -0.31\,\mathrm{r\,l\,u}$. We set the incident photon energy at $E_{res} = 931.38\,\mathrm{eV}$ and σ-polarisation was used.

In Fig. 3.13 (a) one can see an example of high-resolution RIXS spectrum. By making a comparison with the spectra collected at lower resolution (see Fig. 3.3) more spectral features are now observable. Indeed, in the inset it is evident the presence of an additional peak at low energies which is now disentangled from the elastic peak. The "new" peak is associated with lattice vibrations, that is, phonons. We will discuss phonons in detail

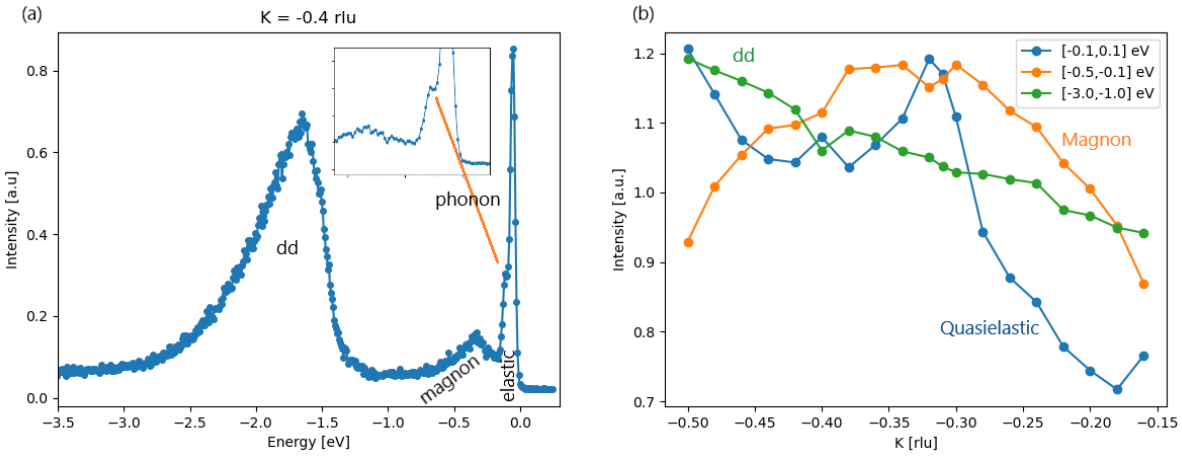

Figure 3.13: (a) RIXS spectrum collected at $K = -0.4\,\mathrm{r\,l\,u}$ where the spectral features are highlighted. Interorbital excitations (dd), magnetic excitation and the elastic components are labelled. The inset display a zoom of the lower energy region which highlight the presence of a further peak ascribable to lattice vibrations. (b) Energy integration over specific energy ranges which allows to have an idea of the K-dependence of the spectral features.

later on. The peak associated with magnetic excitations and the interorbital excitations (dd) were already recognisable in the lower resolution spectra.
A first valid approach to study the momentum dependence of the different types of intrinsic excitations is to consider the energy integration of the spectra over specific ranges. By looking at Fig. 3.13 (a) and taking also into account the colormap in Fig. 3.3, one can realise that dd excitations are found in the range $[-3.0, -1.0]$ eV of energy loss, whereas the paramagnons, which extend over a very wide energy range, can be found in the interval $[-0.1, -0.5]$ eV. The quasielastic peak ($[-0.1, 0.1]$ eV) consists of the elastic scattering contribution together with the lowest energy excitations, including phonons. We have extensively discussed its direct connection to the CDW signal in the previous Sections. The results of the energy integration are plotted in 3.13 (b). The trend of the quasielastic contribution is consistent with previous discussions: a peak is present around $K = -0.32\,\mathrm{r\,l\,u}$, which is ascribable to charge ordering phenomena. dd excitation have a weakly decreasing trend as the transferred in-plane momentum is increased. This trend can be used as a reference to normalise spectra. Magnetic excitations show a very broad peak which reaches a sort of highest intensity plateau from $-0.38\,\mathrm{r\,l\,u}$ to $-0.30\,\mathrm{r\,l\,u}$. Theoretical calculations for the cross sections would be able to explain this trend [13].
However, the discussion we can conduct about these excitations is limited since, by integrating the spectra, we get only information about their spectral weight. High-resolution measurements allow for a more detailed investigation.

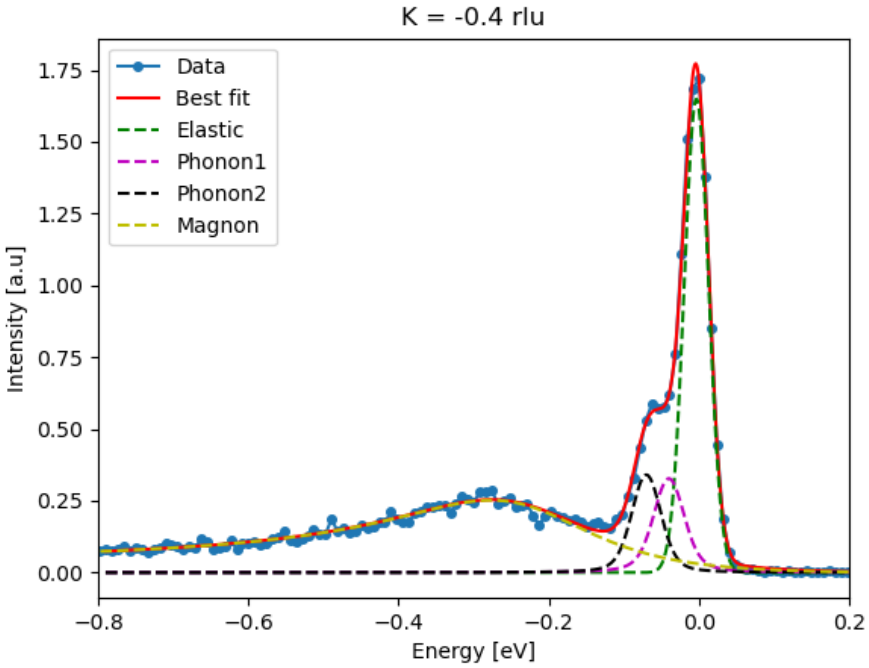

Figure 3.14: Data fitting of the RIXS spectrum collected at $K = -0.40\,\mathrm{r\,l\,u}$. The best-fit is indicated by the red line, whereas each dashed line represents one specific spectral feature.

3.4.2. Data fitting of the high-resolution RIXS spectra

Data have been fitted using a non-linear least squares method. The fitting function was defined as the sum of four different components, each of them related to a specific spectral feature. The elastic peak is fitted with a Gaussian function centred around zero. Its FWHM has been fixed to the width of the combined experimental resolution of beamline and spectrometer. As far as phonons are concerned, we firstly have to say that, in cuprates, RIXS is able to probe two main vibrational modes. They are the buckling mode, which consists in the vibration of planar oxygen atoms out of the CuO_2 planes, and the breathing mode, related to the stretching of Cu-O bonds. Due to the similarities between cuprate systems, given that they are all characterised by the CuO_2 planes, we will take NBCO as a reference for the energy values of these vibrational modes. NBCO presents energies of $\approx 35\,\mathrm{meV}$ for the buckling mode and $\approx 70\,\mathrm{meV}$ for the breathing mode [84], , with very little dispersion for both of them. We then used two different Voigt profiles, each of them representing one of the two phonons ("phonon 1" has been used to label the buckling mode, whereas "phonon 2" labels the breathing mode). The Voigt profile is the result of the convolution between a Lorentzian and a Gaussian profiles. The former is intrinsic

to the excitation's profile, while the latter is due to the experimental resolution. The last fitting function is the one representing the paramagnon. An appropriate function should be chosen such as one capable of modelling the asymmetric shape of the magnetic feature. This damped and asymmetric shape is common to excitations which strongly interact with others. One of the most used functions is the damped harmonic oscillator [85]; however, we decided to employ the Fano lineshape which turns out to be a better fit for the shape of the magnetic peak. Its analytic formula is given by the following equation:

$$F(x, A, \overline{x}, \Gamma, q) = A\frac{(q\Gamma/2 + x - \overline{x})^2}{(\Gamma/2)^2 + (x - \overline{x})^2} \tag{3.2}$$

where A is the amplitude, $\overline{x}$ represents the centre of the lineshape, Γ is related to its width and q is the Fano factor, directly connected to the level of asymmetry. This function has been convoluted with a FWHM-constrained Gaussian to take into account the experimental resolution. In Fig. 3.14 the data fitting carried out on a selected RIXS spectrum is reported as an example. Together with the best fit all the fitting components are depicted. The function representing the paramagnon extends over the whole fitted range, while, previously, we just integrated over the energy range where a higher magnetic signal is present. Supplementary material with the data fitting at each K-value is available in Appendix A.

3.4.3. Elastic line

Fig. 3.15 (a) reports the momentum dependence of all the spectral features. It was calculated by taking into consideration the area of each component. As far the elastic component is concerned, one can notice that it displays a trend similar to to the quasielastic component of Fig. 3.13: a peak around $-0.32\,\mathrm{r\,l\,u}$ is still present. The less intensity is obviously related to the fact that the quasielastic contribution was calculated considering the energy range $[-0.1, 0.1]$ eV, which includes the phonons as well, whereas the fitted elastic peak takes out the other (quasielastic) contributions. By considering the trend of phonon 1 as a function of K, we can state that it is characterised by an enhancement in the region around K_{CDW} as well. The elastic component strongly grows when approaching the condition of zero in-plane momentum transfer, which corresponds to the case of specular reflection. Fig. 3.15 (b) shows the intensity colormap related to the elastic component of the fit.

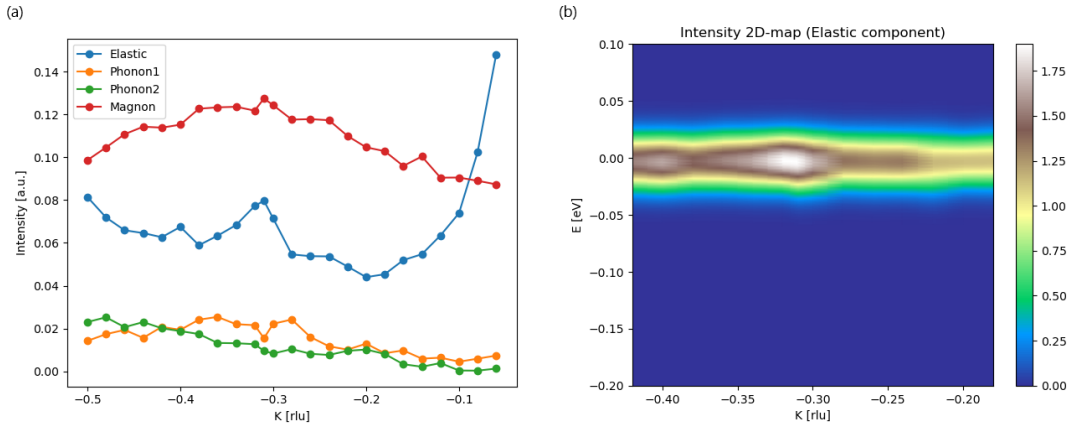

Figure 3.15: (a) Momentum dependence of all the spectral features realised thanks to the data fitting. (b) Intensity colormap for the elastic line created from the elastic component of the fit. The white area indicates the high-intensity region where CDW arises.

3.4.4. Phonons

We have already mentioned above that RIXS is capable of detecting two different lattice vibration modes in cuprates, the buckling and the breathing modes. We have an idea of the associated phonon energies since studies have been conducted on other cuprate materials. Similar energies are expected for Y124 phonons. Therefore, these energy values have been employed in the data fitting to set suitable boundaries to the position of the two phonons. By taking again into consideration Fig. 3.15 (a), the K-dependence of phonon 1 shows an enhancement of the intensity in the central momentum region, where CDW arises. The same behaviour is recognisable in the intensity colormap related to the buckling mode alone visible in Fig.3.16 (a). Therefore, phonon 1 gives a contribution to the quasielastic intensity at K_{CDW}, but, as its dispersion is almost flat around K_{CDW}, the CDW peak is entirely given by the elastic line. Phonon 2 is characterised by a decreasing trend when moving from $-0.50\,\mathrm{r\,l\,u}$ to $-0.06\,\mathrm{r\,l\,u}$. The coupling between phonons and electrons is a consequence of the lattice deformation: the kinetic energy of electrons is modified since lattice vibrations change the way in which orbitals of nearby ions overlap. The breathing mode shows a strong momentum dependence and gives a higher contribution to the RIXS intensity at larger momenta. Since the larger the momentum, the shorter the spatial periodicity of the lattice vibrations, a more pronounced deformation of the lattice and a stronger electron-phonon coupling take place at larger $|K|$ [86]. The colormap depicting the breathing mode intensity is shown in Fig. 3.16 (b). The enhancement in intensity when moving towards higher $|K|$ values is evident. Panel (c) has been shown to compare with our results. It depicts the breathing mode intensity

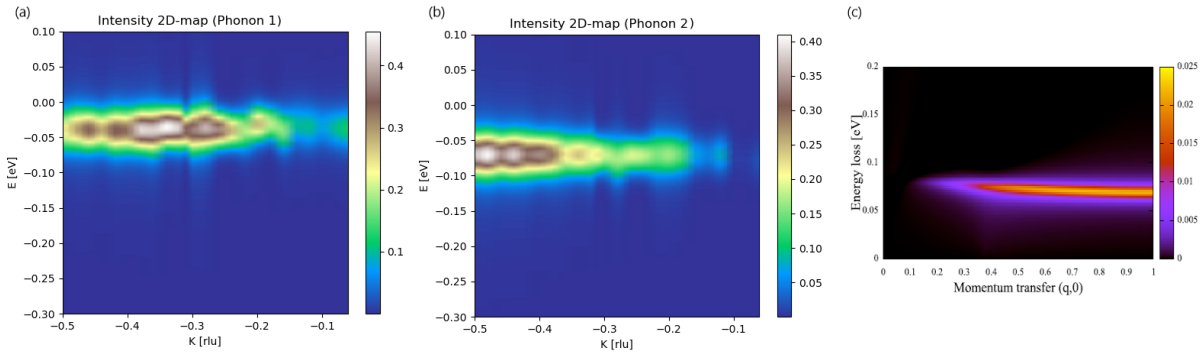

Figure 3.16: Panels (a) and (b) represent the intensity maps related to the phonon 1 and phonon 2 components of the fit. Panel (c) depicts the result of a theoretical treatment for the breathing mode that is possible to compare with our results for phonon 2. It has been taken from Ref. [86].

map calculated through an 8-band Cu-O model. This is part of a work by Devereaux *et al*. [86] focused on the oxygen modes shared to all perovskite oxides. The similarity with our phonon 2 intensity map is clearly visible.
Therefore, RIXS can be a useful tool to retrieve information about the momentum dependence of the electron-phonon coupling. This is not particularly interesting when dealing with BCS superconductivity, where the pairing mechanism shows *s*-wave symmetry, but it could be when unconventional superconductors [87] are taken into account. By employing RIXS together with other complementary techniques, such as ARPES or neutron scattering, the strength of electron-phonon interaction across the Brillouin zone can be reconstructed [88, 89]. This interaction is at the base of conventional superconductivity, but it could participate in stabilising the SC state even in unconventional superconductors.

3.4.5. Magnetic excitations

RIXS allows to study the dispersion of magnetic excitations in reciprocal space. As the Y124 doping level places it far away from the antiferromagnetic phase, let us remind the reader that we are dealing with damped spin-waves, referred as paramagnons in a quantum picture. The possibility of probing (para)magnons by RIXS derives from the fact that the incident photon carries angular moment. This can be transferred to the material under study during a RIXS event and paramagnons, characterised by $\Delta S = 1$, can thus be excited. Bimagnons can be excited as well. They consists of double spin-flip excitations with $\Delta S = 2$, correponding to two counter-propagating spin waves. Actually, the Fano function we selected to fit the magnetic component of the spectrum does not take into account only paramagnons, but includes also bimagnons and, in general, a

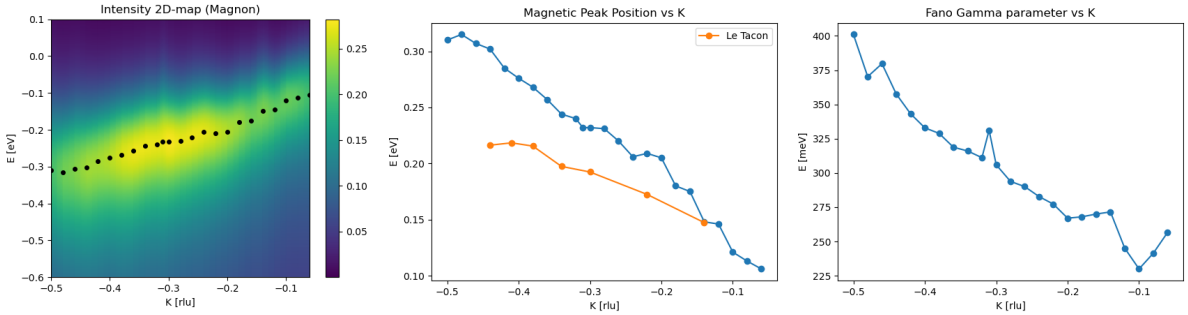

Figure 3.17: (a) Intensity colormap for the magnetic component of the fit. Black points are related to the position of the paramagnon peak and give an idea of the magnetic dispersion. (b) Magnetic dispersion and comparison with Y124 data from Ref. [90]. (c) Fano gamma parameter vs K.

background. However, this lineshape turns out to be useful as it is able to properly fit the peak related to the paramagnon, since the bimagnon excitation becomes very weak very quickly as the doping is increased in cuprates. Fig. 3.17 (a) reports the intensity colormap. The paramagnon dispersion is highlighted by black points and it is also shown in panel (b). This is the typical dispersion of the spin-waves in antiferromagnets, which for the complete Brillouin zone assumes the trend reported in Fig. 2.3. Our data looks different from the ones collected by Le Tacon *et al* [90] on the same compound. The results we show seem to confirm an energy at the BZ boundary of around 300 meV and, thus, similar to other cuprate systems [90]. This discrepancy can be due to the better quality of the Y124 crystals and the absence of multidomain configurations in our samples. Lastly, in Fig. 3.17 (c) the gamma parameter of the Fano function as a function of K is depicted. It gives information about the width of the lineshape thus showing its increase towards higher $|K|$ values. This is a common behaviour of this kind of excitations, but can also come from the interaction with other excitations. However, this considerations are beyond the scope of this work.

Conclusions and future developments

This thesis presents experimental results collected on the underdoped cuprate $YBa_2Cu_4O_8$ (Y124). We analysed high-quality single crystal samples grown by the "Crystal Growth" group of Max Planck Institute for solid state research (Stuttgart, Germany). The experiments were conducted at the ID32 beamline of the European Synchrotron (ESRF), which houses a pioneering high-resolution resonant inelastic x-ray scattering (RIXS) setup.
We used Cu L_3 edge RIXS on the Y124 samples to investigate the presence of charge density waves (CDWs). Indeed, we observed a peak in the quasielastic intensity which is ascribable to a charge order phase. The peak is centred at a similar momentum value as observed in other cuprate families, such as $YBa_2Cu_3O_{6+x}$ (Y123). Furthermore, the presence of the CDW signal was confirmed along both the in-plane directions of the reciprocal space, with unidirectional domains similar in shape and size to those observed in YBCO. By studying the energy dependence of the quasielastic signal we came to the conclusion that charge order is associated with the valence electrons of the CuO_2 planes' copper atoms alone. We also considered the temperature evolution of the CDW signal in Y124. To do so, we fitted the K-scans with a Lorentizian lineshape on top of a linear background. Looking at the data after subtracting the background, we noticed a discrepancy in the temperature dependence of the quasielastic intensity with respect to what happens in the Y123 compound characterised by a similar doping level. At high temperatures, it shows a trend comparable to an order parameter of broken symmetry. We attributed this behaviour to the clean stoichiometry which characterises Y124: the presence of a double chain layer in the crystal structure distinguishes it from Y123 (that has only one chain layer per unit cell) and enhances its chemical and structural stability. This defect-free scenario should allow the CDWs to fully develop as a second order phase transition.
We also collected RIXS spectra with high-resolution, around 35 meV. They allowed us to conduct a detailed study of the dispersions of the inelastic RIXS features in the reciprocal space. This was possible by fitting the energy spectra with the sum of different functions, each of them representing a specific feature of the RIXS spectrum. We analysed the behaviour of the two vibrational modes, the buckling and the breathing modes, which RIXS is able to probe in cuprates. These modes are shared by other cuprate systems and our

results for the breathing mode are in accordance with the predictions given by an 8-band Cu-O theoretical model. Considering magnetic excitations, we focused on the spin collective modes which arise from Cu atoms in the CuO_2 planes. We tracked their dispersion in the reciprocal space, observing that they are characterised by an energy value around 300 meV at the edge of the first Brillouin zone, in analogy to other cuprate materials.
Our findings demonstrates that CDWs are present in the Y124 system and give an outlook about the correlation between disorder and charge ordering phenomena. The unique stoichiometric nature of Y124 represents a great opportunity to conduct further clean measurements. For instance, we investigated only the spin waves arising from Cu atoms in the copper oxygen planes, but the other Cu subsystem, represented by copper atoms in the CuO chains, can give rise to spin excitations as well. In particular, it would be of interest to study their dimensionality. Information about 3D-CDWs could be obtained by moving along the L direction in the reciprocal space and potentially applying high magnetic fields. 3D-CDWs should appear in the superconducting dome as observed in other cuprate systems. Additionally, the behaviour of Y124 physical properties under strain could be investigated. It still remains unclear why no CDW peak appears when moving along the reciprocal space diagonal. Some theories try to explain this by taking into account the shape assumed by the Fermi surface in the pseudogap regime, but further measurements on Y124 and other cuprate materials could help clarify this open question.
To conclude, we can say that our results will inform future investigations and theoretical models of charge and spin collective phenomena in high-T_C cuprate superconductors and akin quantum materials.

Bibliography

[1] H. K. Onnes, "The Superconductivity of Mercury." Comm. Phys. Lab. Univ., Leiden, 122-124, 1911.

[2] B. Keimer, S. Kivelson, M. Norman, *et al.*, "From quantum matter to high-temperature superconductivity in copper oxides," *Nature 518*, pp. 179–186, 2015.

[3] A. Drozdov, M. Eremets, I. Troyan, *et al.*, "Conventional superconductivity at 203 kelvin at high pressures in the sulfur hydride system," *Nature 525*, pp. 73–76, 2015.

[4] E. Snider, N. Dasenbrock-Gammon, R. McBride, *et al.*, "Room-temperature superconductivity in a carbonaceous sulfur hydride," *Nature 586*, pp. 373–377, 2020.

[5] J. Bardeen, L. N. Cooper, and J. R. Schrieffer, "Theory of Superconductivity," *Phys. Rev.*, vol. 108, pp. 1175–1204, Dec 1957.

[6] J. C. Swihart, "Isotope Effect in the Bardeen-Cooper-Schrieffer and Bogoliubov Theories of Superconductivity," *Phys. Rev.*, vol. 116, pp. 45–52, Oct 1959.

[7] L. N. Cooper, "Bound Electron Pairs in a Degenerate Fermi Gas," *Phys. Rev.*, vol. 104, pp. 1189–1190, Nov 1956.

[8] N. W. Ashcroft and N. D. Mermin, *Solid State Physics*, ch. 22: Classical Theory of the Harmonic Crystal. Holt-Saunders, 1976.

[9] M. Chergui, "Localized holes and delocalized electrons in photoexcited inorganic perovskites: Watching each atomic actor by picosecond X-ray absorption spectroscopy Localized holes and delocalized electrons in photoexcited inorganic perovskites: Watching each atomic actor by picosecond X-ray absorption spectroscopy," *Structural Dynamics*, vol. 4, 2017.

[10] W. Prestel, "Study of the Interaction Processes in Cuprate Superconductors by a Quantitative Comparison of Spectroscopic Experiments," Technisce Universitat Munchen, 2012. https://mediatum.ub.tum.de/doc/1099353/1099353.pdf.

[11] N. Barišić, M. Chan, Y. Li, *et al.*, "Universal sheet resistance and revised phase dia-

gram of the cuprate high-temperature superconductors," *Proceedings of the National Academy of Sciences of the United States of America*, vol. 110, 2013.

[12] S. Blundell, *Magnetism in Condensed Matter*, ch. 3: Environments. Oxford Master Series in Condensed Matter Physics, OUP Oxford, 2001.

[13] M. Moretti Sala, V. Bisogni, C. Aruta, *et al.*, "Energy and symmetry of dd excitations in undoped layered cuprates measured by CuL3resonant inelastic x-ray scattering," *New Journal of Physics*, vol. 13, no. 4, 2011.

[14] S. Blundell, *Magnetism in Condensed Matter*, ch. 4: Interactions. Oxford Master Series in Condensed Matter Physics, OUP Oxford, 2001.

[15] N. F. Mott, "The Basis of the Electron Theory of Metals, with Special Reference to the Transition Metals," *Proceedings of the Physical Society. Section A*, vol. 62, no. 7, pp. 416–422, 1949.

[16] M. P. M. Dean, G. Dellea, R. S. Springell, *et al.*, "Persistence of magnetic excitations in La2xSrxCuO4 from the undoped insulator to the heavily overdoped non-superconducting metal," *Nature Materials*, vol. 12, pp. 1019–1023, 2013.

[17] P. Monthoux, A. V. Balatsky, and D. Pines, "Weak-coupling theory of high-temperature superconductivity in the antiferromagnetically correlated copper oxides," *Phys. Rev. B*, vol. 46, pp. 14803–14817, 1992.

[18] F. C. Zhang and T. M. Rice, "Effective Hamiltonian for the superconducting Cu oxides," *Phys. Rev. B*, vol. 37, pp. 3759–3761, 1988.

[19] G. Ghiringhelli, "High Temperature Superconductors studied with RIXS." Slides for the course "Magnetism and Superconductivity", Politecnico di Milano, 2021.

[20] J. F. Annett, *Superconductivity, superfluids and condensates*, ch. 7, Superfluid ^{3}He and unconventional superconductivity. Oxford master series in condensed matter physics, Oxford Univ. Press, 2004.

[21] J. F. Annett, *Superconductivity, superfluids and condensates*, ch. 1, Bose-Einsten condensates. Oxford master series in condensed matter physics, Oxford Univ. Press, 2004.

[22] J. F. Annett, *The macroscopic coherent state* , ch. 5, Superfluid ^{3}He and unconventional superconductivity. Oxford master series in condensed matter physics, Oxford Univ. Press, 2004.

[23] D. J. V. Harlingen, "Josephson Interferometry: Mapping the Pairing Symmetry of

Unconventional Superconductors." University of Illinois at Urbana-Champaign, 2007. https://conferences.illinois.edu/bcs50/pdf/vanharlingen.pdf.

[24] A. Damascelli, Z. Hussain, and Z.-X. Shen, "Angle-resolved photoemission studies of the cuprate superconductors," *Reviews of Modern Physics*, vol. 75, no. 2, p. 473–541, 2003.

[25] Z.-X. Shen, D. S. Dessau, B. O. Wells, *et al.*, "Anomalously large gap anisotropy in the a-b plane of $Bi_2Sr_2CaCu_2O_{8+\delta}$," *Phys. Rev. Lett.*, vol. 70, pp. 1553–1556, 1993.

[26] M. Hashimoto, I. Vishik, R. He, *et al.*, "Energy gaps in high-transition-temperature cuprate superconductors," *Nature Phys*, vol. 10, p. 483–495, 2014.

[27] E. Razzoli, Y. Sassa, G. Drachuck, *et al.*, "The Fermi surface and band folding in La2-xSrxCuO4, probed by angle-resolved photoemission," *New Journal of Physics*, vol. 12, 2010.

[28] I. M. Vishik, M. Hashimoto, R.-H. He, *et al.*, "Phase competition in trisected superconducting dome," *Proceedings of the National Academy of Sciences*, vol. 109, no. 45, pp. 18332–18337, 2012.

[29] W. Lee, I. Vishik, K. Tanaka, *et al.*, "Abrupt onset of a second energy gap at the superconducting transition of underdoped Bi2212," *Nature*, vol. 450, pp. 81–84, 2007.

[30] E. Fradkin, S. A. Kivelson, M. J. Lawler, J. P. Eisenstein, and A. P. Mackenzie, "Nematic fermi fluids in condensed matter physics," *Annual Review of Condensed Matter Physics*, vol. 1, no. 1, pp. 153–178, 2010.

[31] Y. Sato, S. Kasahara, H. Murayama, *et al.*, "Thermodynamic evidence for a nematic phase transition at the onset of the pseudogap in yba2cu3oy," *Nature Physics*, vol. 13, p. 1074–1078, Jul 2017.

[32] G. Seibold, R. Arpaia, Y. Peng, *et al.*, "Strange metal behaviour from charge density fluctuations in cuprates," *Communications Physics*, vol. 4, no. 7, 2021.

[33] C. M. Varma, P. B. Littlewood, S. Schmitt-Rink, E. Abrahams, and A. E. Ruckenstein, "Phenomenology of the normal state of Cu-O high-temperature superconductors," *Phys. Rev. Lett.*, vol. 63, pp. 1996–1999, 1989.

[34] K. Takenaka, J. Nohara, R. Shiozaki, and S. Sugai, "Incoherent charge dynamics of $La_{2-x}Sr_xCuO_4$: Dynamical localization and resistivity saturation," *Phys. Rev. B*, vol. 68, 2003.

[35] M. Platé, J. D. F. Mottershead, I. S. Elfimov, *et al.*, "Fermi Surface and Quasiparticle Excitations of Overdoped $Tl_2Ba_2CuO_{6+\delta}$," *Phys. Rev. Lett.*, vol. 95, p. 077001, 2005.

[36] S. Wakimoto, H. Zhang, K. Yamada, I. Swainson, H. Kim, and R. J. Birgeneau, "Direct Relation between the Low-Energy Spin Excitations and Superconductivity of Overdoped High-T_c Superconductors," *Phys. Rev. Lett.*, vol. 92, p. 217004, 2004.

[37] W. Wen, C. Dang, and L. Xie, "Photoinduced phase transitions in two-dimensional charge-density-wave 1T-TaS2 $*$,"$ChinesePhysicsB, vol.\ 28, p.\ 058504, may2019.$

[38] P. Aebi, T. Pillo, H. Berger, and F. Lévy, "On the search for fermi surface nesting in quasi-2d materials," *Journal of Electron Spectroscopy and Related Phenomena*, vol. 117-118, pp. 433–449, 2001. Strongly correlated systems.

[39] T. Straub, T. Finteis, R. Claessen, P. Steiner, S. Hüfner, P. Blaha, C. S. Oglesby, and E. Bucher, "Charge-Density-Wave Mechanism in $2H - NbSe_2$: Photoemission Results," *Phys. Rev. Lett.*, vol. 82, pp. 4504–4507, May 1999.

[40] J. Tranquada, B. Sternlieb, J. Axe, *et al.*, "Evidence for stripe correlations of spins and holes in copper oxide superconductors," *Nature*, vol. 375, pp. 561–563, 1995.

[41] P. Abbamonte, A. Rusydi, S. ASmadici, *et al.*, "Spatially modulated 'mottness' in $La_{2-x}Ba_xCuO_4$," *Nature Phys*, vol. 1, pp. 155–158, 2005.

[42] R. Comin and A. Damascelli, "Resonant X-Ray Scattering Studies of Charge Order in Cuprates," *Annual Review of Condensed Matter Physics*, vol. 7, 2015.

[43] A. Frano, S. Blanco-Canosa, B. Keimer, and R. J. Birgeneau, "Charge ordering in superconducting copper oxides," *Journal of Physics: Condensed Matter*, vol. 32, no. 37, p. 374005, 2020.

[44] J. E. Hoffman, E. W. Hudson, K. M. Lang, *et al.*, "A Four Unit Cell Periodic Pattern of Quasi-Particle States Surrounding Vortex Cores in $Bi_2Sr_2CaCu_2O_{8+\delta}$," *Science*, vol. 295, no. 5554, pp. 466–469, 2002.

[45] G. Ghiringhelli, M. L. Tacon, M. Minola, *et al.*, "Long-Range Incommensurate Charge Fluctuations in $(Y,Nd)Ba_2Cu_3O_{6+x}$," *Science*, vol. 337, no. 6096, pp. 821–825, 2012.

[46] T. Hanaguri, C. Lupien, Y. Kohsaka, *et al.*, "A 'checkerboard' electronic crystal state in lightly hole-doped $Ca_{2-x}Na_xCuO_2Cl_2$," *Nature*, vol. 430, pp. 1001–1005, 2004.

[47] R. Liang, D. A. Bonn, and W. N. Hardy, "Evaluation of CuO_2 plane hole doping in $YBa_2Cu_3O_{6+x}$ single crystals," *Phys. Rev. B*, vol. 73, p. 180505, 2006.

[48] S. Blanco-Canosa, A. Frano, E. Schierle, *et al.*, "Resonant x-ray scattering study of charge-density wave correlations in yba$_2$cu$_3$o$_{6+x}$," *Phys. Rev. B*, vol. 90, p. 054513, 2014.

[49] S. Gerber, H. Jang, H. Nojiri, *et al.*, "Three-dimensional charge density wave order in $YBa_2Cu_3O_{6.67}$ at high magnetic fields," *Science*, vol. 350, no. 6263, pp. 949–952, 2015.

[50] T. Wu, H. Mayaffre, S. Krämer, *et al.*, "Magnetic-field-induced charge-stripe order in the high-temperature superconductor YBa2Cu3Oy," *Nature*, vol. 477, no. 7363, p. 191–194, 2011.

[51] R. Arpaia, S. Caprara, R. Fumagalli, G. De Vecchi, Y. Y. Peng, E. Andersson, D. Betto, G. M. De Luca, N. B. Brookes, F. Lombardi, M. Salluzzo, L. Braicovich, C. Di Castro, M. Grilli, and G. Ghiringhelli, "Dynamical charge density fluctuations pervading the phase diagram of a Cu-based high-Tc superconductor," *Science*, vol. 365, no. 6456, p. 906–910, 2019.

[52] S. Jin, H. O'Bryan, P. Gallagher, T. Tiefel, R. Cava, R. Fastnacht, and G. Kammlott, "Synthesis and properties of the YBa2Cu4O8 superconductor," *Physica C: Superconductivity*, vol. 165, no. 5, pp. 415–418, 1990.

[53] J. Yu, K. T. Park, and A. Freeman, "Electronic structure and properties of YBa2Cu4O8," *Physica C: Superconductivity*, vol. 172, no. 5, pp. 467–476, 1991.

[54] P. Lightfoot, S. Pei, J. D. Jorgensen, Y. Yamada, T. Matsumoto, F. Izumi, and Y. Kodama, "Redetermination of the structure of the 80 K superconductor $YBa_2Cu_4O_8$ by time-of-flight neutron powder diffraction," *Acta Crystallographica Section C*, vol. 47, no. 6, pp. 1143–1145, 1991.

[55] S. Blundell, *Magnetism in Condensed Matter*, ch. 7: Magnetism in metals. Oxford Master Series in Condensed Matter Physics, OUP Oxford, 2001.

[56] M. Springford, N. Harrison, P. Meeson, and P.-A. Probst, "Comment on "de Haas–van Alphen effect and Fermi surface of $YBa_2Cu_3O_{6.97}$"," *Phys. Rev. Lett.*, vol. 69, pp. 2453–2453, 1992.

[57] N. Doiron-Leyraud, C. Proust, D. LeBoeuf, *et al.*, "Quantum oscillations and the Fermi surface in an underdoped high-Tc superconductor.," *Nature*, vol. 447, p. 565–568, 2007.

[58] M. Chan, R. Harrison, N.and McDonald, *et al.*, "Single reconstructed Fermi surface

pocket in an underdoped single-layer cuprate superconductor.," *Nat Commun*, vol. 7, 2016.

[59] F. Ronning, C. Kim, D. L. Feng, *et al.*, "Photoemission Evidence for a Remnant Fermi Surface and a d-Wave-Like Dispersion in Insulating $Ca_2CuO_2Cl_2$," *Science*, vol. 282, no. 5396, pp. 2067–2072, 1998.

[60] E. A. Yelland, J. Singleton, C. H. Mielke, N. Harrison, F. F. Balakirev, B. Dabrowski, and J. R. Cooper, "Quantum Oscillations in the Underdoped Cuprate $YBa_2Cu_4O_8$," *Phys. Rev. Lett.*, vol. 100, p. 047003, 2008.

[61] C. Proust, B. Vignolle, J. Levallois, S. Adachi, and N. E. Hussey, "Fermi liquid behavior of the in-plane resistivity in the pseudogap state of yba2cu4o8," *Proceedings of the National Academy of Sciences*, vol. 113, no. 48, p. 13654–13659, 2016.

[62] S. I. Mirzaei, D. Stricker, J. N. Hancock, *et al.*, "Spectroscopic evidence for fermi liquid-like energy and temperature dependence of the relaxation rate in the pseudogap phase of the cuprates," *Proceedings of the National Academy of Sciences*, vol. 110, no. 15, pp. 5774–5778, 2013.

[63] G. Grissonnanche, O. Cyr-Choinière, F. Laliberté, *et al.*, "Direct measurement of the upper critical field in cuprate superconductors," vol. 5, 2014.

[64] P. M. C. Rourke, A. F. Bangura, C. Proust, *et al.*, "Fermi-surface reconstruction and two-carrier model for the Hall effect in $YBa_2Cu_4O_8$," *Phys. Rev. B*, vol. 82, p. 020514, 2010.

[65] F. Rullier-Albenque, H. Alloul, C. Proust, P. Lejay, A. Forget, and D. Colson, "Total Suppression of Superconductivity by High Magnetic Fields in $YBa_2Cu_3O_{6.6}$," *Phys. Rev. Lett.*, vol. 99, p. 027003, 2007.

[66] L. J. P. Ament, M. van Veenendaal, T. P. Devereaux, J. P. Hill, and J. van den Brink, "Resonant inelastic x-ray scattering studies of elementary excitations," *Rev. Mod. Phys.*, vol. 83, pp. 705–767, Jun 2011.

[67] R. Fumagalli, *Cuprate high-Tc superconductors studied by polarization-resolved RIXS*. PhD thesis, Politecnico di Milano, 2020.

[68] S. Shrivastava, "Crystal structure of cuprate based superconducting materials," 05 2018.

[69] M. Minola, *Magnetic, orbital and charge fluctuations in layered cuprates studied by resonant soft x-ray scattering*. PhD thesis, Politecnico di Milano, 2013.

[70] L. Braicovich, J. van den Brink, V. Bisogni, M. M. Sala, L. J. P. Ament, N. B. Brookes, G. M. De Luca, M. Salluzzo, T. Schmitt, V. N. Strocov, and G. Ghiringhelli, "Magnetic Excitations and Phase Separation in the Underdoped $La_{2-x}Sr_xCuO_4$ Superconductor Measured by Resonant Inelastic X-Ray Scattering," *Phys. Rev. Lett.*, vol. 104, p. 077002, 2010.

[71] J. P. Hill, G. Blumberg, Y.-J. Kim, D. S. Ellis, *et al.*, "Observation of a 500 meV Collective Mode in $La_{2-x}Sr_xCuO_4$ and Nd_2CuO_4 Using Resonant Inelastic X-Ray Scattering," *Phys. Rev. Lett.*, vol. 100, p. 097001, 2008.

[72] ESRF, "Accelerators," 2022. https://www.esrf.fr/cms/live/live/en/sites/www/home/UsersAndScience/Accelerators.html.

[73] ESRF, "What is a synchrotron?," 2022. https://www.esrf.fr/cms/live/live/en/sites/www/home/about/synchrotron-science/synchrotron.html.

[74] J. Clarke, "Insertion Devices. Lecture 1. Introduction to Synchrotron Radiation ." ASTeC, Daresbury Laboratory, 2014. https://www.cockcroft.ac.uk/wp-content/uploads/2014/12/Lecture-1.pdf.

[75] D. Attwood, "Intro to Synchrotron Radiation ." Univ. California, Berkeley, 2007. https://people.eecs.berkeley.edu/ attwood/srms/2007/Lec08.pdf.

[76] R. Fumagalli, L. Braicovich, M. Minola, *et al.*, "Polarization-resolved Cu L 3 -edge resonant inelastic x-ray scattering of orbital and spin excitations in NdBa2Cu3O7," *Physical Review B*, vol. 99, 04 2019.

[77] ESRF, "RIXS end-station," 2022. https://www.esrf.fr/home/UsersAndScience/Experiments/EMD/ID32/RIXS.html.

[78] N. Brookes, F. Yakhou-Harris, K. Kummer, *et al.*, "The beamline ID32 at the ESRF for soft X-ray high energy resolution resonant inelastic X-ray scattering and polarisation dependent X-ray absorption spectroscopy," *Nuclear Instruments and Methods in Physics Research Section A: Accelerators, Spectrometers, Detectors and Associated Equipment*, vol. 903, pp. 175–192, 2018.

[79] Y. Song, J. Peng, X. Wang, G. Sun, and C. Lin, "Ambient-condition growth of superconducting yba2cu4o8 single crystals using koh flux," *Journal of Crystal Growth*, vol. 300, no. 2, pp. 263–266, 2007.

[80] Y.-T. Hsu, M. Berben, M. Čulo, *et al.*, "Anomalous vortex liquid in charge-ordered cuprate superconductors," *Proceedings of the National Academy of Sciences*, vol. 118, no. 7, 2021.

[81] Y. Y. Peng, G. Dellea, M. Minola, *et al.*, "Influence of apical oxygen on the extent of in-plane exchange interaction in cuprate superconductors," *Nature Physics*, vol. 13, p. 1201–1206, Aug 2017.

[82] R. Comin, A. Frano, M. M. Yee, *et al.*, "Charge Order Driven by Fermi-Arc Instability in $Bi_2Sr_{2x}La_xCuO_{6+\delta}$," *Science*, vol. 343, no. 6169, p. 390–392, 2014.

[83] S. Blanco-Canosa, A. Frano, T. Loew, *et al.*, "Momentum-Dependent Charge Correlations in $YBa_2Cu_3O_{6+\delta}$ Superconductors Probed by Resonant X-Ray Scattering: Evidence for Three Competing Phases," *Phys. Rev. Lett.*, vol. 110, p. 187001, 2013.

[84] M. Rossi, R. Arpaia, R. Fumagalli, *et al.*, "Experimental determination of momentum-resolved electron-phonon coupling," *Phys. Rev. Lett.*, vol. 123, p. 027001, Jul 2019.

[85] J. Lamsal and W. Montfrooij, "Extracting paramagnon excitations from resonant inelastic x-ray scattering experiments," *Phys. Rev. B*, vol. 93, p. 214513, Jun 2016.

[86] T. P. Devereaux, A. M. Shvaika, K. Wu, *et al.*, "Directly Characterizing the Relative Strength and Momentum Dependence of Electron-Phonon Coupling Using Resonant Inelastic X-Ray Scattering," *Phys. Rev. X*, vol. 6, p. 041019, Oct 2016.

[87] J. J. Lee, F. T. Schmitt, R. G. Moore, and others., "Interfacial mode coupling as the origin of the enhancement of tc in fese films on srtio3," *Nature*, vol. 515, no. 7526, p. 245–248, 2014.

[88] L. J. P. Ament, M. van Veenendaal, and J. van den Brink, "Determining the electron-phonon coupling strength from resonant inelastic x-ray scattering at transition metal l-edges," *EPL (Europhysics Letters)*, vol. 95, p. 27008, jul 2011.

[89] S. Moser, S. Fatale, P. Krüger, *et al.*, "Electron-phonon coupling in the bulk of anatase tio_2 measured by resonant inelastic x-ray spectroscopy," *Phys. Rev. Lett.*, vol. 115, p. 096404, Aug 2015.

[90] M. Le Tacon, G. Ghiringhelli, J. Chaloupka, M. M. Sala, *et al.*, "Intense paramagnon excitations in a large family of high-temperature superconductors," *Nature Physics*, vol. 7, p. 725–730, Jul 2011.

A | Appendix A

This Appendix is used to provide further material which has not been included in the previous Chapters. We will report the results of the data fittings on the H- and K-scans at each temperature value and on high-resolution RIXS measurements at each K-value.

A.1. K-scan best fits and backgrounds

Fig. A.1 shows the K-scans together with the corresponding best fits and linear backgrounds at each temperature. These are the backgrounds which have been subtracted to get the temperature dependence shown in Fig. 3.9. Data after background subtraction and the Lorentzian component of the fits are depicted in Fig. A.2. These Lorentzian curves have been used to realise the plots in Figs. 3.10 and 3.11.

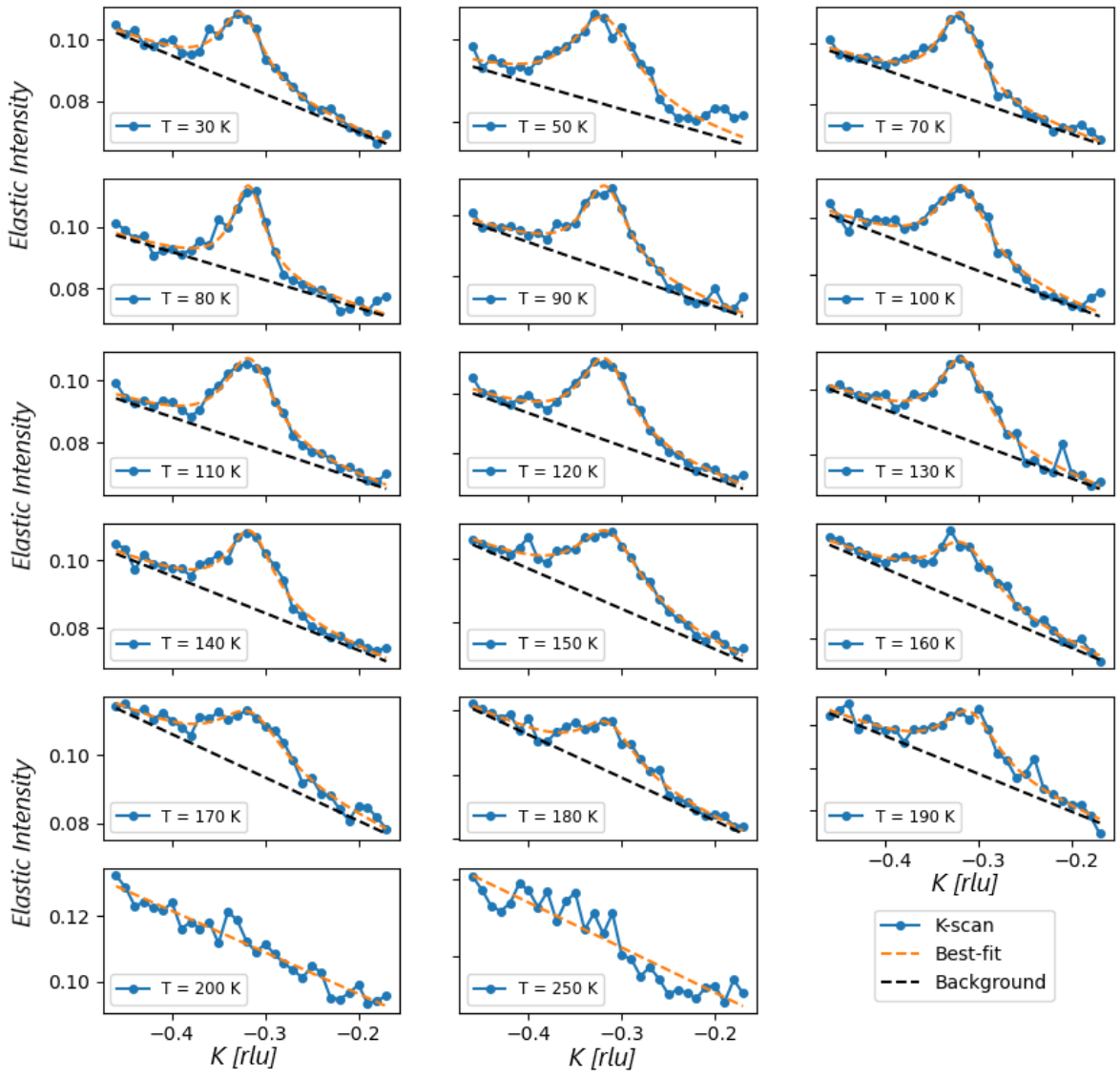

Figure A.1: K-scans and the corresponding best fits and linear backgrounds at each temperature. We remind that a Lorentzian lineshape on the top of a straight line was used as fitting function.

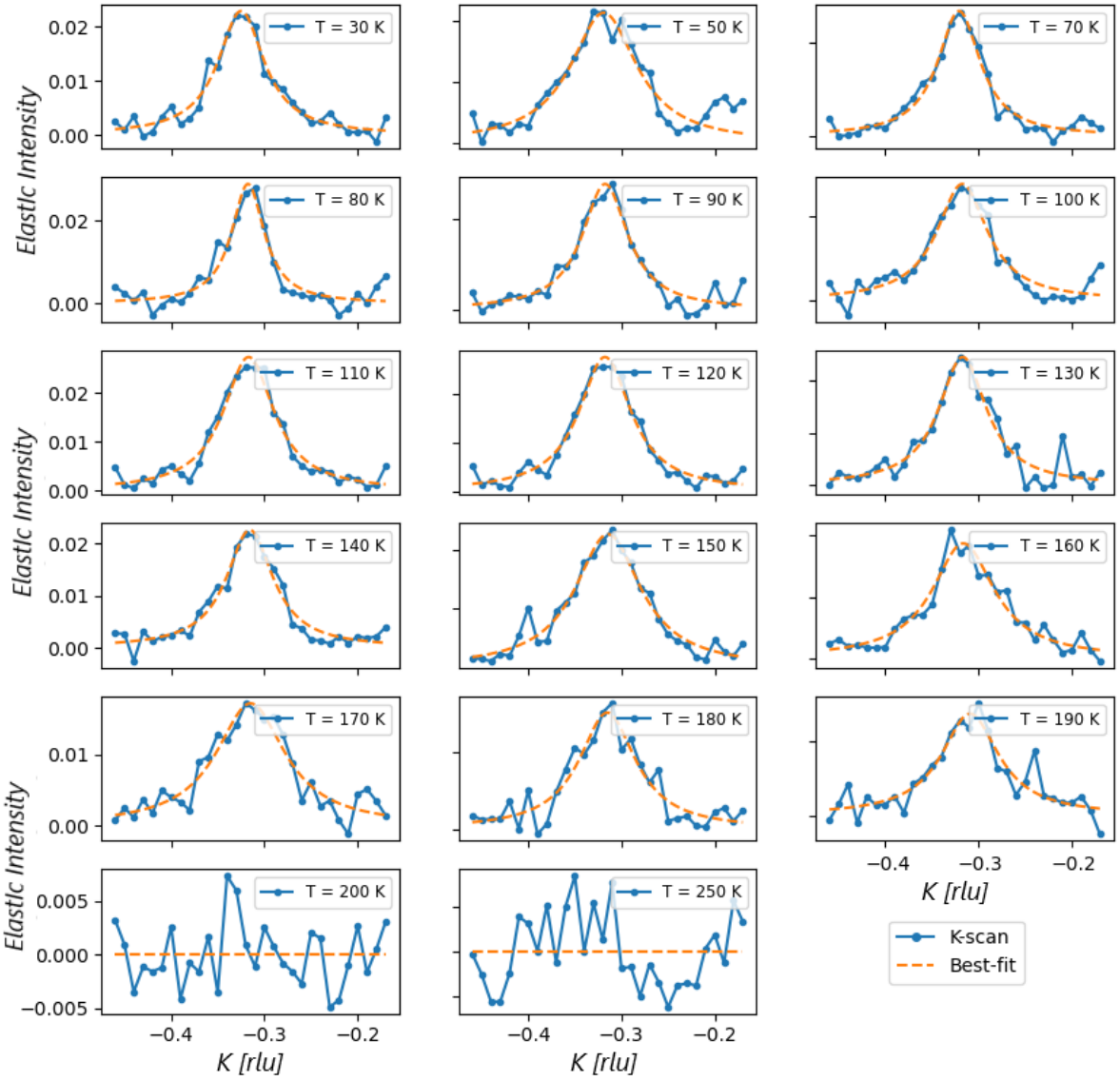

Figure A.2: K-scans after background subtraction and the corresponding Lorentzian component of the fits at each temperature.

A.2. Data fitting of H- and K-scans

Here the results of the data fitting on H- and K-scans at 80 K are provided. They have been used to realise pictures in Section 3.3.5. Top panels of Fig. A.3 report the best fits and the linear backgrounds, whereas the bottom panels refer to data after background subtraction. The Lorentzian part of the fits is displayed as well.

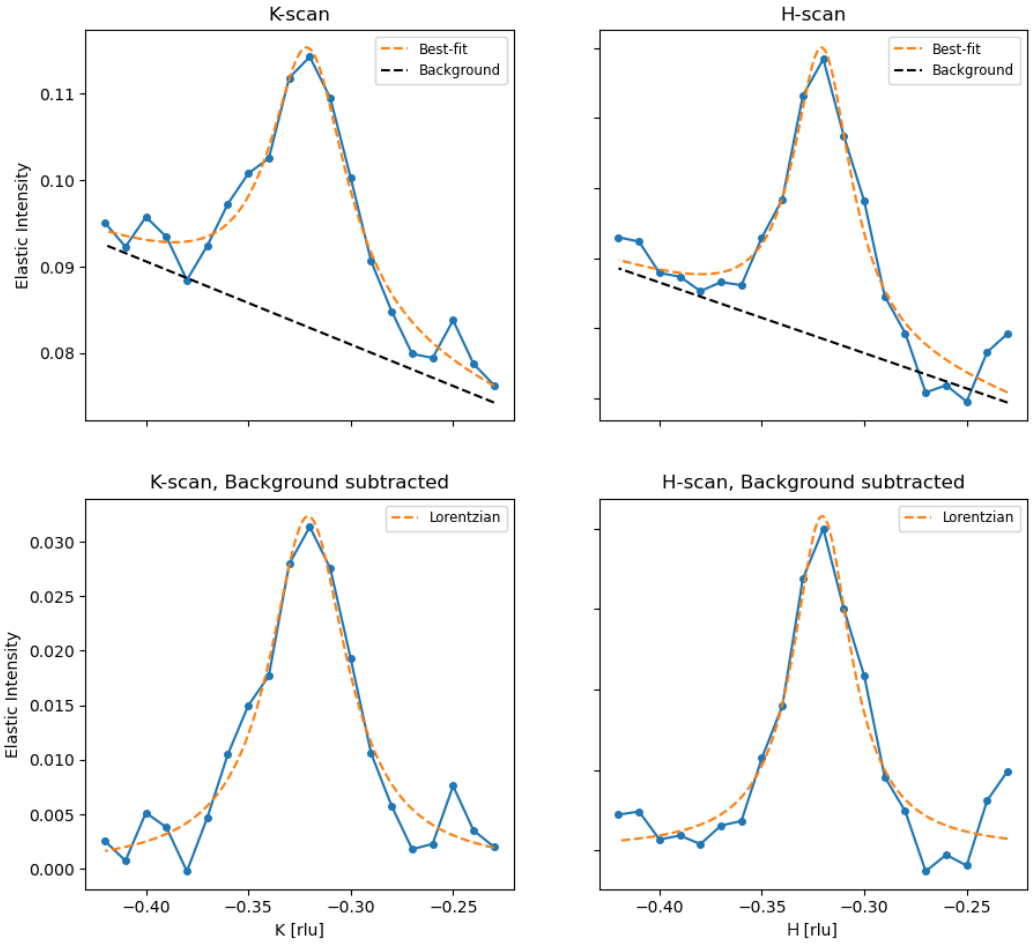

Figure A.3: Fitting results of H- and K-scans collected at the critical temperature. Top panels display the total fit and the linear background. Bottom panels show the data after subtracting the background together with the Lorentzian part of the fit.

A.3. Data fitting of high-resolution RIXS spectra

Figs. A.4 and A.5 reports the data fitting realised on high-resolution RIXS spectra collected at several K-values. The employed fitting function is given by the sum between a Guassian function, representing the elastic line, two Voigt profiles, which account for the phonon modes and a Fano lineshape, which fits the contribution deriving from magnetic excitations. These results have been used to create plots in Sections 3.4.3, 3.4.4 and 3.4.5.

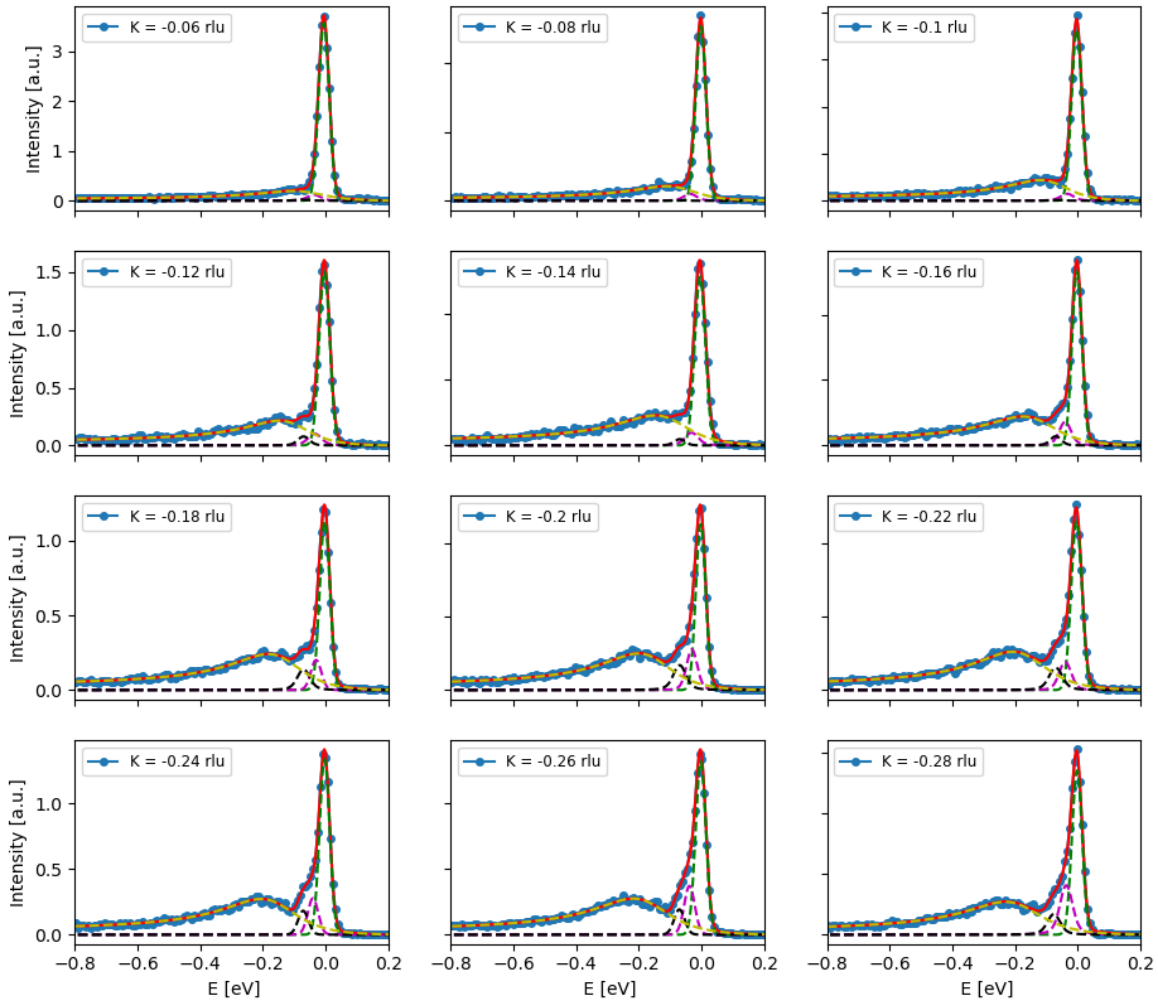

Figure A.4: Fitting results of RIXS spectra with $K \in [-0.06, -0.28]$ r l u collected at the critical temperature. Top panels display the total fit and the linear component which represents the background. Dashed lines represent the fitting components: the elastic line (green), the first phonon mode (pink), the second phonon mode (black) and the paramagnon (yellow).

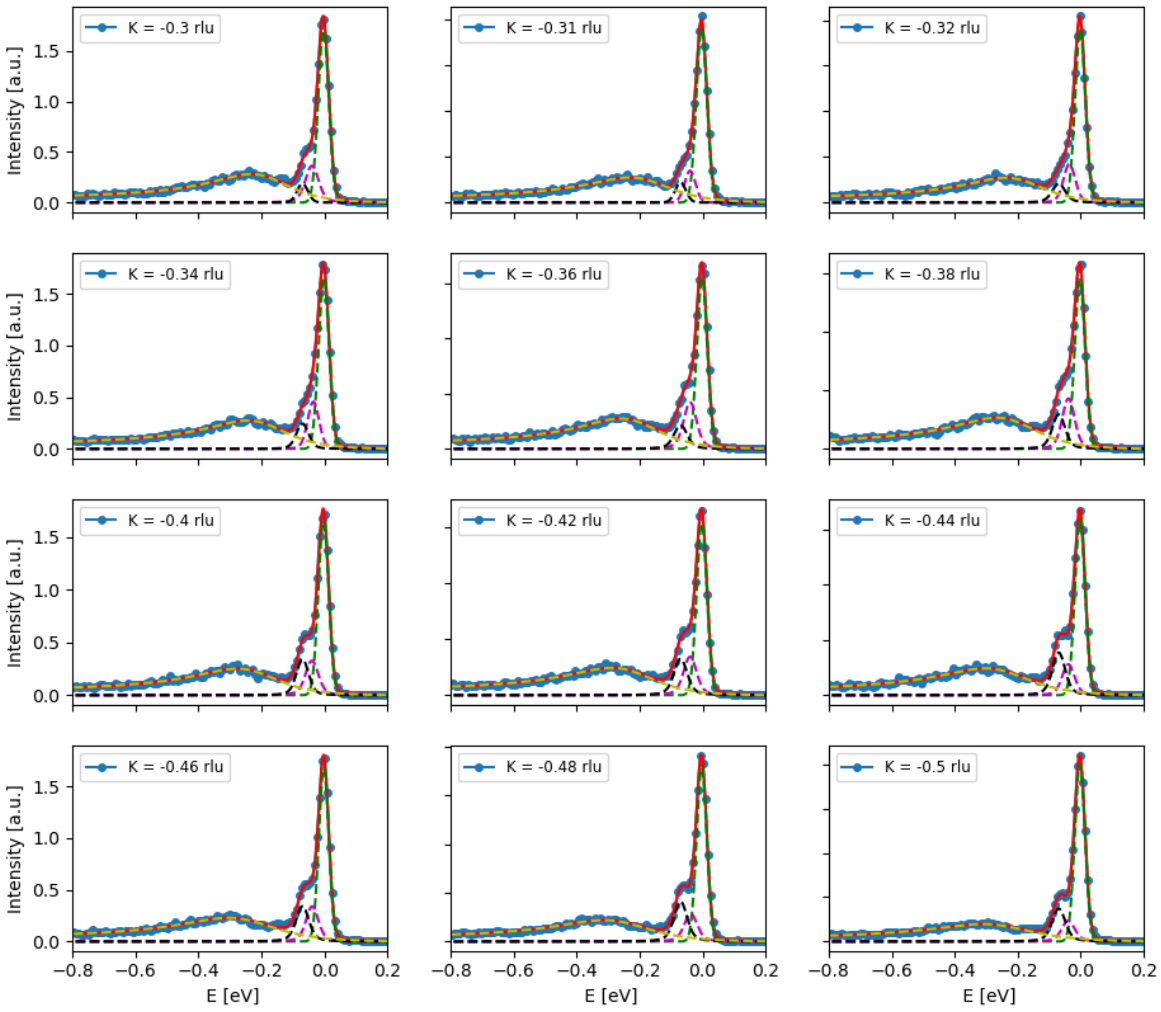

Figure A.5: Fitting results of RIXS spectra with $K \in [-0.30, -0.50]$ r l u collected at the critical temperature. Best fit is indicated by a red line. Dashed lines represent the fitting components: the elastic line (green), the first phonon mode (pink), the second phonon mode (black) and the paramagnon (yellow).

List of Figures

Acknowledgements

First, I would like to express my gratitude to my supervisor, Prof. Giacomo Ghiringhelli, which helped me throughout the realisation of this work and made this experience at the ESRF possible.
I also want to sincerely thank all the members of the ID32 beamline at the ESRF, with whom I had the pleasure to work. They shared with me their knowledge and they made me understand what it means working in a beamline and finding a solution to problems. In particular, special thanks go to Nicholas Brookes and Davide Betto for always making me feel part of the team and for supervising my work. Thank you, Davide, for conducting the experiments which have given rise to this thesis and for helping review this document, but, especially, for all that you have taught me during these months.
I would particularly like to thank Matteo Minola for giving me the possibility to spend two weeks at Max Plank Institute in Stuttgart, where I could contribute to the preparation of samples. Thank you, Matteo, for giving me substantial help in the writing and revision of this thesis.
Last but not the least, I would like to thank the friends I have shared this experience with and without whom nothing would have been the same. Thanks for making the time in Grenoble unforgettable.
My deepest gratitude cannot but go to my family and all my friends for supporting me, believing in me and encouraging me to follow my dreams. Thank you for making my life better.